

# THE MILLENNIUM ARECIBO 21-CM ABSORPTION LINE SURVEY. I. TECHNIQUES AND GAUSSIAN FITS

Carl Heiles

*Astronomy Department, University of California, Berkeley, CA 94720-3411;  
cheiles@astron.berkeley.edu*

T.H. Troland

*Department of Physics and Astronomy, University of Kentucky, Lexington, KY;  
troland@pa.uky.edu*

## ABSTRACT

We review the theory of measuring spectral lines in emission/absorption observations and apply it to a new survey of the 21-cm line against 79 continuum sources. We develop an observing technique and least-squares procedure to determine the opacity profile, the expected emission profile, and their uncertainty profiles. We discuss the radiative transfer for the two-component interstellar HI gas and use Gaussian components, separate ones for the Warm and Cold neutral media (WNM and CNM), as a practical implementation of a simple but physically correct model that successfully treats both simple and complicated profiles. Our Gaussians provide CNM spin temperatures, upper limits on kinetic temperatures for both CNM and WNM from the line widths, column densities, and velocities; we discuss these astrophysical aspects in Paper II.

## Contents

<b>1</b>	<b>INTRODUCTION</b>	<b>3</b>
<b>2</b>	<b>EXTRACTING EXPECTED AND OPACITY PROFILES FROM ARECIBO DATA</b>	<b>4</b>
2.1	The ON-OFF spectrum . . . . .	4
2.2	The Arecibo telescope and electronics . . . . .	4
2.3	The observing technique . . . . .	5
2.4	Obtaining the continuum source flux and antenna temperatures . . . . .	6
2.5	The meaning of our derived source fluxes . . . . .	7

2.6	Least-squares fitting the spectra . . . . .	7
2.6.1	The least-squares technique: theory . . . . .	7
2.6.2	The least-squares technique: illustration . . . . .	11
2.7	Evaluation of instrumental effects . . . . .	12
2.8	Machine-readable data and the two-panel plots . . . . .	15
2.9	Comparison of our results with previous ones . . . . .	16
<b>3</b>	<b>DERIVING CNM SPIN TEMPERATURES AND WNM BRIGHTNESS TEMPERATURES: RADIATION TRANSFER IN THE 21-cm LINE</b>	<b>17</b>
3.1	A single temperature HI . . . . .	17
3.2	A two-component HI . . . . .	17
3.3	Gaussian components and radiative transfer . . . . .	18
3.4	Permuting CNM components and trying different $\mathcal{F}$ for WNM components . . . . .	20
3.5	Calculating the physical parameters . . . . .	21
3.6	Limits on Opacities and Spin Temperatures for WNM Components . . . . .	22
<b>4</b>	<b>GAUSSIAN COMPONENTS AND OUR DATA</b>	<b>22</b>
4.1	Gaussian parameters in tabular form and graphical form . . . . .	22
4.2	The process of fitting Gaussians . . . . .	23
4.3	Optical lines versus the 21-cm line . . . . .	25
4.4	Errors incurred from fitting too many/too few Gaussians . . . . .	26
4.4.1	The low- $\tau(\nu)$ case . . . . .	26
4.4.2	The high- $\tau(\nu)$ case . . . . .	27
4.5	Fitting the opacity profiles: CNM Gaussian components . . . . .	27
4.5.1	Sources for which the CNM fits are fairly unambiguous . . . . .	27
4.5.2	Sources for which the CNM fits are more ambiguous or difficult . . . . .	39
4.6	Fitting the expected profiles: WNM Gaussian components . . . . .	40
4.6.1	Sources for which WNM fits are fairly unambiguous . . . . .	40
4.6.2	Sources for which the WNM fits are more ambiguous or difficult . . . . .	40

4.6.3	Sources with no CNM components . . . . .	41
4.7	Two illustrative examples of the combined Gaussian fitting process . . . . .	42
4.7.1	3C120 . . . . .	42
4.7.2	3C315 . . . . .	44
4.7.3	Commentary . . . . .	44
<b>5</b>	<b>COMPARISON OF GAUSSIAN-FIT RESULTS WITH SLOPE METHOD</b>	<b>46</b>
5.1	Two representative examples . . . . .	46
5.1.1	Unblended opacity components . . . . .	47
5.1.2	Blended multicomponent opacity profiles . . . . .	47
5.2	Sample of ten sources and conclusion . . . . .	50
<b>6</b>	<b>SUMMARY</b>	<b>50</b>

## 1. INTRODUCTION

In February 1999 we used the Arecibo<sup>1</sup> telescope to begin a series of Zeeman-splitting measurements of the 21-cm line in absorption against continuum radio sources. Zeeman-splitting measurements require high sensitivity and a by-product of this survey is a set of sensitive emission/absorption line data for 79 sources from which spin temperatures and other information can be gleaned.

In §2 we discuss Arecibo’s instrumental effects and introduce a least-squares technique to account for both them and for angular derivatives of the HI emission. In §3 we discuss the radiative transfer of the two-component (warm and cold) HI and define our technique of Gaussian fitting as a practical means to treat radiative transfer in a physically correct but simple model. §4 discusses the practical implementation of the Gaussian fitting process and the associated difficulties and uncertainties. §5 compares our method with a previous method for dealing with the radiative transfer, the “slope method”. §6 is a brief summary of the paper. Heiles (2001a) presented a preliminary report of the astrophysical implications of our Gaussian components on the WNM and CNM; Paper II (Heiles & Troland 2002) presents the complete discussion.

---

<sup>1</sup>The Arecibo Observatory is part of the National Astronomy and Ionosphere Center, which is operated by Cornell University under a cooperative agreement with the National Science Foundation.

## 2. EXTRACTING EXPECTED AND OPACITY PROFILES FROM ARECIBO DATA

### 2.1. The ON-OFF spectrum

In the presence of a continuum source that provides antenna temperature  $T_{src}$ , the on-source antenna temperature is

$$T_{src}(\nu) = T_{exp}(\nu) + T_{src}e^{-\tau(\nu)} , \quad (1)$$

where  $T_{exp}(\nu)$  is the “expected profile”, which is the emission that would be observed in the absence of the source, and  $\tau(\nu)$  is the 21-cm line opacity; both of these are functions of frequency because of the spectral line. The appended symbols ( $\nu$ ) indicate frequency-dependent quantities within the profile; unappended temperatures are continuum. In this paper, all temperatures are (Stokes  $I/2$ ) because they are the average of measurements in orthogonal polarizations.

Consider equation 1 and assume, for the moment, that the spatial derivatives are zero. Then the two unknowns  $T_{exp}(\nu)$  and  $e^{-\tau(\nu)}$  are easily separated observationally by taking on-source and off-source measurements, for which  $T_{src}$  changes from zero to the full source intensity. More generally the spatial derivatives are nonzero; using the on source and off source measurements, we include spatial derivatives to write a more complicated version of equation 1 and subject it to a least squares analysis, as discussed in detail in §2.6. By this procedure, the expected emission profile  $T_{exp}(\nu)$  and the opacity profile  $e^{-\tau(\nu)}$  (and, in addition, the spatial derivatives) are well-determined.

### 2.2. The Arecibo telescope and electronics

The Arecibo telescope has a reflector fixed on the ground and points by moving the feed structure. This makes many characteristics of the beam change as a source is tracked. These changes are discussed by Heiles et al (2001a) and documented in more detail on Arecibo’s website. We sampled two linearly polarized channels simultaneously, performing both auto and crosscorrelations with Arecibo’s three-level “interim” digital correlator, to generate and instrumentally correct all four Stokes parameters in the manner discussed by Heiles (2001) and Heiles et al (2001b).

We observed each source by repeating many times an observational pattern. A “pattern” consists of a sequence of  $J$  “measurements” at fixed, defined, different sky positions (denoted by subscript  $j$ ) relative to the source observed for prescribed times. We designed the patterns to measure the first and second derivatives of intensity on the sky so that we could correct for instrumental effects as described below. Each pattern contains one or more on-source measurements and at least four off-source measurements. The total integration time for a given source consists of  $N$  patterns (denoted by subscript  $n$ ).

The on-source antenna temperature can vastly exceed the off-source one. With three-level correlators it is important to keep the input level at the optimum value; this meant that the electronics gains for the on-source measurements ( $\mathcal{G}_n$  below) were set lower than those for the off-source ones ( $G_n$  below). These gains, which are functions of  $n$  but not of  $j$ , had to be calibrated independently and have independent uncertainties.

For each source we repeated a pattern  $N$  times. Each pattern is characterized by its own gains, so we have  $N$  values of  $\mathcal{G}$  and  $G$ ; we denote individual ones by the subscript  $n$ , e.g.  $\mathcal{G}_n$ .

### 2.3. The observing technique

We have two patterns for observing. One, called Z4, generates four off-source emission spectra and the on-source spectrum. The four allow determination of the first derivative of the emission line in the sky. The other pattern, called Z16, generates sixteen off-source emission spectra and the on-source spectrum (Figure 1). The sixteen allow determination of not only the first derivative of the emission line in the sky, but all second derivatives. The following details must be accounted for in the data reduction:

1. The on-source electronics gain  $\mathcal{G}_n$  for each pattern  $n$  is not perfectly calibrated.
2. The off-source electronics gain  $G_n$  for each pattern  $n$  is not perfectly calibrated.
3. The on-axis gain (“Kelvins per Jansky”)  $[\text{K Jy}^{-1}]_n$  of the telescope changes with  $(az, za)$ , so that the source deflection changes. This quantity is known from previous calibration data; we adopt it from a table lookup.
4. The off-source cold-sky system temperature  $T_{R,n}^*$  changes with  $za$  (but not by much). Our notation, with the subscript  $R$ , implies “Receiver” temperature, but this is not quite correct. Rather, it is the off-source cold-sky system temperature, which is the actual receiver temperature plus other sources of cold-sky noise including, specifically, the cosmic background radiation and also the  $za$ -dependent contribution from the ground;  $T_{R,n}^*$  depends on  $(az, za)$  and is known from previous calibration data. We do not measure it explicitly, but rather adopt it from a table lookup.
5. Arecibo’s beam shape changes with  $(az, za)$ . In particular, the location of the first zero in the antenna beam response changes and, moreover, does not always exist. This means that the off-source spectra contain some remnant of the source intensity so one cannot obtain the expected profile by going just a little way off source.

## 2.4. Obtaining the continuum source flux and antenna temperatures

In this and future sections we need to distinguish between measured quantities and true quantities. The difference arises from the fact that the gain calibrations ( $G$  and  $\mathcal{G}$ ) are imperfect. The measured quantities are denoted by the superscript  $m$  and the true quantities by  $*$ . For system temperatures (equations 2 below), the measured and true quantities are related by gain factors in the sense that the gain factor multiplied by the true quantity equals the measured one. Antenna temperatures are derived from system temperatures by subtracting a table-lookup receiver temperature (equations 4 below), so the relationship is more complicated. Measured quantities also have random noise, but in the following we temporarily assume they are noise-free so that we can write (schematically)  $T_{sys}^m = GT_{sys}^*$ .

For a particular off-source position  $j$  within pattern  $n$ , we directly measure the system temperature  $T_{sys,n,j}^m$ , which is

$$T_{sys,n,j}^m = G_n T_{sys,n,j}^* \quad (2a)$$

and, correspondingly for the on-source position (denoted by  $j = s$ ),

$$T_{sys,n,s}^m = \mathcal{G}_n T_{sys,n,s}^* \quad (2b)$$

The off-source antenna temperature, i.e. the excess response of the telescope over cold sky, includes the response to the source (which might enter through sidelobes) as well as any diffuse emission that happens to lie in the same direction and is simply

$$T_{ant,n,j}^* = T_{sys,n,j}^* - T_{R,n}^* \quad (3)$$

We define the measured antenna temperatures as

$$T_{ant,n,j}^m \equiv T_{sys,n,j}^m - T_{R,n}^* = G_n T_{sys,n,j}^* - T_{R,n}^* \quad (4a)$$

with the corresponding equation for the on-source position, for which we define the on-source antenna temperature to be the source temperature  $T_{src,n}$ :

$$T_{src,n}^m \equiv T_{sys,n,s}^m - T_{R,n}^* = \mathcal{G}_n T_{sys,n,s}^* - T_{R,n}^* \quad (4b)$$

We derive the source flux by assuming that all of the antenna temperature, including that portion that comes from unrelated diffuse emission, arises from the source, i.e. we define

$$S_{src} \equiv \frac{T_{src,n}^*}{[\text{K Jy}^{-1}]_n} = \frac{\frac{T_{sys,n,s}^m}{\mathcal{G}_n} - T_{R,n}^*}{[\text{K Jy}^{-1}]_n} \quad (5)$$

Except for  $\mathcal{G}_n$ , the quantities on the right hand side are known from our data or from previous calibration. The gains  $\mathcal{G}_n$  are randomly distributed with  $|\mathcal{G}_n - 1| \ll 1$ , so  $\frac{1}{\mathcal{G}_n}$  is also randomly distributed. Therefore, from the set of  $N$  patterns we obtain the best estimate for  $S_{src}$  from a least squares fit of the  $N$  equations

$$[\text{K Jy}^{-1}]_n S_{src} = T_{sys,n,s}^m - T_{R,n}^* , \quad (6)$$

i.e., by assuming all  $\mathcal{G}_n = 1$ .

Having performed the least squares fit, we rewrite equation 5 to solve for the unknown  $\mathcal{G}_n$ :

$$\mathcal{G}_n = \frac{T_{sys,n,s}^m}{[\text{K Jy}^{-1}]_n S_{src} + T_{R,n}^*} . \quad (7)$$

All quantities on the right-hand side are known, so this explicitly provides the value for each  $\mathcal{G}_n$  for each pattern, allowing us to correct the individual on-source measurements  $T_{sys,n,s}^m$  for the gain error (but not the off-source measurements; see §2.6).

## 2.5. The meaning of our derived source fluxes

We derive the source flux  $S_{src}$  with equation 5. In essence, this averages the difference between the  $\mathcal{G}_n$ -corrected system temperatures  $T_{sys,n,s}^m$  and the predicted cold-sky antenna temperatures  $T_{R,n}^*$ . Our sources are all small, no more than a few arcmin in diameter. If a source lies within an extended region of emission, then our derived source flux includes the antenna temperature from that extended region. Thus, our source fluxes should be systematically larger than those measured interferometrically. This does not affect the scales of our derived opacity spectra because they are derived from ON–OFF differences.

## 2.6. Least-squares fitting the spectra

### 2.6.1. The least-squares technique: theory

Conventionally, one observes off-source positions to obtain the “expected profile”  $T_{exp}(\nu)$ , which is the line profile one would observe at the source’s position if the continuum source were turned off. One uses the expected profile for two purposes: one subtracts it from the on-source

spectrum, which difference provides the opacity spectrum; and one combines it with the opacity to obtain the spin temperatures.

This conventional technique is not perfect because the off-source emission spectra differ from the expected profile. There are two reasons. First, the antenna response to the continuum source is not zero for the off positions, so the off-source emission spectra are contaminated by a small, unknown contribution from the opacity spectrum. Second, there is angular structure in emission spectra. We treat these problems using a least squares technique.

We assume that the angular structure in each spectral channel can be represented by a Taylor series expansion; for our early data we carried it to first order and we obtained the derivatives from a four-point off-source grid centered on the source (the Z4 pattern). Later we carried the expansion to second order. Obtaining second derivatives from measurements on the two-dimensional sky requires measuring a minimum of nine independent positions. Normally one selects positions on a nine-point grid centered on the position of interest, and includes the central position as an equal partner in the calculation of the derivatives. However, in this case the central point is not an equal partner because it contains the continuum source. Therefore we need at least one additional point. Moreover, we want redundancy so that we can estimate the uncertainties in the derived quantities. In practice, we made measurements on the 17-point grid shown in Figure 1; there is one on-source point and 16 off-source points (the Z16 pattern).

As described above, for each pattern we corrected the on-source measurement for the gain errors  $\mathcal{G}_n$ . However, all the off-source measurements for pattern number  $n$  have a single independently-calibrated gain  $G_n$  which differs from  $\mathcal{G}_n$ . If there were no gain errors for the off-source measurements, i.e. if  $G_n = 1$ , then each measurement  $j$  within pattern  $n$  would provide the true system temperature  $T_{sys,n,j}^*(\nu)$  at each frequency channel  $\nu$  in the profile, which satisfies the equation

$$T_{sys,n,j}^*(\nu) - T_{R,n}^* = [T_{exp}(\nu)] + \left[ \frac{\partial T_{exp}(\nu)}{\partial \alpha} \right] \Delta \alpha_j + \left[ \frac{\partial T_{exp}(\nu)}{\partial \delta} \right] \Delta \delta_j + \left[ \frac{\partial T_{exp}(\nu)^2}{\partial^2 \alpha} \right] \frac{(\Delta \alpha_j)^2}{2} + \left[ \frac{\partial T_{exp}(\nu)^2}{\partial \alpha \partial \delta} \right] (\Delta \alpha_j) (\Delta \delta_j) + \left[ \frac{\partial T_{exp}(\nu)^2}{\partial^2 \delta} \right] \frac{(\Delta \delta_j)^2}{2} + [e^{-\tau(\nu)}] T_{ant,n,j}^* . \quad (8)$$

Here, as before, we have  $N$  patterns, each of which is denoted with subscript  $n$ , and within each pattern we have  $J$  measurements, each of which is denoted by subscript  $j$ . Each pattern consists of measurements at  $J = 17$  positions, one of which is directly on-source; even the off-source positions have nonzero  $T_{ant,n,j}^*$ , as discussed above. The appended symbols  $(\nu)$  indicate frequency-dependent quantities within the profile; unappended temperatures are continuum. Quantities to be derived from a least squares treatment are enclosed in square brackets. There are 7 such quantities for the full second-order expansion and 4 for the first-order one.

In fact, however, we have off-source gain uncertainties, just as we had on-source gain uncertainties in §2.4. To convert from the idealized starred quantities to the measured ones, we multiply



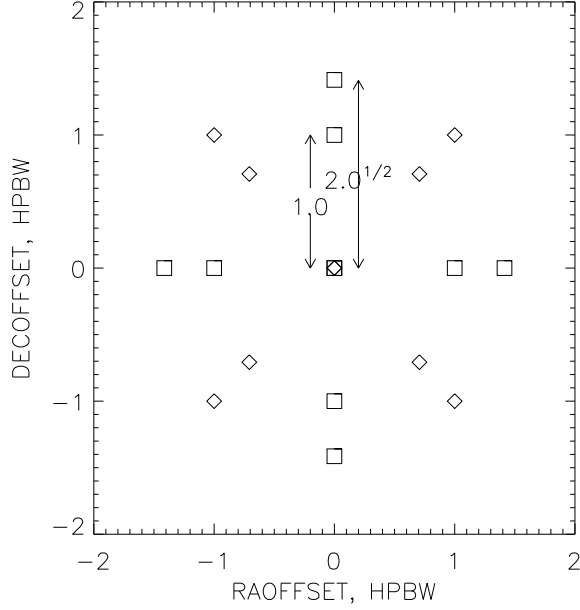


Fig. 1.— The 17-point measurement grid of the Z16 pattern. It consists of two crosses, one aligned with ra/dec (squares) and one at  $45^\circ$  to ra/dec (diamonds). The innermost points are  $1.0 \text{ HPBW}$  and the outermost points  $2^{1/2} \text{ HPBW}$  from the central point.

both sides of equation 8 by the off-source gain factor  $G_n$  and use equations 2a and 4a, yielding the more complicated

$$\begin{aligned}
 T_{sys,n,j}^m(\nu) - T_{R,n}^* &= [G_n] \left\{ [T_{exp}(\nu)] + \left[ \frac{\partial T_{exp}(\nu)}{\partial \alpha} \right] \Delta \alpha_j + \left[ \frac{\partial T_{exp}(\nu)}{\partial \delta} \right] \Delta \delta_j + \right. \\
 &\left. \left[ \frac{\partial T_{exp}(\nu)^2}{\partial^2 \alpha} \right] \frac{(\Delta \alpha_j)^2}{2} + \left[ \frac{\partial T_{exp}(\nu)^2}{\partial \alpha \partial \delta} \right] (\Delta \alpha_j) (\Delta \delta_j) + \left[ \frac{\partial T_{exp}(\nu)^2}{\partial^2 \delta} \right] \frac{(\Delta \delta_j)^2}{2} \right\} + \\
 &+ [e^{-\tau(\nu)}] (T_{sys,n,j}^m - [G_n] T_{R,n}^*) + ([G_n] - 1) T_{R,n}^* . \tag{9}
 \end{aligned}$$

The additional complexity of this equation does not lie simply in its being more cumbersome and also requiring a nonlinear, instead of a linear, least-squares fit. Rather, it means that we have  $N$  additional quantities, the  $G_n$ , for a total of  $(7 + N)$  unknowns for each spectral channel. We cannot solve this on a channel-by-channel basis because  $G_n$  is identical for all channels and, moreover, for a single channel the equations are degenerate. To remove the degeneracy we need to have different system temperatures, and these are provided by different channels with their varying 21-cm line emission and absorption spectral values.

We can solve the system of equations by considering all channels simultaneously in the fit to the  $N$  patterns. If  $C$  is the number of channels in the profile, this means solving  $CNJ$  equations. For each channel there are 7 unknowns [ $\tau(\nu)$  together with  $T_{exp}(\nu)$  and its various derivatives] and for the ensemble of patterns there are  $N$  unknown gains, so the total of unknowns is  $(7C + N)$ . The number of equations exceeds the number of unknowns and the solution exists as long as there is no degeneracy.

However, with current computers it is difficult (but hardly impossible) to solve these  $CNJ$  equations using least squares because often  $C \sim 1000$  and typically  $N \sim 100$ ; the entire assembly constitutes  $CNJ \sim 1.5 \times 10^6$  independent measurements with  $\sim (7000 + N)$  unknowns, so using matrix techniques requires generating and manipulating a  $\sim (1.5 \times 10^6) \times 7100$  matrix, which occupies  $\sim 40$  Gb of memory.

We attack the problem by splitting it into two parts; this is motivated by the fact that typically all  $G_n = 1$  to within a few percent. First, we assume all  $G_n = 1$  and solve equation 8 for the spectral quantities, treating each channel individually, first setting  $T_{ant,n}^* = T_{sys,n}^m - T_{R,n}^*$ . Solving these  $NJ \sim 1500$  separate equations by least-squares provides the 7 unknowns for each channel; repeating the process for each channel provides all of the  $\sim 7000$  unknowns. Next we use these derived quantities in a least-squares fit for the  $N$   $G_n$ , using all frequency channels simultaneously: this fit has, as before,  $\sim 1.5 \times 10^6$  measurements, but only  $N \sim 100$  unknowns, and is tractable. This provides the  $N$  gains; using these, we again perform the solution for the spectral quantities for each channel individually. It is unnecessary to iterate further, because this procedure converges rapidly and a single iteration derives the gains to high accuracy.

There is one additional complication in the least-square fitting, which is that each of the  $N$  patterns, each of the  $J$  measurements within each pattern, and each frequency channel have a different intrinsic noise. For each of the  $NJ$  measurements the system temperature is different; in particular, the on-source measurements within a pattern have a significantly, sometimes much, higher system temperature than the off-source measurements. Moreover, the system temperatures depend on frequency; for example, at the peak optical depth of the 21-cm line, the on-source system temperature is smaller than that off the line. Finally, some of our data were taken with the five-point observing grid and some with the 17-point grid; the individual measurements for these grids have different integration times. The equation of condition for each measurement for a particular spectral channel received the weight  $W_n(\nu)$  equal to the reciprocal of the rms noise  $\sigma(T)$  calculated in the usual way<sup>2</sup>

$$W_n(\nu) = \frac{1}{\sigma(T(\nu))} \tag{10a}$$

---

<sup>2</sup>see §15.4 of Press et al (1992), which calls the set of equations of condition the “design matrix”.

where

$$\sigma(T(\nu)) = \frac{0.77T_{sys}(\nu)}{\sqrt{t\Delta\nu}} \quad (10b)$$

where  $T_{sys}(\nu)$  is the system temperature in that channel,  $t$  the integration time, and  $\Delta\nu$  the frequency separation between channels; we empirically determined the factor 0.77 as being what was required to reproduce the observed  $\sigma(T(\nu))$ .

### 2.6.2. The least-squares technique: illustration

Figure 2 illustrates the fit technique and results for 3C454.3. We illustrate using this source for two reasons. First, it is strong, so that the off-source positions have an easily detectable continuum flux from the source. In addition, it has unusually large gain errors, both for on-source  $\mathcal{G}_n$  and off-source  $G_n$ , for the following reason. It is a VLBI calibrator and was observed near Solar maximum in early March 1999, when it had the same right ascension of the Sun; this put it only about  $23^\circ$  from the Sun. It suffered severe interplanetary scintillation, which produced some variability in its apparent intensity on the time scale of a few seconds, which was the interval during which our cal was turned on and off; these variations produced significant errors in the measured cal deflection, which led to gain errors for the on-source spectra as high as  $\sim 50\%$  and for the off-source spectra as high as  $\sim 10\%$ .

Figure 2 plots the measured antenna temperatures at frequency  $\nu 1094$  (spectral channel 1094) versus the measured continuum antenna temperatures. We chose this channel because it has the peak optical depth. The vertical scale of the left panel is  $T_{ant,n,j}^m(\nu 1094) = T_{sys,n,j}^m(\nu 1094) - T_{R,n}^*$ , i.e. the spectral antenna temperature *not* corrected for gain. The vertical scale of the right panel is the gain-corrected equivalent  $T_{ant,n,j}^*(\nu 1094)$ , where we use  $\mathcal{G}_n$  and  $G_n$  to correct the on-source and off-source measurements, respectively.

These plots are for the Z4 pattern with one on-source and four off-source measurements. The on-source datapoints are those having  $T_{ant,n} > 100$  K. There is one on-source datapoint for each pattern  $n$ ; its gain is the on-source gain  $\mathcal{G}_n$ . There are four off-source datapoints for each pattern  $n$ ; their gains are all identical, equal to the off-source gain  $G_n$ .

There are four plotted lines in each of the two panels of Figure 2. Each line is a least-squares fit for the measurements of the on position and one of the four off positions. They have slightly different  $y$ -intercepts but, as a constraint of the fits, identical slopes. The slope is  $e^{-\tau(\nu 1094)}$ . The four  $y$ -intercepts are the observed antenna temperatures for the four off positions, averaged over all  $N$  patterns.

In the left panel the dispersion of on-source antenna temperatures is huge, which is a result of the anomalously high gain errors produced by the scintillation. The dispersion of the off-source points is much less, but still larger than expected. These excessive dispersions are produced by

scintillation. The dispersions are much smaller for the gain-corrected data in the right panel.

In the right panel, the corrected on-source antenna temperatures disperse along the plotted line. This shows that the gain-corrected dispersion does not arise from statistical noise. Rather, it is real and reflects Arecibo’s  $(az, za)$ -dependent point-source gain  $[\text{K Jy}^{-1}]_n$ . Similarly, the off-source points disperse along the line; this is produced by the small responses of the beam to the source at the off-source positions, which differ from one pattern  $n$  to another as the telescope beam rotates on the sky.

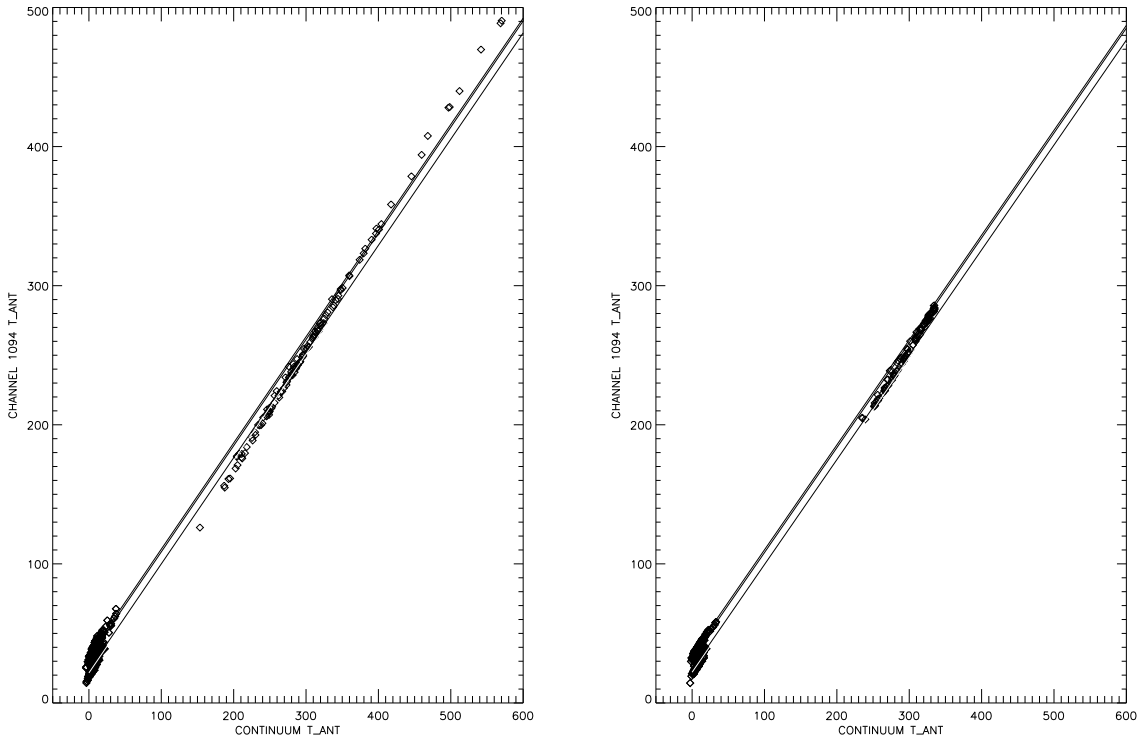


Fig. 2.—  $T_{ant}$  for frequency  $\nu 1094$  (spectral channel 1094) versus  $T_{ant}$  for the continuum. On-source datapoints for pattern  $n$  are those having  $T_{ant,n} > 100$  K; the others are off-source points, four for each pattern. The left panel shows the measured values without gain correction, the right panel with gain correction. See §2.6.2.

## 2.7. Evaluation of instrumental effects

Our ultimate goal is to derive only two of the spectral profile parameters in equations 8 and 9, namely the expected profile  $T_{exp}(\nu)$  and the opacity profile  $e^{-\tau(\nu)}$ . We need the other profile parameters involving angular derivatives only for the purpose of estimating uncertainties in the two

desired profiles.

The least squares process itself directly provides uncertainties in the  $M$  derived parameters; the equation for the  $m$ 'th parameter is, in schematic form,

$$error_m = C_{mm} \frac{\sum_{n=0}^{N-1} residual_n^2}{N(N-M)} \quad (11)$$

where  $C_{mm}$  is the  $m$ 'th diagonal element of the covariance matrix and  $N$  is the number of independent patterns. There are three basic assumptions in this equation. Most important is that the measurements are independent. Also, that the residuals are randomly (normally) distributed about the true value and that there is no covariance among the derived quantities.

However, this equation cannot apply for our derived spectral parameters: specifically, while we can divide by  $(N - M)$  we should certainly not divide by the additional factor of  $N$ . The reason is that we have a number  $N$  identical patterns, meaning  $N$  measurements of each OFF position and the ON position. Suppose that there were no instrumental noise; then the residuals for all patterns would be identical, because the residuals would produced be only by the higher angular derivatives than we measure. In this case, dividing by the additional factor of  $N$  produces a meaningless and unrealistic reduction in  $error_m$ . In fact, each of the  $N$  patterns does have some instrumental noise. We need a technique to average the instrumental noise but not to artificially decrease the derived  $error_m$ .

We describe our technique for deriving the error in  $T_{exp}(\nu)$  for the 17-point pattern; we use a similar technique for the 5-point pattern. The 17-point pattern has 16 OFF measurements. For a set of  $N$  patterns, we average each OFF measurement over the  $N$  patterns; this averages the instrumental noise and provides a fairly noise-free measurement of the antenna temperature spectrum at each of the 16 independent OFF positions. Also, equation 8 provides a *prediction* of the same spectrum at each OFF position once the fitting process has yielded spectra for the unknowns in that equation. For each channel independently, we calculate the 16 differences between the measured and predicted antenna temperatures. These 16 residuals represent 16 different estimates of the error of the fit in predicting the antenna temperature in that channel. We average the squares of these 16 residuals and take the square root, obtaining an rms spectrum  $\Delta T(\nu)$  in which the spectral values are statistically representative *uncertainties* of the predicted antenna temperatures at the OFF positions.  $\Delta T(\nu)$  should also characterize the uncertainties of the predicted antenna temperatures at the ON position; thus  $\Delta T_{exp}(\nu) = \Delta T(\nu)$ .

The error in the expected profile is simply  $\Delta T_{exp}(\nu)$ . To derive the error in the optical depth profile, we recall that if the source were turned off (making its flux  $S = 0$  Jy) then the ON-source antenna temperature  $T_{ON,0Jy}$  is the expected profile

$$T_{ON,0Jy}(\nu) = T_{exp}(\nu) \quad (12a)$$

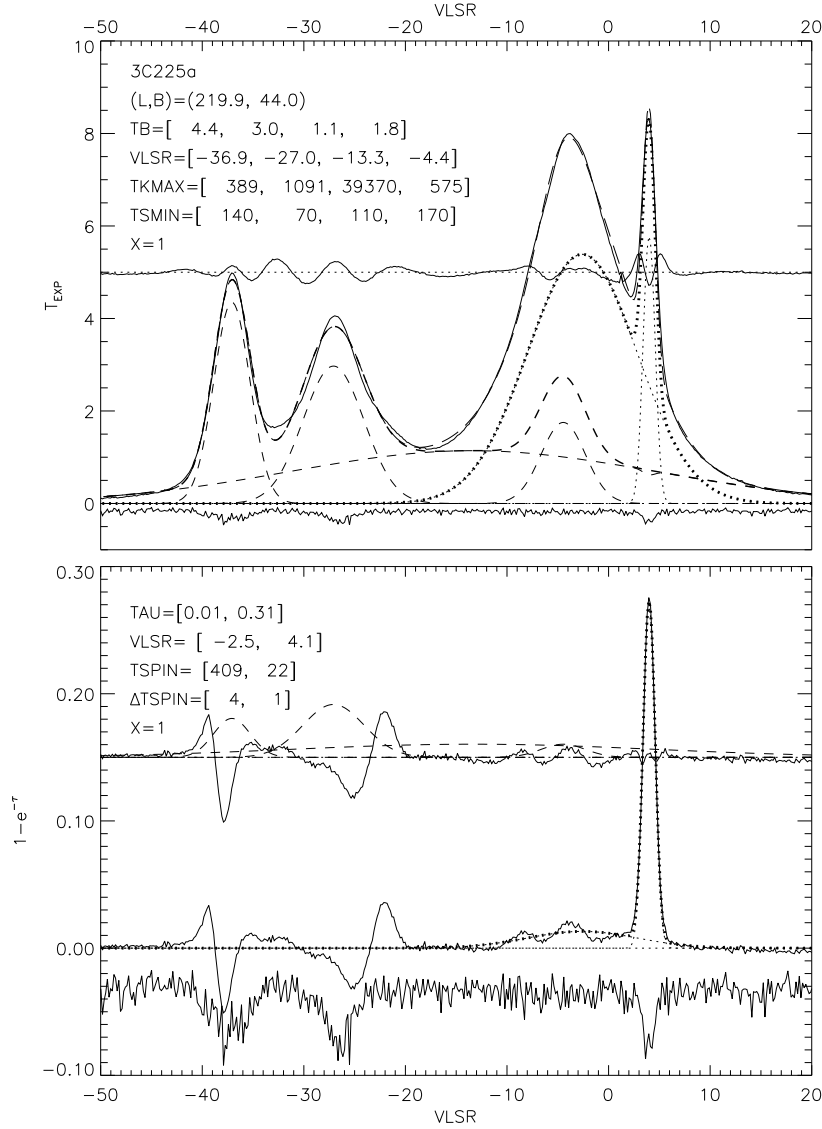


Fig. 3.— Illustrating the derived spectral parameters and their uncertainties as derived in §2.7 for the source 3C225a, which has severe problems with derivatives. In the top panel, the solid line profile extending above zero is the expected profile  $T_{exp}(\nu)$  and the solid line profile extending below zero is the (negative of) its uncertainty  $\Delta T_{exp}(\nu)$ . In the bottom panel, the solid line profile extending above zero is the opacity profile  $[1 - e^{-\tau}(\nu)]$  and the solid line profile extending below zero is the (negative of) its uncertainty  $\Delta e^{-\tau}(\nu)$ . Gaussian parameters for the WNM (top) and CNM (bottom) are given in square brackets. For a complete description of other features in these two-panel plots, see §2.8 and 4.1. Plots for all sources are in the electronic edition of *The Astrophysical Journal*. Also, they can be retrieved by ftp from [vermi.berkeley.edu/pub/zobs/bigfig.ps](http://vermi.berkeley.edu/pub/zobs/bigfig.ps).

and with the source turned on ( $S = S_{src}$  Jy) we have

$$T_{ON, S_{src}Jy}(\nu) = T_{exp}(\nu) + T_{src}e^{-\tau(\nu)} \quad (12b)$$

where  $T_{src} = [\text{K Jy}^{-1}]S_{src}$  is the continuum antenna temperature of the source. Combining these provides

$$e^{-\tau(\nu)} = \frac{T_{ON, S_{src}Jy}(\nu) - T_{exp}(\nu)}{T_{src}} \quad (12c)$$

To calculate the uncertainty in the opacity profile  $\Delta e^{-\tau(\nu)}$ , we retain only the uncertainty in  $T_{exp}(\nu)$ ; the fractional errors in  $T_{ON, S_{src}Jy}(\nu)$  and  $T_{src}$  are negligible because they are averages of  $N$  directly-measured quantities. This gives

$$\Delta e^{-\tau(\nu)} = \frac{\Delta T_{exp}(\nu)}{T_{src}} \quad (12d)$$

Figure 3 illustrates these results for 3C225a, for which the angular derivatives for  $V_{LSR} \lesssim -15$  km s<sup>-1</sup> are particularly deleterious. The top panel shows the expected profile  $T_{exp}(\nu)$  and its error  $\Delta T_{exp}(\nu)$ ; the bottom panel, the opacity profile  $e^{-\tau(\nu)}$  and its error  $\Delta e^{-\tau(\nu)}$ . The relative error in the expected profile  $\Delta T_{exp}(\nu)/T_{exp}(\nu)$  is small, which is typical for all sources.

For our sources the relative errors in the opacity profile are usually, but not always, small. For the example of 3C225a the errors for the negative velocity peaks are comparable to the measured values. This is fortunate, as the measured values for  $e^{-\tau(\nu)}$  exceed unity—meaning  $\tau < 0$ , which implies an interstellar maser! We don’t expect negative spin temperatures for the 21-cm line, and our error analysis shows that these measurements are meaningless. This source, 3C225a, is a serious example of large angular derivatives in the 21-cm line emission. Some sources are equally serious, although none of these others happens to exhibit apparent maser emission as a result.

## 2.8. Machine-readable data and the two-panel plots

Table 1 presents the expected profile, the opacity profile, and the various derivatives of the emission profile for all sources.

We exhibit our results for each source in a plot with two panels. We present plots for all sources in the electronic edition of *The Astrophysical Journal*, of which Figure 3 is an example. For each source, we choose the smallest possible velocity range for each plot because we are interested in the fine-scale velocity structure. Sometimes this requires us to cut off some emission and/or opacity components that lie outside the displayed range; however, we do this only when the fits outside the

displayed range are good. In no case do we restrict the velocity range when the fits do not agree with the data, or if there is interesting profile structure, outside the range. For two sources that have both wide- and narrow-velocity structure we present two velocity ranges.

In the top panel, the solid line profile extending above zero is the expected profile  $T_{exp}(\nu)$ . The dashed curves show the fitted emission from each individual WNM component, including absorption by the CNM (described in §3), and the heavy-dashed curve shows the totality of WNM fitted Gaussians  $T_{B,WNM}$  (equation 20). The solid line near mid-profile-height is the residuals of the data from the fit. The dotted curves show the intrinsic emission from each individual CNM component, not including absorption from the CNM components that lie in front, and the heavy dots the predicted emission of all CNM components including absorption from the CNM components that lie in front ( $T_{B,CNM}$  in equation 19). The long-dashed curve is the predicted expected profile ( $T_{B,WNM} + T_{B,CNM}$ ). The solid line profile extending below zero is the (negative of the) uncertainties  $\Delta T_{exp}(\nu)$  described in §2.7.

In the bottom panel, the solid line profile extending above zero is the opacity profile  $[1 - e^{-\tau(\nu)}]$ . The dotted curves show each individual CNM opacity Gaussian and the heavy dots show the sum of all the CNM Gaussians  $[1 - e^{-\tau(\nu)}]$ , with  $\tau(\nu)$  from equation 18. The solid line near mid-profile-height is the residuals of the data from the fit. The dashed curve near mid-profile height shows the sum of the lower limits of WNM opacity (§3.6), separately for each WNM component. The solid line profile extending below zero is the (negative of the) uncertainties in the opacity profile  $\Delta e^{-\tau(\nu)}$  (equation 21c).

Annotations in the top and bottom panels list properties of the WNM and CNM Gaussian components, respectively, listed in order of increasing velocity. In the upper panel, TB is the fitted intrinsic, unabsorbed brightness temperature of each WNM component ( $T_{0,k}$  in equation 20) and TKMAX is the upper limit kinetic temperature from the linewidth (§4.1). TSMIN is the lower limit on WNM spin temperature (§3.6).

In the lower panel, TAU is the peak optical depth of each CNM component  $\tau_{0,n}$  in equation 18, TSPIN is the fitted value for spin temperature  $T_{s,n}$  in equation 19, and  $\Delta TSPIN$  is the uncertainty in  $T_{s,n}$  (equation 21c).

Also, each panel has a parameter  $X$ , which is the factor by which both the residuals and profile errors are magnified for clarity. If the bottom panel has no properties listed, then no CNM components were fit.

## 2.9. Comparison of our results with previous ones

We compare our results with two of the most sensitive previous HI line absorption surveys, Dickey, Salpeter, & Terzian (1978; DST) and Payne, Salpeter, & Terzian (1982; PST). The comparisons cannot be exact because we don't have the original data. We have 10 sources in common



with PST; all show reasonable agreement. For a few we see weak opacity tails where PST might not and for a few the scales of the measured quantity, which is  $(1 - e^{-\tau(\nu)})$ , differ by up to  $\sim 15\%$ .

We have 15 sources in common with DST, of which 13 have detectable absorption lines. Of these 13, most show reasonable agreement, again with possible differences in profile wings and scale. Three agree badly: 3C237, 3C310, and 3C348. The disagreements are in the line shape: the DST profiles are either broader or have more components than ours. Profiles with more components appear like “ghosts”, with a pattern of less-intense components shifted with respect to the same pattern of more intense ones. PST observed 3C237, which result agrees with ours. Dickey (personal communication) confirms our suspicion that the local oscillator during some of his observations was either unstable or improperly set for Doppler correction because of the transient nature of the Arecibo software at the time. Greisen and Liszt (1986) observed 3C348 interferometrically and obtained an opacity spectrum that agrees with ours; they erroneously ascribed their disagreement with DST to difficulties with the single-dish observing and data-reduction process.

### 3. DERIVING CNM SPIN TEMPERATURES AND WNM BRIGHTNESS TEMPERATURES: RADIATION TRANSFER IN THE 21-cm LINE

#### 3.1. A single temperature HI

Much HI emission/absorption work has assumed a single temperature HI component, for which the equation of transfer is

$$T_{exp}(\nu) = T_s(1 - e^{-\tau(\nu)}) \quad (13)$$

Both the expected profile  $T_{exp}(\nu)$  and the opacity profile  $\tau(\nu)$  are measured quantities, so one obtains the spin temperature directly from this equation.

However, the assumption of a single temperature is clearly inadequate because emission profiles are always wider than opacity profiles. This means that some HI is so warm that it produces emission, contributing to  $T_{exp}(\nu)$  but having negligible opacity; this produces spin temperatures  $T_s$  that lie between the warm and cold values.

#### 3.2. A two-component HI

This observational situation leads to the concept of a two-component medium, with the Cold Neutral Medium (CNM) providing the opacity and also brightness temperature and the Warm Neutral Medium (WNM) providing only brightness temperature. Separating the CNM and WNM contributions to  $T_{exp}(\nu)$  then becomes the major difficulty.

The equation of transfer for this case is discussed recently by Mebold et al (1997) and Dickey et al (2000). The expected profile consists of the WNM and the CNM components:

$$T_{exp}(\nu) = T_{B,WNM}(\nu) + T_{B,CNM}(\nu) \quad (14)$$

Here a fraction  $\mathcal{F}$  of the WNM lies in front of the CNM so that a fraction  $(1 - \mathcal{F})$  of the WNM emission is absorbed by the CNM gas:

$$T_{B,WNM}(\nu) = T_{E,WNM}(\nu)[\mathcal{F} + (1 - \mathcal{F})e^{-\tau(\nu)}] \quad (15)$$

where  $T_{E,WNM}(\nu)$  is the intrinsic, unabsorbed emission from the WNM gas and  $\tau(\nu)$  is the CNM opacity. The emission from the CNM is just the usual

$$T_{B,CNM}(\nu) = T_s(1 - e^{-\tau(\nu)}) \quad (16)$$

These authors discuss and illustrate how to separate the components by plotting the two observables  $T_{exp}(\nu)$  and  $[1 - e^{-\tau(\nu)}]$  against each other:

$$T_{exp}(\nu) = T_{E,WNM}(\nu) + [T_s - T_{E,WNM}(\nu)(1 - \mathcal{F})][1 - e^{-\tau(\nu)}] \quad (17)$$

The  $y$ -intercept is  $T_{E,WNM}(\nu)$  and the slope is  $[T_s - T_{E,WNM}(\nu)(1 - \mathcal{F})]$ . Because  $\mathcal{F}$  lies between 0 and 1, the slope provides limits on  $T_s$ . Some inaccuracy occurs because in the region where the slope is defined the quantities change with  $\nu$ , but nevertheless the method seems to produce reasonable results. We call this the ‘‘slope method’’.

Previous single-dish authors, in contrast, implicitly assume that clouds are *not* isothermal. They derive the spin temperature from equation 13 at the opacity profile peak, where the derived temperature is coldest; this spin temperature lies between the lowest and highest temperatures along the line of sight through the cloud. Moreover, temperatures derived off of the opacity profile peak are warmer. Thus each point on their histograms does not represent a true mean cloud temperature; rather, it represents the lowest derived temperature, which itself is a weighted mean temperature for which the weights are unknown.

### 3.3. Gaussian components and radiative transfer

Our emission and opacity profiles clearly consist of multiple components, which often overlap and have different spin temperatures. This requires generalizing the equations in §3.2, which we accomplish by assuming the components can be represented as Gaussians.

For each CNM opacity spectrum, we represent its components' optical depths by a set of  $N$  Gaussians. Thus we least-squares fit the observed opacity spectrum  $e^{-\tau(\nu)}$ , where

$$\tau(\nu) = \sum_0^{N-1} \tau_{0,n} e^{-[(\nu - \nu_{0,n})/\delta\nu_n]^2} \quad (18)$$

in which  $(\nu_{0,n}, \delta\nu_n)$  are (central frequency,  $\frac{1}{e}$  width) of component  $n$ . We assume that each component is an independent physical entity and is isothermal with spin temperature  $T_{s,n}$ . This fit yields values for all  $\tau_{0,n}$ ,  $\nu_{0,n}$ , and  $\delta\nu_{0,n}$ .

Having fit the opacity profile to equation 18, we next fit the expected emission profile  $T_{exp}(\nu)$  to the sum of the emission from the CNM and WNM. For the CNM, the brightness temperature of the assembly of CNM components is

$$T_{B,CNM}(\nu) = \sum_0^{N-1} T_{s,n} (1 - e^{-\tau_n(\nu)}) e^{-\sum_0^{M-1} \tau_m(\nu)}, \quad (19)$$

where the subscript  $m$  with its associated optical depth profile  $\tau_m(\nu)$  represents each of the  $M$  CNM clouds that lie in front of cloud  $n$ . This fit yields values for  $T_{s,n}$ . For multiple absorption components, as part of the least-squares fit process we experiment with all possible orders along the line of sight and choose the one that yields the smallest residuals.

For the WNM, we assume that the intrinsic, unabsorbed emission profile is represented by a set of  $K$  Gaussians. We also include the absorption of each WNM component by the CNM by assuming that a fraction  $\mathcal{F}_k$  lies in front of all the CNM and is unabsorbed, with the rest all lying behind; thus

$$T_{B,WNM} = \sum_0^{K-1} [\mathcal{F}_k + (1 - \mathcal{F}_k) e^{-\tau(\nu)}] T_{0,k} e^{-[(\nu - \nu_{0,k})/\delta\nu_k]^2}, \quad (20)$$

where the subscript  $k$  represents each WNM component. This fit yields values for  $T_{0,k}$ ,  $\nu_{0,k}$ , and  $\delta\nu_k$ . We also experiment with determining  $\mathcal{F}_k$  from the fit as discussed in §3.4. Note that  $T_{0,k}$  is a brightness temperature, not a kinetic temperature; for component  $k$ , the intrinsic unabsorbed emission profile is  $T_{B,WNM,k} = T_{0,k} e^{[(\nu - \nu_{0,k})/\delta\nu_k]^2}$ . In fitting  $T_{exp}(\nu) = T_{B,CNM}(\nu) + T_{B,WNM}(\nu)$ , we usually find that  $\mathcal{F}_k$  is indeterminate and we can only distinguish between the two extremes  $\mathcal{F}_k = (0, 1)$ . The differences between the  $\mathcal{F}_k = 0$  and 1 profile variances ( $\sigma^2$  of the data points from the fit) are usually not statistically significant but nevertheless lead to differences in the derived CNM temperatures. These differences reflect the uncertainties in  $T_{s,n}$  more than the conventional errors derived from least squares fits.

### 3.4. Permuting CNM components and trying different $\mathcal{F}$ for WNM components

For the CNM components,  $T_{B,CNM}(\nu)$  depends on the order of the components along the line of sight. The ordering is a discrete quantity and cannot be solved for using the standard least-squares technique. Rather, we must try solutions for different orderings and compare the variances  $\sigma^2$  from the residuals of the fits. For  $N$  CNM components there are  $N!$  possible orderings. However, some of these are extraneous because changing the order only matters for clouds whose profiles overlap in velocity. Thus, we define the quantity  $N_x$  such that there are  $N_x!$  possible orderings of *overlapping* CNM components. Obviously,  $N_x \leq N$ , and if  $N > 0$ , then  $N_x \geq 1$ ;  $N_x$  cannot be zero because a component overlaps with itself. In our data set, the smallest value of  $N_x$  ranges from 1 to 5 (with 120 possible orderings). The statistics are:  $(N_x, \text{number of sources}) = (1, 25), (2, 19), (3, 12), (4, 2), (5, 6)$ ; 15 sources have no detectable CNM components.

For the WNM components,  $T_{B,WNM}$  depends on the values of  $\mathcal{F}_k$ .  $\mathcal{F}_k$  can, in principle, be determined by least squares. However, only rarely are the the variances sufficiently sensitive to  $\mathcal{F}_k$  for least squares to work. Even though the variances are insensitive, the derived parameters (such as the associated CNM spin temperatures and the CNM and WNM HI column densities) depend on the  $\mathcal{F}_k$ .

Therefore, we explore the range of each WNM's  $\mathcal{F}_k$  by calculating the results for three values,  $\mathcal{F}_k = (0, 0.5, 1)$ . There are  $K$  WNM components and we consider all possible combinations, which is  $3^K$ . However, some of these are extraneous because the value of a WNM component's  $\mathcal{F}_k$  only matters if the component's profile overlaps an absorbing CNM component. Thus, we define the quantity  $K_x$ , which is the number of such WNM Gaussian components. The statistics are:  $(K_x, \text{number of sources}) = (1, 28), (2, 33), (3, 2), (4, 1)$ ; 15 sources have no detectable CNM components, so  $K_X = 0$ .

For any given source, the total number of trial least square fits is  $[N_x! 3^{K_x}]$ . The two sources with the largest total number are 3C138 and 3C409, both with  $N_x = 5$  and  $K_x = 2$  and 1080 total trials. Most sources have many fewer trials.

$\mathcal{F} = 0$  means that the WNM lies behind the CNM so that the WNM'S emission is absorbed. This means that the CNM must make up for the missing WNM emission, so the least-square-fitted spin temperatures are always higher for  $\mathcal{F} = 0$  than for  $\mathcal{F} = 1$ . Also, the fitted WNM brightness tends to be larger for  $\mathcal{F} = 0$  than for  $\mathcal{F} = 1$ , but this is a smaller effect. The other WNM parameters, central velocity and width, are only marginally sensitive to  $\mathcal{F}_k$ . Of course, the WNM parameters are completely insensitive to the CNM component ordering, because we assume that  $\mathcal{F}_k$  is the same for all CNM components.

### 3.5. Calculating the physical parameters

For most sources, the variances don't change very much among the various trials. Typically these changes are less than 20%, and this is not enough to distinguish one particular trial as being significantly better than others. (Occasionally the changes are much bigger; we discuss these two sources below.) However, the derived physical parameters such as spin temperature and HI column density do change significantly among the trials. We derive a value and error for each physical parameter by taking a weighted average over all trials. The weight of each trial is the reciprocal of the variance  $\sigma^2$  computed from the residuals to the fit to  $T_{exp}(\nu)$ .

For example, consider the spin temperature of a particular CNM component for a source having  $F$  trial least-square fits; normally  $F = [N_x! 3^{K_x}]$ , but for some sources some fits don't converge and  $F$  is smaller. Let  $T_{s,f}$  be the spin temperature derived for fit  $f$  and  $w_f = (1/\sigma_f^2)$  be the trial fit's weight. Then we derive the mean spin temperature  $\langle T_s \rangle$  and its variance  $\sigma_{\langle T_s \rangle}^2$  by the usual weighted average

$$\langle T_s \rangle = \frac{\sum_{f=0}^{F-1} w_f T_{s,f}}{\sum_{f=0}^{F-1} w_f} \quad (21a)$$

$$\sigma_{\langle T_s \rangle}^2 = \left[ \frac{\sum_{f=0}^{F-1} w_f [(T_{s,f} - \langle T_s \rangle)^2 + \sigma(T_{s,f})^2]}{\sum_{f=0}^{F-1} w_f} \right] \left[ \frac{F}{F-1} \right] \quad (21b)$$

Here  $\sigma(T_{s,f})^2$  is the variance of  $T_{s,f}$  in the least squares fit number  $f$ ; it accounts for the intrinsic uncertainty in that particular fitted value for  $T_{s,f}$ .

Normally one would then define the uncertainty in  $\langle T_s \rangle$  as  $\Delta \langle T_s \rangle = [\sigma_{\langle T_s \rangle}^2 / F]^{1/2}$ . However, this is not appropriate for our case. This usual definition makes two assumptions: one, that the residuals from the average, i.e.  $[T_{s,f} - \langle T_s \rangle]$ , are distributed randomly about the mean; and two, that the mean is the same for all data. Neither assumption is valid here. The mean varies systematically with  $\mathcal{F}_k$  and tends to adopt three distinctly different values, corresponding to the three trials of  $\mathcal{F}_k$ , with small fluctuations about those values. A better representation of the uncertainty  $\Delta \langle T_s \rangle$  is the spread among the three values of  $T_{s,f}$ . A good approximation to this is simply

$$\Delta \langle T_s \rangle = \sigma_{\langle T_s \rangle} \quad (21c)$$

This description applies to all physical parameters including HI column densities, except that we do not include the term  $\sigma(N_f(HI))^2$  in equation 21b.

Finally, we consider the most likely value  $\langle \mathcal{F}_k \rangle$ . Again, each of the three trial values of  $\mathcal{F}_k$  has  $N_x!$  least square fits, each with variance  $\sigma_f^2$ . We again take a weighted average, as above in equation

21. However, in this case the residuals are more nearly randomly distributed about a single mean. Accordingly, we define the uncertainty  $\Delta\langle\mathcal{F}_k\rangle$  as

$$\Delta\langle\mathcal{F}_k\rangle = \left[ (\sigma_{\langle\mathcal{F}_k\rangle}^2 / N_x!) \right]^{1/2} \quad (22)$$

This equation deserves a small elaboration. Consider the case where there is no favored  $\mathcal{F}_k$ , i.e. where the the variances for all three choices  $\mathcal{F}_k = (0, 0.5, 1)$  are equal. Then we derive  $\langle\mathcal{F}_k\rangle = 0.5$ ,  $\Delta\langle\mathcal{F}_k\rangle = 0.29$ . This is the maximum  $\Delta\langle\mathcal{F}_k\rangle$ ; in practice the variances don't change much with  $\mathcal{F}_k$  so that all sources have  $\Delta\langle\mathcal{F}_k\rangle$  almost this large and, concomitantly,  $\langle\mathcal{F}_k\rangle \sim 0.5$ .

### 3.6. Limits on Opacities and Spin Temperatures for WNM Components

In addition to parameters estimated directly from the least squares fits, we can also place limits on the peak opacity and spin temperature of each WNM component  $k$ . First, we can estimate an *upper* limit to the peak opacity  $\tau_{0,k}$ . We do so by considering both the intrinsic uncertainty in the opacity profile  $\Delta e^{-\tau(\nu)}$  (equation 12d; downward-going solid line in the bottom panel of the two-panel plots) and the residuals from the fit of the CNM components to the opacity profile (solid line near mid-profile height in the bottom panel of the two-panel plots). These estimates are upper limits in the sense that higher values of  $\tau_{0,k}$  would produce WNM features in the opacity profiles that are greater than the errors in our measurements. In Table 2, column 2 we list these upper limits on  $\tau_{0,k}$  for WNM components. (See §4 for a description of this table.) This upper limit, being visually estimated, is very uncertain; its error is not quoted, but realistically the error is large, something like half its value.

The above upper limit on  $\tau_{0,k}$  imply a *lower* limit on  $T_{s,k}$ , because  $T_{s,k} = \frac{T_{0,k}}{\tau_{0,k}}$  for a WNM component. We list these lower limits for the WNM components in Table 2, column 5 and as TSMIN in the upper panels of the two-panel plots such as Figure 3.

Finally, we can estimate *upper* limits on on the kinetic temperatures of Gaussian components from the fitted line widths of WNM (and CNM) components. We define this limit as  $T_{kmax} = 21.86\Delta V^2$ . This parameter is listed in Table 2, column 6. For WNM components,  $T_{kmax}$  also implies a *lower* limit on  $\tau_{0,k}$ .

## 4. GAUSSIAN COMPONENTS AND OUR DATA

### 4.1. Gaussian parameters in tabular form and graphical form

We present the numerical results of our fits in Table 2. The opacity and expected profiles, together with other desiderata are described in §2.8.

1. Column 1:  $T_B$  is the intrinsic peak brightness temperature of the component. For WNM components it is equal to the unabsorbed central height of the emission Gaussian  $T_{0,k}$  (see equation 20) and its error is derived as discussed in §3.5. For CNM components,  $T_B$  is equal to the spin temperature  $T_{s,n}$  times  $(1 - e^{-\tau_{0,n}})$  (see equations 18 and 19) and its error is not quoted.
2. Column 2:  $\tau$  is the central opacity of the component. For CNM components, it is  $\tau_{0,n}$  from equation 18, derived directly from the least squares fit to the opacity profile. For WNM components it is the upper limit to peak opacity  $\tau_{0,k}$ , estimated by eye (§3.6), and has a very large error.
3. Column 3:  $V_{LSR}$  is the central VLSR in  $\text{km s}^{-1}$ .
4. Column 4:  $\Delta V$  is the Gaussian FWHM  $\text{km s}^{-1}$ .
5. Column 5:  $T_s$  is the spin temperature. For CNM components it is derived from the fit to the expected profile; its error is derived as discussed in §3.5. For a few CNM components,  $T_s$  had to be forcibly set to zero to attain convergence of the fit to the expected profile. For WNM components  $T_s$  is a lower limit (§3.6), and has a very large error; this is TSMIN in the two-panel plots.
6. Column 6:  $T_{kmax}$  is the kinetic temperature of a component if there were no nonthermal broadening;  $T_{kmax} = 21.86\Delta V^2$ .
7. Column 7:  $N(HI)_{20}$  is the HI column density in units of  $10^{20} \text{ cm}^{-2}$ . For the few CNM components with  $T_s = 0$ , we assign  $N(HI) = 0$ .
8. Column 8: For WNM components.  $\mathcal{F}$  is the weighted average of  $\mathcal{F}$ , calculated as described in §3.5. For CNM components, O is equal to the order of the component along the line of sight, beginning with 0; increasing numbers mean increasing distance along the line of sight. This order is the one for which the variance from the fit to the emission spectrum is smallest. For CNM components, no error is given.
9. Column 9:  $l/b/SOURCE$  are the Galactic longitude, latitude, and source name.

## 4.2. The process of fitting Gaussians

First, we remark that the astronomically popular activity of fitting Gaussians to spectral profiles is based on the assumption that velocity profiles are, indeed, characterized by Gaussians. This is necessarily true when the damping wings are insignificant, as for the 21-cm line, and when there are no nonthermal motions. However, most of our Gaussian components have linewidths  $T_{kmax} > T_s$ , so that the line shape is determined by nonthermal motions. Unless the nonthermal motions consist of a large number of turbulent elements, so that the central limit theorem applies,

there is no known reason why a component’s shape need be Gaussian. Nevertheless, both the opacity and expected profile of most sources are easily decomposed into Gaussians, so whether or not this model is physically correct it works empirically and is convenient—and besides, how else would one proceed?

Gaussian functions are not orthogonal, so our Gaussian fits are not unique. Rather, they reflect our subjective judgment in selecting the number of Gaussian components and other biases. Here we describe our approach to this subjective procedure, a procedure based on the equations of §3.3.

For each source we begin by fitting Gaussians to the opacity spectrum (equation 18; we call these the “CNM Gaussian components”). Our approach is to use the minimum number of components required to make the residuals of the fit comparable to or smaller than the errors derived as discussed in §2.7. After fitting the opacity components, we fit the expected profile by simultaneously (1) fitting the intensities of the opacity components (whose centers and widths are fixed) and (2) adding one or more “WNM Gaussian components”, which contribute to the expected profile but not to the opacity profile. This fit to the expected profile is a fit to the sum of equations 19 and 20.

For the WNM we again use the minimum number of WNM components. However, in this case the criterion involves reducing the residuals of the fit to a “reasonable” level instead of to the much smaller level of the derived errors. The reason is that the WNM components are derived from the observed expected profile, and this is subject to an unaccounted-for source of error, namely the contribution of HI emission from directions outside the main telescope beam. In fact, almost half of the response of the Arecibo telescope to an extended source, such as the 21-cm line, comes from outside the main beam (Heiles et al 2001a). These directions are likely to contain velocity components that are unrelated to those within the main beam, or have Gaussian parameters that are modified by angular derivatives.

Consequently, when fitting the expected profile we use our subjective judgment in deciding how many WNM components to fit. Almost always this number is small, consisting of one or two fairly narrow WNM components often sitting on top of a much weaker, broader one. Below we present and discuss a number examples to illustrate our approach and our subjective definition of what is “reasonable”.

During the fitting process we were concerned about “stray radiation”, which is radiation entering the telescope from distant sidelobes. This can produce unreal features in observed emission spectra. These are usually broad and could cause us to fit weak, broad WNM Gaussians that are unrelated to the gas in direction observed. For each source we compared the tails of our expected profiles  $T_{exp}(\nu)$  with the nearest profile of the Leiden-Dwingeloo survey (Hartmann and Burton 1997). We were gratified—and somewhat surprised in view of Arecibo’s substantial aperture blockage (Heiles et al 2001a)—to find that the differences between the intensities in the profile wings for the two datasets are completely negligible. This implies that Arecibo’s significant sidelobes all lie close to the direction of the main beam. Thus, our HI column densities, even for the weak, broad



WNM components, are quite reliable.

### 4.3. Optical lines versus the 21-cm line

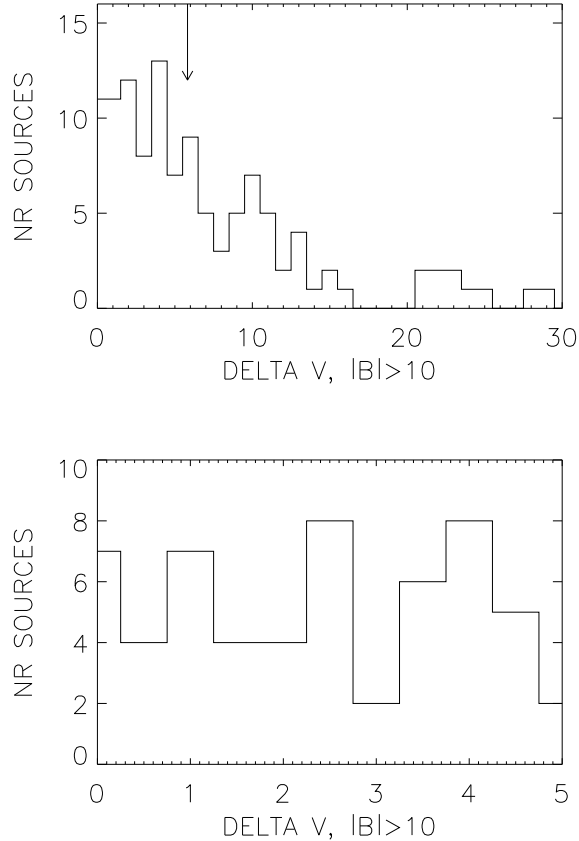


Fig. 4.— Histogram of the velocity separations between adjacent CNM Gaussians. The lower panel is an expanded version.

Our results should be comparable to the results from optical absorption lines of minority ionization species such as KI because both sample the CNM. The 21-cm line opacity  $\propto N(\text{HI})T_k^{-1}$ . The KI opacity is approximately  $\propto N(\text{KI})$ ; under ionization equilibrium,  $N(\text{KI}) \propto N(\text{HI})PT^{-1.7}$ , where  $P$  is the CNM pressure, which is typically  $(P/k) = 2250 \text{ cm}^{-3} \text{ K}$  (Jenkins & Tripp 2001). Thus optical absorption lines are biased towards low temperatures even more than the 21-cm line is.

Optical interstellar absorption lines sample heavy elements, which have smaller thermal motions than HI, so they might reveal multiple narrow components where we might resolve only one.

If we take the results at face value, then this is indeed occurring. Figure 4 exhibits the histogram of velocity separations between adjacent CNM Gaussian components. Welty and Hobbs (2001; WH) present the same histogram for KI optical absorption line components in their Figure 16. Their histogram has a pronounced peak centered at about  $1.8 \text{ km s}^{-1}$ , falling to zero below  $0.7 \text{ km s}^{-1}$  and becoming small above  $3 \text{ km s}^{-1}$ . In contrast, ours is roughly flat from 0 to  $5 \text{ km s}^{-1}$ . They discuss their histogram in terms of a continuous distribution of closely-spaced components, and the difference between our histogram and theirs could be a result of blending.

However, we have lingering doubts about the reality of some of their closely-spaced components. In some cases they need several components to reduce the residuals to their noise level; in other cases they do not. To us, their sample of closely-spaced components seems inconsistently nonuniform. Looking at their Table 1, many stars have closely-spaced components and many do not (defined as  $< 1.9 \text{ km s}^{-1}$  for this discussion). For example,  $\omega^1\text{Sco}$  at  $(l, b) = (352.8^\circ, 22.8^\circ)$  has 4 while the fairly nearby  $1\text{Sco}$  at  $(346.1^\circ, 21.8^\circ)$  has none; the two stars have comparable visual line profiles and extinctions  $E(B - V) = (0.22, 0.19)$  mag, respectively. Are conditions really that different towards the two stars, or is the presence of multiple closely-spaced components a vagary of small departures from idealized Gaussian line shapes and subjective judgment?

We asked this question above about our own Gaussians in §4.2 and the question applies equally to the optical data. The KI line profiles are always dominated by nonthermal motions, because even the multiple closely-spaced components have nonthermal line widths. WH prefer to decompose the line shapes by inserting multiple Gaussian subcomponents (actually, Voigt subcomponents) until the residuals are equal to the noise. This is a valid mathematical description of the profile, although it is not unique—but is it a valid *physical* description? We repeat, there is no physical reason to assume that turbulent broadened profiles are, in fact, Gaussian, unless the number of subcomponents is so large that the central limit theorem applies.

In our opinion, the use of many subcomponents to represent a profile peak might, but does not necessarily, describe the physical world.

#### 4.4. Errors incurred from fitting too many/too few Gaussians

The nonuniqueness of Gaussian fitting means that we might sometimes fit opacity profiles with too many or too few Gaussians. For example, perhaps the multiple closely-spaced components of WH are physically real. Here we discuss how this affects our derived spin temperature  $T_s$ .

##### 4.4.1. The low- $\tau(\nu)$ case

We assume  $\tau = (1 - e^{-\tau})$ , which is valid for  $\tau(\nu) \lesssim 1$ . Whether we fit  $N$  overlapping Gaussians, or fit only one when  $N$  are required in the physical world, we always require agreement with the

data, i.e.

$$\sum_0^{N-1} \tau(\nu)_n = \tau(\nu) \quad (23a)$$

$$\sum_0^{N-1} T_{s,n} \tau(\nu)_n = T_{exp}(\nu) \quad (23b)$$

where  $n$  represents each Gaussian and the quantities on the right are the observed ones. The easiest way to satisfy this combined requirement on both sums is for  $T_{s,n}$  to be the same for all components, and this makes  $T_s$  independent of  $N$ . If  $T_{s,n}$  changes with  $n$ , then the values should cluster around the  $n$ -independent one. Therefore, derived spin temperatures for all the Gaussian components are not sensitive to the number of fitted Gaussians  $N$ .

The same cannot be said of the velocity widths and integrated areas of the Gaussians. If we fit Gaussian-shaped opacity and expected profiles with multiple blended Gaussians, then the widths ( $T_{kmax}$ ) and areas ( $N(HI)$ ) necessarily decrease with  $N$ .

#### 4.4.2. The high- $\tau(\nu)$ case

The high- $\tau(\nu)$  case is harder to treat because the emission is nonlinearly related to  $\tau$ . Here we consider a simple model in which  $N$  clouds of identical  $\tau(\nu)$  and  $T_s$  lie behind each other. In this case, equation 23a remains valid but equation 23b becomes a simpler version of equation 19 with all  $T_{s,n} = T_s$  and all  $\tau(\nu)_n = \tau$ , namely

$$T_{exp}(\nu) = T_s \sum_0^{N-1} (1 - e^{-\tau(\nu)}) e^{-\sum_0^{M-1} \tau(\nu)}, \quad (24)$$

One can manipulate this equation to show that  $T_s$  is independent of  $N$ , as it is for the low-opacity case. Thus again, for this illustrative model the derived spin temperature is unaffected by the number of components that represent the profile.

## 4.5. Fitting the opacity profiles: CNM Gaussian components

### 4.5.1. Sources for which the CNM fits are fairly unambiguous

For many sources either a single Gaussian or multiple ones that don't overlap are sufficient (i.e.,  $N_x = 1$ ); examples are 3C315 and 3C207, shown in Figures 17 and 18 below. These cases are unambiguous and there is very little room for mistakes, except for the possibility that each

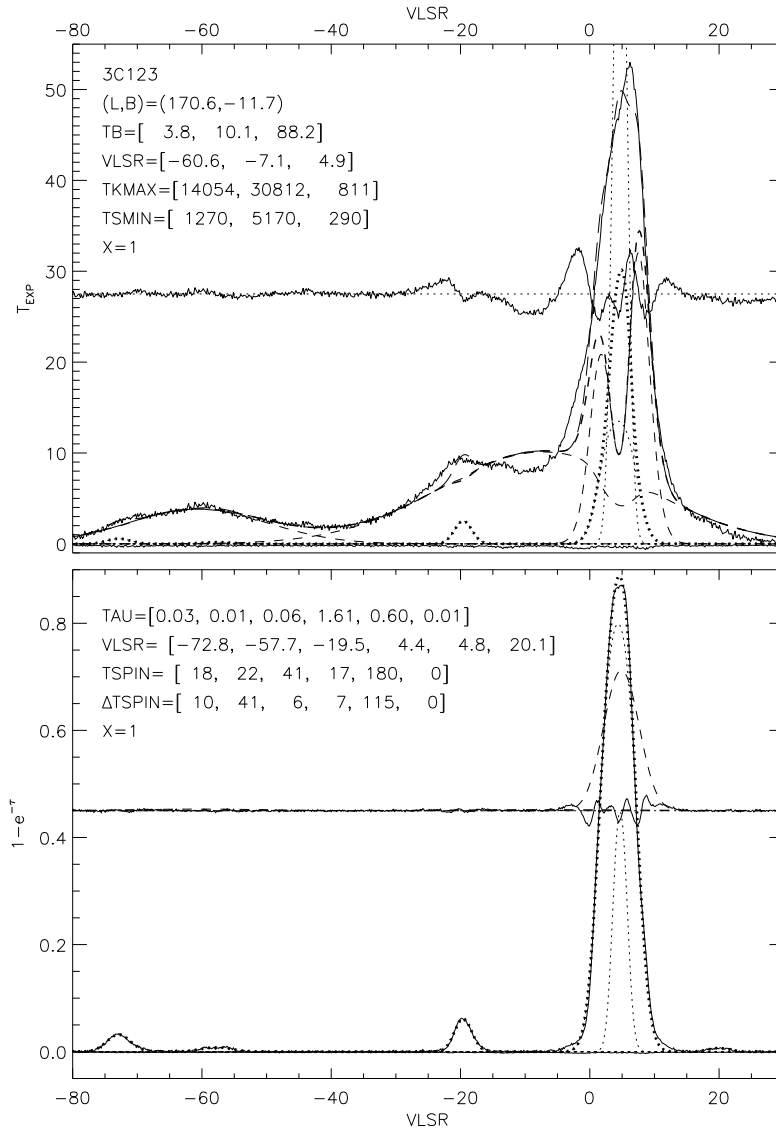


Fig. 5.— Data for 3C123. Profile uncertainties are invisible because the source is strong. For a complete description of this figure, see Figure 3, §2.8, and §4.1.

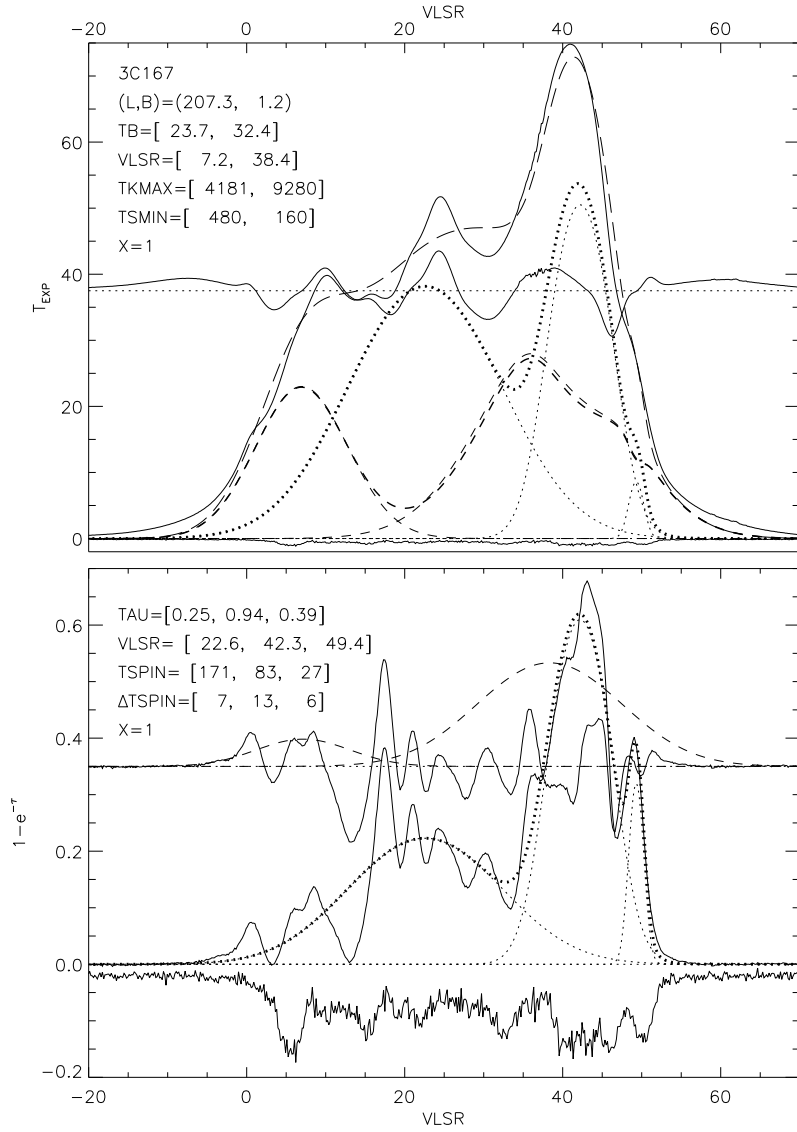


Fig. 6.— Data for 3C167. For a complete description of this figure, see Figure 3, §2.8, and §4.1.

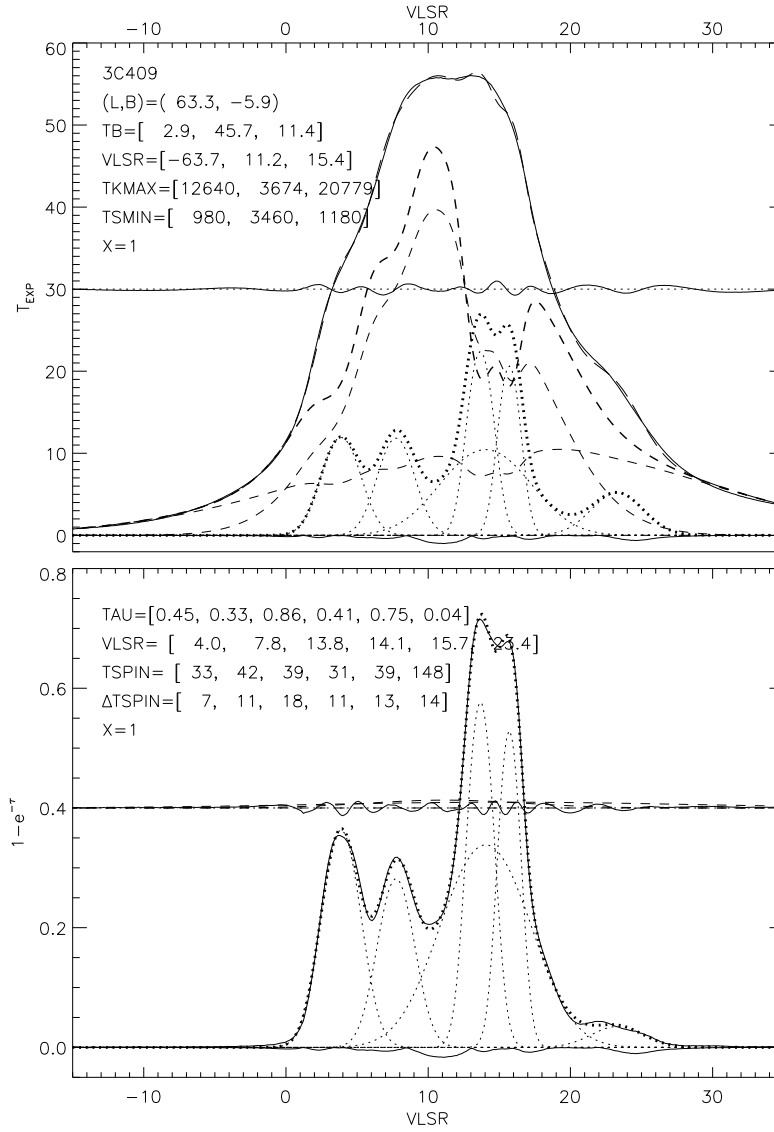


Fig. 7.— Data for 3C409. For a complete description of this figure, see Figure 3, §2.8, and §4.1.

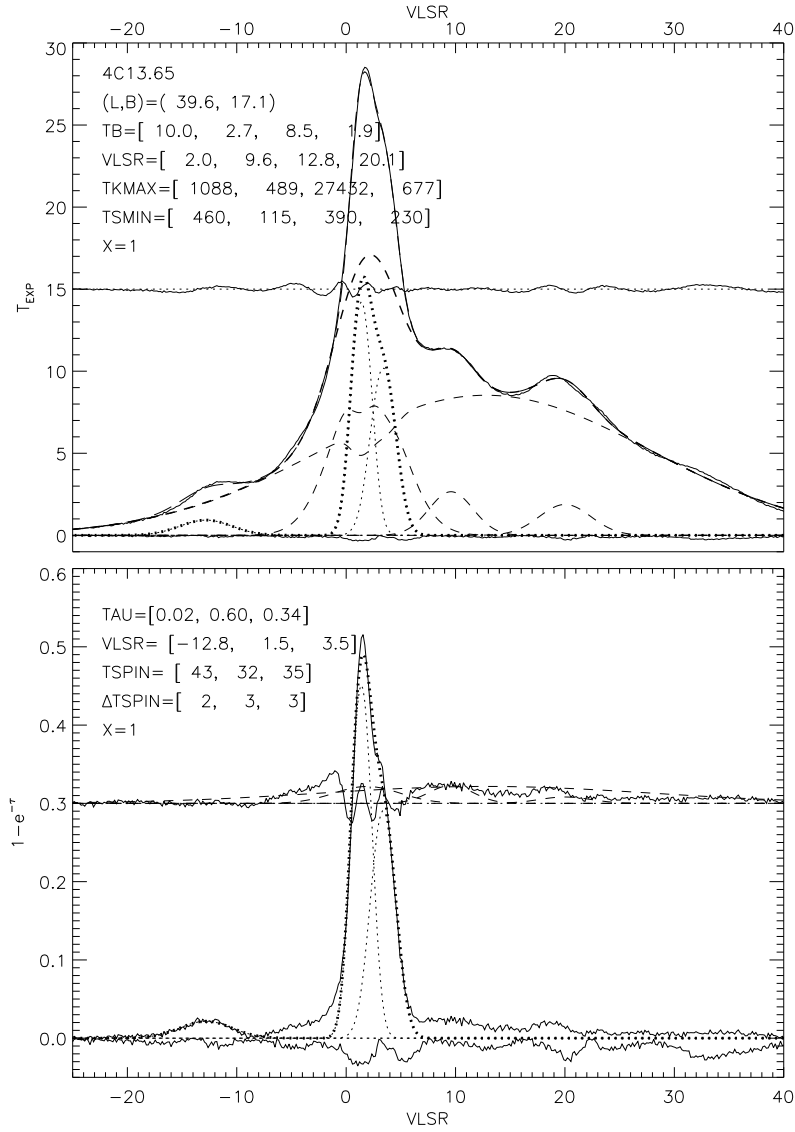


Fig. 8.— Data for 4C13.65. For a complete description of this figure, see Figure 3, §2.8, and §4.1.

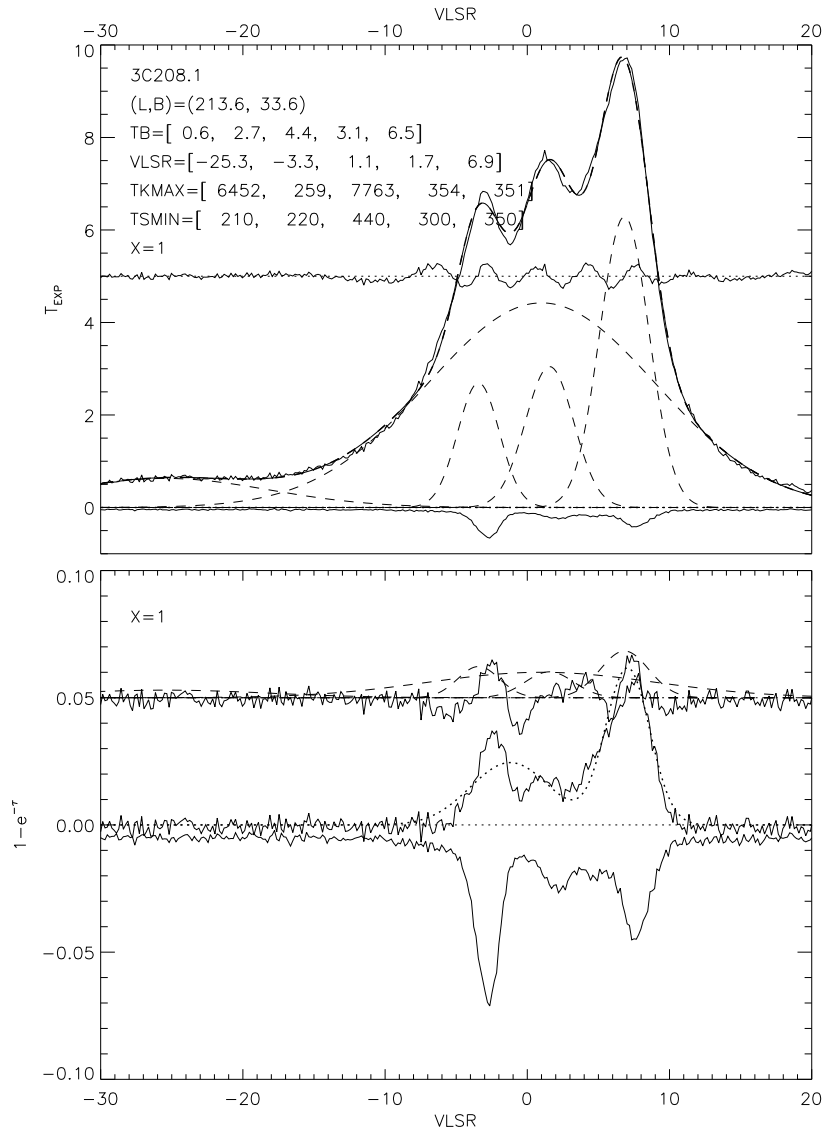


Fig. 9.— Data for 3C208.1. For a complete description of this figure, see Figure 3, §2.8, and §4.1.



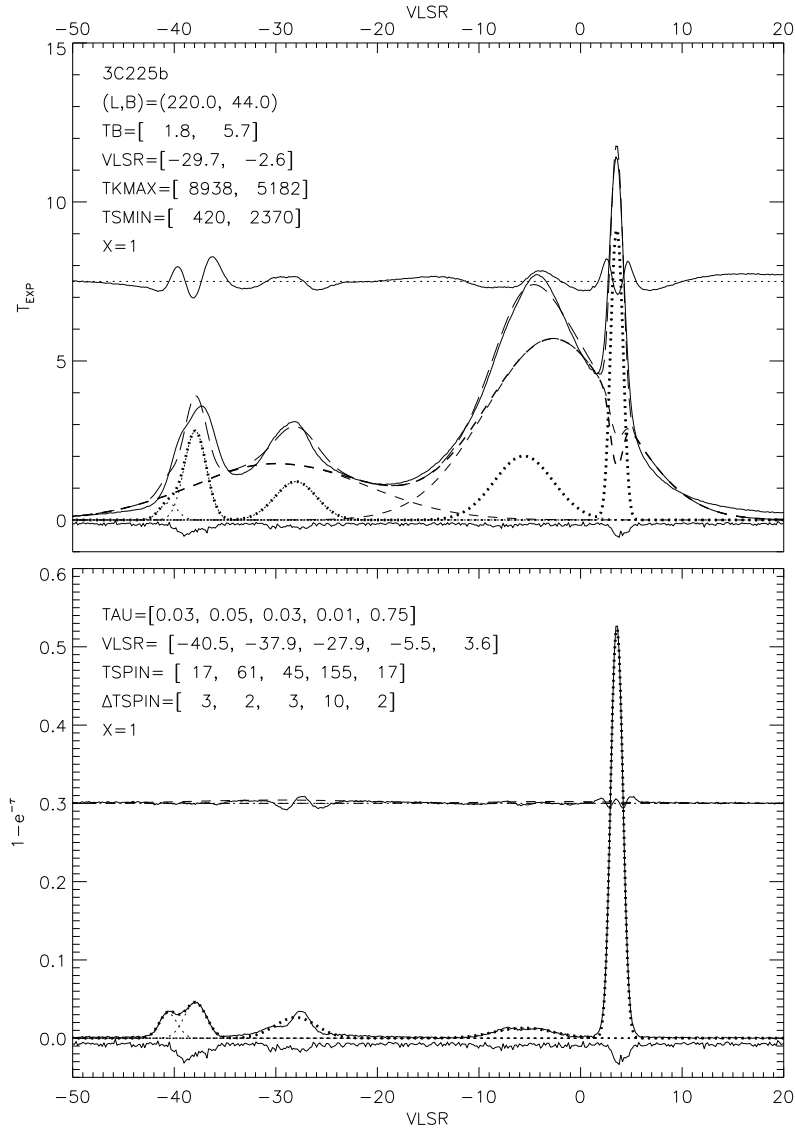


Fig. 10.— Data for 3C225b. For a complete description of this figure, see Figure 3, §2.8, and §4.1.

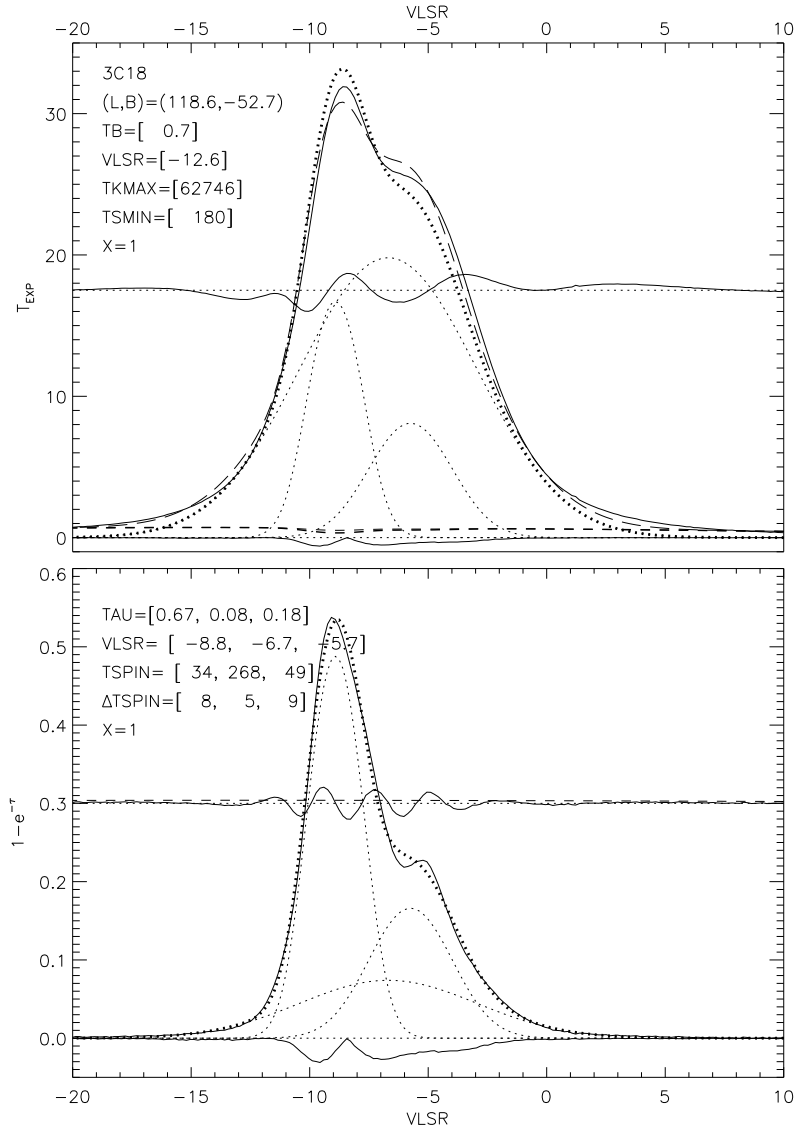


Fig. 11.— Data for 3C18. For a complete description of this figure, see Figure 3, §2.8, and §4.1.

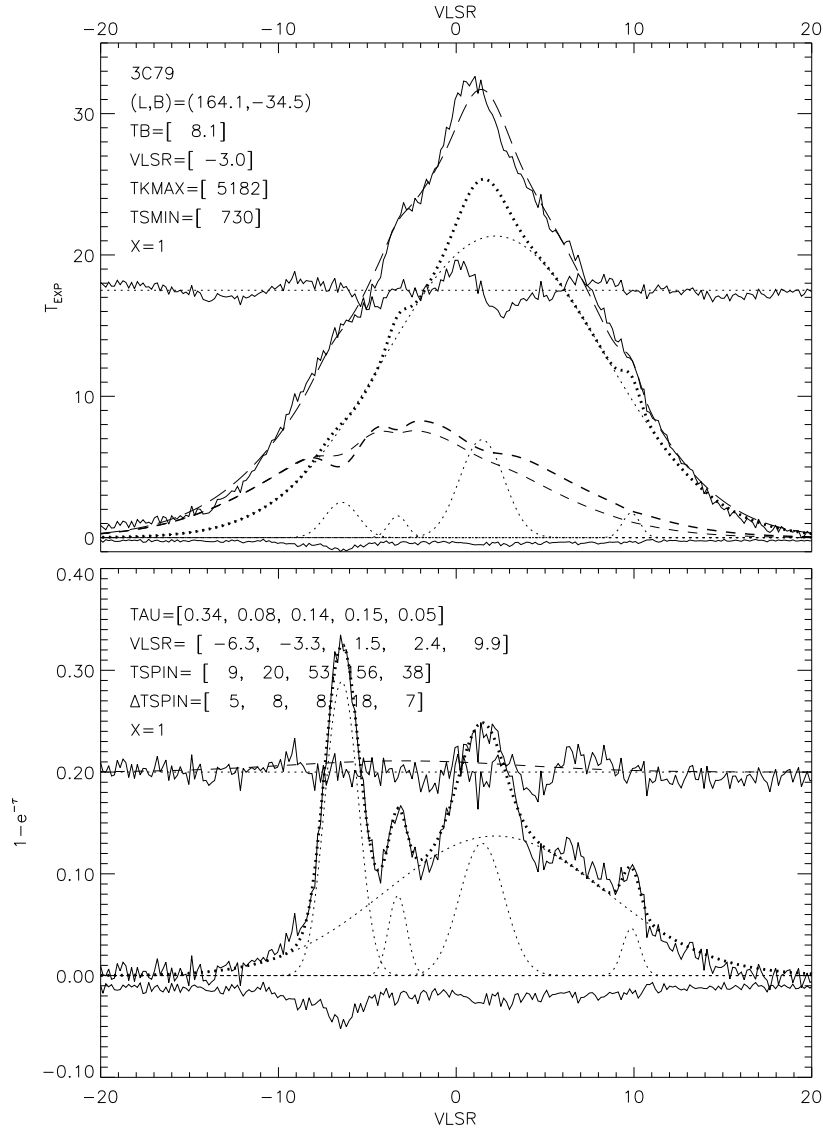


Fig. 12.— Data for 3C79. For a complete description of this figure, see Figure 3, §2.8, and §4.1.

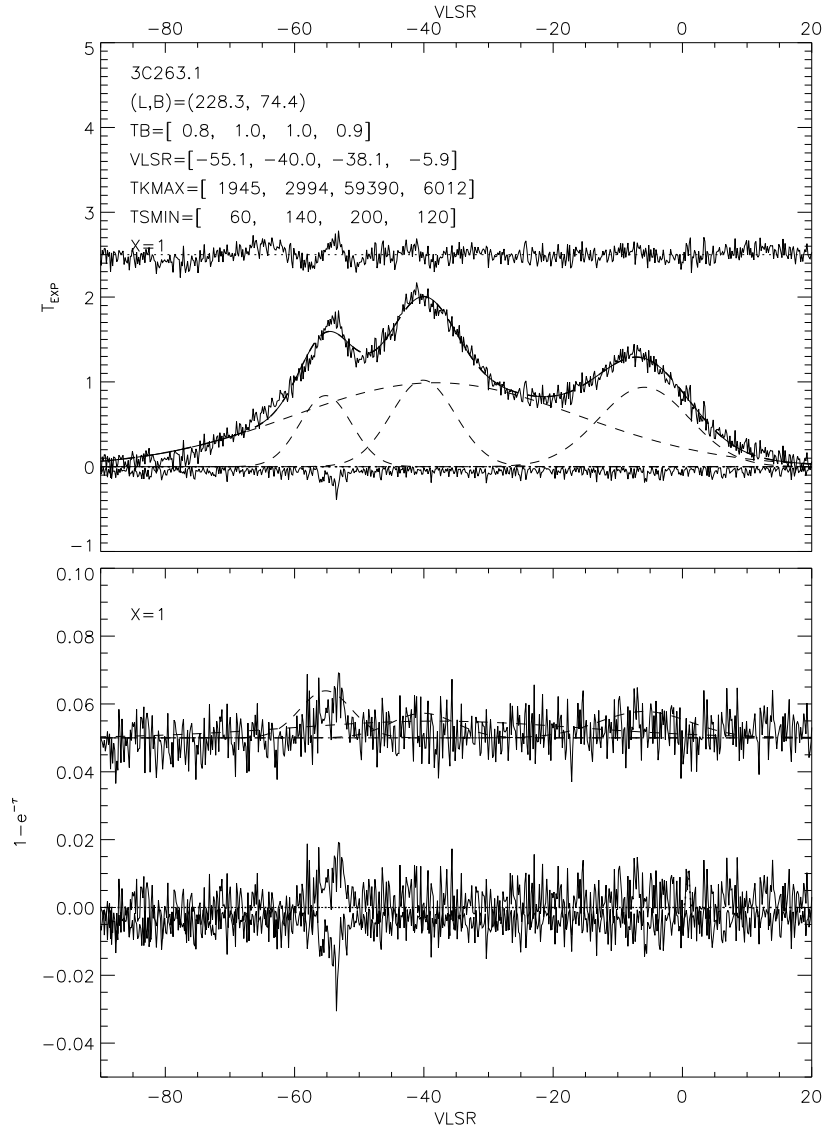


Fig. 13.— Data for 3C263.1. For a complete description of this figure, see Figure 3, §2.8, and §4.1.

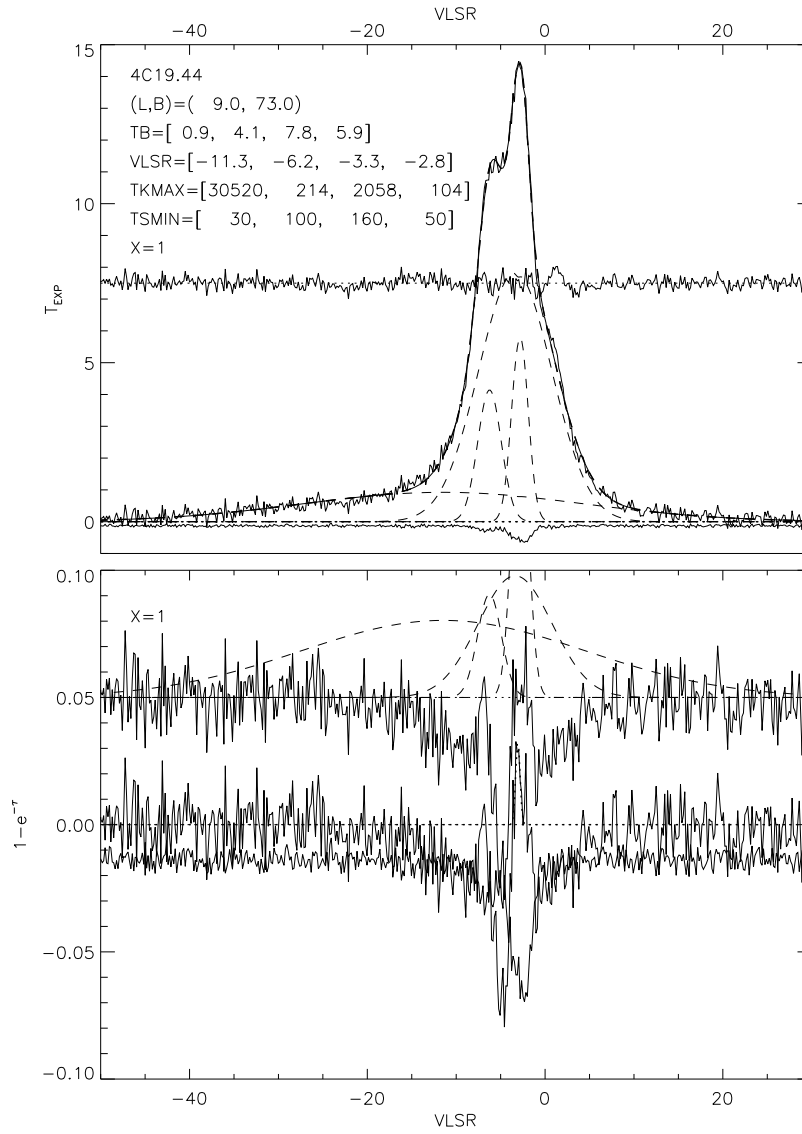


Fig. 14.— Data for 4C19.44. For a complete description of this figure, see Figure 3, §2.8, and §4.1.

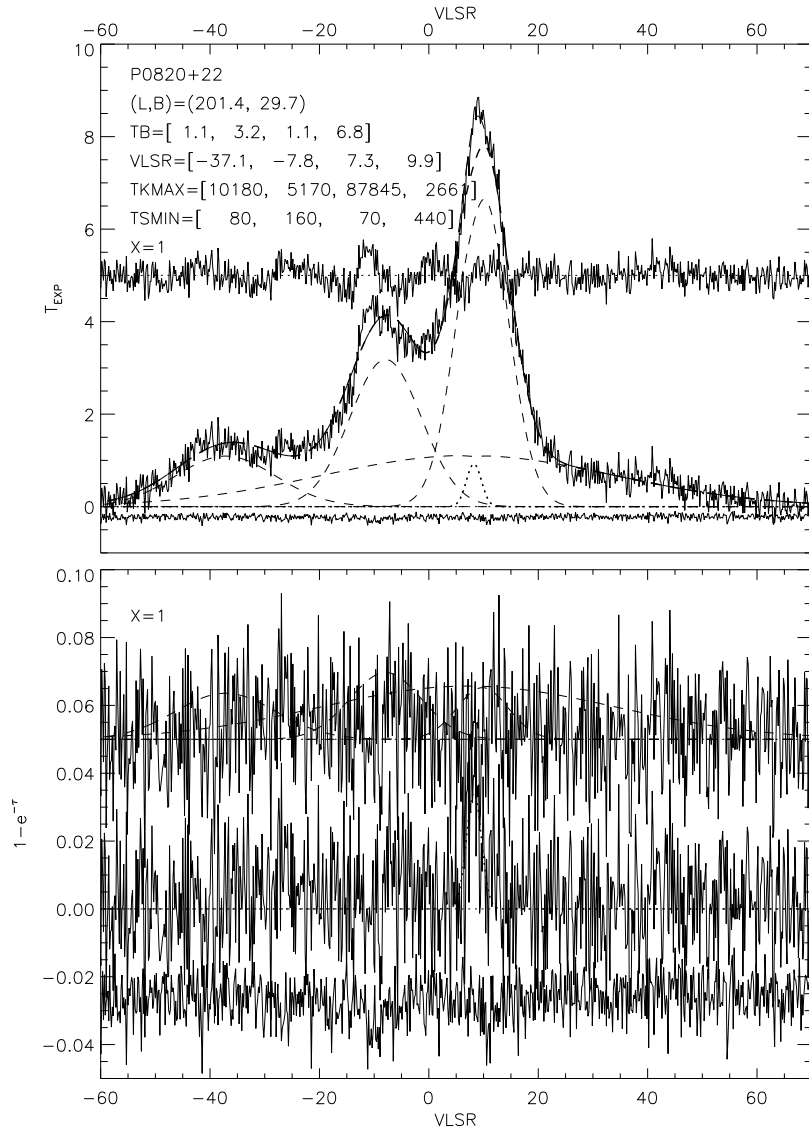


Fig. 15.— Data for P0820+22. For a complete description of this figure, see Figure 3, §2.8, and §4.1.

Gaussian really consists of more than one narrower and/or weaker ones. 26 out of the 62 sources having CNM components fall into this unambiguous category.

Many sources have overlapping Gaussians. Examples are 3C120 and P0531+19, shown in Figures 16 and 19 (these are presented below because their main focus is in later discussion). For 3C120 we use three Gaussians and achieve residuals that are considerably smaller than the errors; this exceeds the requirement of a good fit. However, two Gaussians produce residuals that vastly exceed the errors, so three Gaussians is the correct choice. We have not been able to fit three Gaussians with other parameters than those given, so the validity of this fit seems secure. P0531+19 has two distinctly separated narrow peaks connected by a nonzero broad region and is fit well by two narrow and one broad Gaussians. Three Gaussians are certainly required and, again, no other combination of Gaussians works, so this seems the correct solution.

#### 4.5.2. Sources for which the CNM fits are more ambiguous or difficult

3C123 (Figure 5) is a good example of two difficulties. One is overlapping opacity components, which make the uniqueness of a fit less certain; in the case of 3C123, the overlapping components are indistinguishable, making a true fit impossible. 3C123 is a very strong source, so its opacity spectrum has small errors and imperfections of the fit reveal small inadequacies. The main opacity peak has ( $\tau_0 = 1.60 \pm 0.03$ ) and, when fit with a single or even a “reasonable number” of Gaussians, has residuals that vastly exceed the errors. We believe that the main absorption peak consists of several overlapping narrow components, which are degenerate in the fitting process. 3C123 lies near a molecular cloud in the Taurus/Perseus region and even exhibits OH absorption, which is rare for our sources. 3C123 has at least three narrow OH absorption components ( $\Delta V = 0.5$  to  $1.4$  km s<sup>-1</sup>) in the velocity range 2 to 7 km s<sup>-1</sup> (Troland & Heiles, in preparation; Crutcher, Troland, & Heiles 1981). Each of these is likely to have associated HI, producing overlapping narrow HI components.

An additional problem with 3C123 is its 20.0 km s<sup>-1</sup> CNM component: the least squares fit to the expected profile would not converge unless its spin temperature was forced to zero. Its opacity  $\tau_0 = 0.007 \pm 0.002$ , which is very small, and we suspect that this component occupies a small solid angle, absorbing a small fraction of 3C123 continuum and contributing insufficient 21-cm line brightness to be detected. The same situation occurs for two opacity components in 3C273.

Sources near the Galactic plane (defined here as  $|b| < 10^\circ$ ) have complicated absorption spectra and cannot always be fit in a reasonable way; 3C167 (Figure 6) is an example, others being 3C141.0, T0526+24, T0556+19, T0629+10). On the other hand, some low- $|b|$  sources are well-fit: for example, 3C409 (Figure 7) is exceedingly well-fit, seemingly unambiguously, by 6 Gaussians; others (not quite so well fit) include 3C154, 4C13.67, 4C22.12, P0531+19, 3C138. Intermediate cases are 3C131, 3C133, 3C410.

#### 4.6. Fitting the expected profiles: WNM Gaussian components

We thoroughly discuss two example cases, 3C120 and 3C138, in detail in §4.7. Here we present some examples and describe them only briefly.

##### 4.6.1. Sources for which WNM fits are fairly unambiguous

Sometimes only a single WNM component is required (e.g. P0531+19, Figure 19). More often two are required, one a broad, weak one to fit the wings of the line and the other a much more intense and narrow component to fill in the emission line, e.g. 3C207 and 3C315 (Figures 18, 17). Sometimes additional nonoverlapping WNM components at different velocities are required, e.g. 3C120 (Figure 16). All these cases are straightforward and unambiguous. More complicated WNM cases include, of course, sources near the Galactic plane, and also others. Many complicated cases are nevertheless well-fit, including those listed above as being unambiguously fit with CNM Gaussians.

##### 4.6.2. Sources for which the WNM fits are more ambiguous or difficult

Some sources away from the plane are remarkably complicated: 4C13.65 (Figure 8) has a broad WNM component with several narrower ones within; it is complicated but the Gaussian process seems fairly secure. 3C208.1 (Figure 9) has no reliable CNM components because of the relatively large  $\Delta e^{-\tau(\nu)}$ , but it has several WNM components; its nearby brother, 3C208.0, is similar.

3C225a (Figure 3) and 3C225b (Figure 10) have truly complicated expected profiles, each of which extends over a wide velocity range and has several peaks connected by a broad Gaussian which is only a surrogate for reality. These sources are separated by only 6.3 arcmin so that one expects them to be similar, and they are. However, their Gaussian representations differ significantly, partly because 3C225b has CNM components at velocities where 3C225a has WNM ones; this is, in turn, a consequence of the fact that 3C225a has large errors in its opacity spectrum (Figure 3). Also, the fitting process yields quite different estimates for the WNM components in the velocity range  $-15$  to  $10 \text{ km s}^{-1}$ , largely because the contribution to the expected profiles of the broad weak CNM component in this range is poorly determined, particularly for 3C225a. Inconsistencies between the fits to this pair of sources illustrate the uncertainties introduced by large angular derivatives. Fortunately, our observing and analysis techniques reveal these derivatives and the errors they introduce. Because the optical depth error profile for 3C225b is about a factor of two smaller than that for 3C225a, the WNM and CNM components to 3C225b should be more reliable.

Heiles (2001b) presented a short preliminary report of this work which featured 3C18 (Figure 11) as an example of a straightforward fit. Ironically, further reflection reveals that it is not so straightforward, despite the fact that its profiles look so simple; in fact, 3C18 is probably the most



difficult case in our entire source list with regard to the ambiguity in assigning CNM and WNM components. To illustrate this ambiguity for such a difficult case we discuss the alternative fit in the following paragraph.

In the current fit for 3C18 we have replaced the earlier narrow WNM component, which had  $T_{kmax} = 2200$  K, with a CNM component that is 30% wider with  $T_{kmax} = 3640$  K and  $T_s = 586 \pm 11$  K. With the earlier fit, the residual of the opacity profile fit (i.e., the difference between the observed and fitted opacity profiles) had the same shape as the original narrow WNM component and was somewhat larger in magnitude than the  $\Delta\tau(\nu)$  profile. Accordingly, we could assign the residual to a new CNM component. At the same time, we eliminated a doubtful narrow CNM component in the original fit. The original and new fits are of comparable quality. This illustrates the effects of subjective judgment on measured spectra whose fitted residuals lie close to the intrinsic errors. We emphasize that we do not necessarily regard the current fit as better than the earlier one; rather, we present this difficult case as an illustration. Accordingly, the spin temperature of this CNM component should be regarded with suspicion. However, if its spin temperature is close to the derived value of  $267 \pm 5$  K, then this source is very unusual in having insignificant WNM. Our opinion is that the spin temperature has little validity, because all other sources have significant WNM column density fractions. This change doesn't affect any other parameters much, nor does it affect the conclusion in Paper II that  $T_{kmax}$  for this component lies in the thermally unstable range.

The fitting of Gaussians to some sources seems strained. 3C79 (Figure 12) is one example with a bumpy opacity profile and a nearly triangular expected profile. We fit it successfully with 5 CNM components, which seems excessive for a source at Galactic latitude  $b = -35^\circ$ , and a single WNM component.

#### 4.6.3. Sources with no CNM components

19 sources exhibit no detectable opacity profile; we fit them only with WNM components. Most of these fits are straightforward, requiring one or two rather clearly-defined components. Some are more complicated. 3C263.1 (Figure 13) has three narrower WNM components embedded in a much broader one; the need for the three is clear, but the broad one might be an unreal way to represent more blended components. P0820+22 (Figure 15) is similar, but it also contains one or two WNM components that are considerably narrower, with widths comparable to typical CNM components. 4C19.44 (Figure 14) has three narrow blended WNM components; again, their widths are similar to those of typical CNM components, but the errors in the opacity spectrum prevent them from being detected.

#### 4.7. Two illustrative examples of the combined Gaussian fitting process

Here we discuss the fits for two particular sources in some detail to illustrate our Gaussian-fitting process. We choose 3C120 and 3C315 because they are typical in most respects, but are unusual in the following way. For most sources the variances do not change much for different trials of  $\mathcal{F}_k$ ; the ratios of maximum to minimum variance are usually less than 1.2. However, some sources have significantly larger ratios, and these two sources have the largest, 3.1 and 2.9 respectively. The next highest is 4C19.44 (ratio=1.8).

First a comment on sources that have atypical ratios that exceed 1.4: 3C120, 3C138, 3C315, 3C318, 3C353, 3C93.1, 4C19.44, NRAO140. Some sources are so extreme that their fits don't even converge for some trials; this happened for 3C123, 3C138, 3C172.0, 3C315, NRAO140. For most of these sources, the fits that do converge produce variances that don't differ much.

We display the two extreme fits for 3C120 and 3C315 in plots with three panels in Figures 16 and 17. In the top two panels of these figures we plot the observed expected profile  $T_{exp}(\nu)$  and the two extreme fits. For both sources the residuals are smaller when the principal WNM component has  $\mathcal{F} = 0$ , i.e. it lies fully behind the absorbing CNM components. The absorption of the broad WNM component by the narrower CNM ones puts more structure on the central peak of the profile.

##### 4.7.1. 3C120

Figure 16 exhibits the results for 3C120. Note the factors of two and four expansion in vertical scale for the residuals and uncertainties on the top two and bottom panels, respectively. First, some general comments about the choice of Gaussian components. The opacity spectrum in the bottom panel is fit very well by the three blended CNM components, with residuals smaller than the errors; fitting only two CNM Gaussians makes the residuals unacceptably large. The emission spectrum is fit by three WNM Gaussians, one of which is weak and centered at  $-19 \text{ km s}^{-1}$ , outside the  $V_{LSR}$  plotting range. The other two WNM components are blended: one is wide and weak, providing a floor over which the narrower, more intense WNM Gaussian sits.

The residuals and uncertainties are expanded by a factor of two on the top two panels. The differing residuals are obvious. The residuals are affected almost exclusively by  $\mathcal{F}$ ; the ordering of CNM components affects the variance only at the  $\sim 2\%$  level, despite the large CNM central optical depths (1.67, 0.74, 0.63). The relative insensitivity of the residuals to CNM ordering is typical.

The intense, narrow WNM Gaussian has halfwidth  $6.75 \pm 0.78 \text{ km s}^{-1}$ , corresponding to  $T_{kmax} = 1000 \text{ K}$ . From Table 2, its peak intrinsic weighted mean  $T_{0,k} = 41.3 \pm 5.6 \text{ K}$ , so that its peak opacity  $\tau_0 \geq (41/1000) = 0.041$ . From the errors on  $\tau(\nu)$  in the bottom panel, we estimate that a component that has its width and center should not have  $\tau_0 \gtrsim 0.02$ . This is smaller than the 0.041 that we just calculated. Since  $T_k$  smaller than 1000 K would produce an even larger peak opacity, the true  $T_k$  cannot be far below 1000 K; moreover, we could probably include this

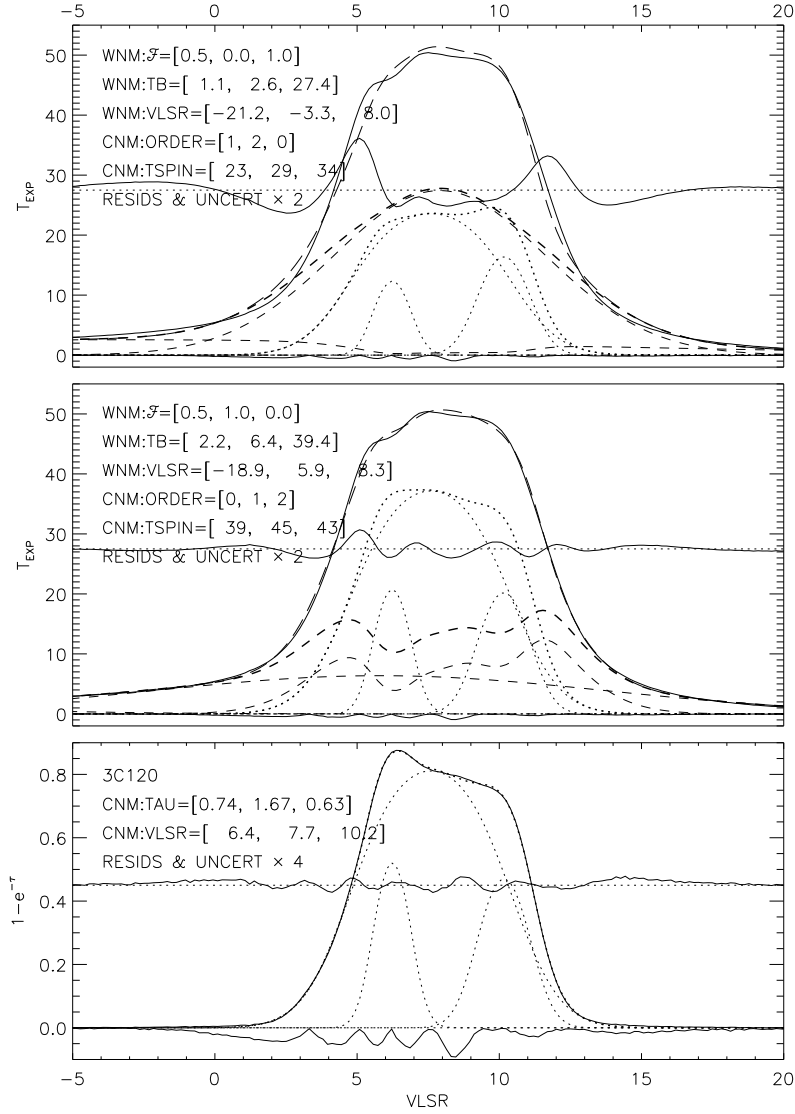


Fig. 16.— Data for 3C120. Top two panels: data and fits having largest (top) and smallest residuals for the trial fits to  $T_{exp}(\nu)$ . Bottom panel: data and fits for the opacity spectrum. For a more detailed description of this figure, see §4.7. Here, the top two panels are similar to the top panel in Figure 3, and the bottom panel is like the bottom panel in that figure.

component in the opacity fit, which would slightly reduce the  $\tau_0$  for the other components (and there would be significant uncertainties).

#### 4.7.2. 3C315

Figure 17 exhibits the results for 3C315. The opacity spectrum is fit to within the uncertainties by two CNM Gaussians that overlap only slightly. The emission spectrum is very well fit by two WNM Gaussians with nearly equal central velocities; one is wide and weak and provides a floor over which the narrower, more intense WNM Gaussian sits. The residuals and uncertainties are expanded by a factor of four on the top two panels. The differing residuals are obvious. As for 3C120, the residuals are affected almost exclusively by  $\mathcal{F}$ , here because of the small overlap of the two CNM components.

The intense, narrow WNM Gaussian has halfwidth  $6.6 \pm 1.2 \text{ km s}^{-1}$ , corresponding to  $T_{kmax} < 950 \text{ K}$ . From Table 2, its peak intrinsic weighted mean  $T_{0,k} = 12.5 \pm 0.4 \text{ K}$ , so that its peak opacity  $\tau_0 \geq (12.5/950) = 0.013$ . This is somewhat smaller than the  $\sim 0.02$  that one visually estimates from the bottom panel for the upper limit for its opacity, so the results are mutually consistent and its true temperature can be (but is not necessarily) somewhat below 950 K, say  $\sim 600 \text{ K}$ .

#### 4.7.3. Commentary

Table 3 illustrates how the CNM spin temperatures  $T_s$  and the WNM intrinsic peak brightness temperatures  $T_0$  change from the worst and best fits, and also lists the fit adopted in our standard Table 2; these values are in the three pairs of columns. We don’t show the changes in  $V_{LSR}$  or linewidth because they are small. The adopted values from Table 2 are all closer to the best case values than the worst case ones, and the uncertainties on the adopted values look reasonable given the scatter of the worst/best values.

Our main results in Table 2 are not those from the particular  $\mathcal{F}_k$  that yields the smallest variance. The reason is that each derived variance is a result of an independent numerical experiment and model fit. The results of each experiment should be regarded as a set of independent estimates for the HI component parameters. As with any set of independent measurements, the best estimate for the derived parameters is an appropriately weighted average of their independent estimates. We perform this weighting as described in §3.5.

The WNM Gaussian centers and widths (and, to a lesser extent the intensities) are not strongly affected by the choice of  $\mathcal{F}$ . This is easy to understand. We can mentally divide the expected profile into two portions, the “center” where the CNM absorption exists and the “outside” where it does not.

Consider 3C120 above in Figure 16. In both upper panels, the WNM Gaussian parameters are

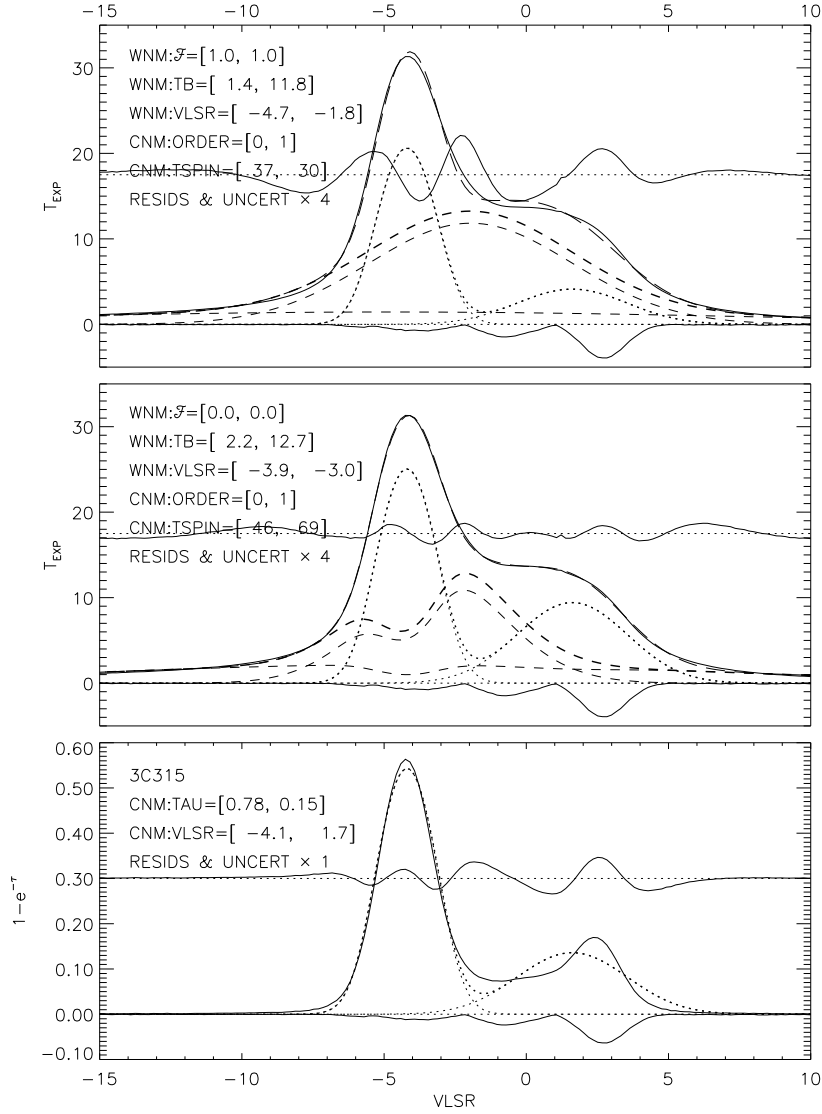


Fig. 17.— Data for 3C315. Top two panels: data and fits having largest (top) and smallest residuals for the trial fits to  $T_{exp}(\nu)$ . Bottom panel: data and fits for the opacity spectrum. For a more detailed description of this figure, see §4.7. Here, the top two panels are similar to the top panel in Figure 3, and the bottom panel is like the bottom panel in that figure.

determined mainly by the outside portions: after all, it is to represent these outside portions that the WNM component is required. The opacity has no effect on these outside portions; this is why the WNM Gaussian properties don’t change much between the two panels.

In contrast, the central portion of the expected profile is highly affected by  $\mathcal{F}$ . The central portion, both for 3C120 and 3C137, has narrow structure, and this structure can only come from the narrower opacity components. For these two sources, this narrower structure is best represented by allowing the CNM components to absorb the WNM emission from behind. This choice, with WNM behind, means that the WNM contributes less to the emission and the CNM spin temperatures must be larger to compensate.

## 5. COMPARISON OF GAUSSIAN-FIT RESULTS WITH SLOPE METHOD

Here we compare the two methods, both of which provide spin temperatures using physically correct radiative transfer. For each method we provide two measurements of spin temperature for the two extreme values of  $\mathcal{F}$ . For  $\mathcal{F} = 0$  we designate the slope-derived spin temperatures by the symbols  $T_{s,S,\mathcal{F}=0}$  and the Gaussian-derived ones with  $T_{s,G,\mathcal{F}=0}$ , with equivalent designations for  $\mathcal{F} = 1$ .

To obtain spin temperatures with the slope method (§3.2), one makes a “slope plot” by plotting  $T_{exp}(\nu)$  versus  $(1 - e^{-\tau(\nu)})$  and visually estimates the slope and the intercept. The intercept is  $T_{E,WNM}$ . For  $\mathcal{F} = 1$  the slope is  $T_s$ ; for  $\mathcal{F} = 0$  the slope is  $T_s - T_{E,WNM}$  (equation 17). Our technique of Gaussian fitting also provides  $T_s$  and  $T_{E,WNM}$ .

Before beginning, we note that our least-square fits produce reasonable facsimiles of the observed  $T_{exp}(\nu)$  and  $e^{-\tau(\nu)}$  profiles. Thus, the slope plot of the observed  $T_{exp}(\nu)$  versus  $e^{-\tau(\nu)}$  is very similar to that of the predicted one, and both provide similar estimates of  $T_{s,S}$ .

Nevertheless, because of the nonuniqueness of Gaussians it is conceivable that the model embodied in our least squares fit bears no relationship to the real situation for a particular source. Even so, our fit is a numerical expression of *some* physical situation that happens to match the observed data, and our Gaussian parameters are necessarily correct for this (perhaps fictitious) situation. Therefore, if the slope method disagrees with the Gaussian parameters for this situation, the slope method is necessarily incorrect for this possibly fictitious situation. In fact, however, we believe that our Gaussian fits are usually reasonably good approximations to the real situations and a disagreement between  $T_{s,S}$  and  $T_{s,G}$  indicates a problem with the slope method.

### 5.1. Two representative examples

We compare the results derived from the slope method and our Gaussian fits for two representative example sources, one with unblended opacity components and one with blended components.

We show the results in three-panel plots (Figures 18 and 19) in which the top two panels are the usual ones described in §2.8. The bottom panel shows the slope plot of  $T_{exp}(\nu)$  versus  $\tau(\nu)$ ; the solid line is the data and the dashed line the least-squares fit. The heavy dashed lines show the visually-estimated slopes. In the upper left of each bottom panel are the ranges of  $T_s$  allowed by the slopes and intercepts.

### 5.1.1. *Unblended opacity components*

Figure 18 exhibits the data for 3C207. There is a pair of well-separated, relatively unblended CNM components, with two associated strong WNM components that are slightly blended and a third weak, narrow WNM component ( $T_K < 100$  K) which is embedded in the stronger WNM component. Our CNM components have  $T_s = (18 \pm 3, 18 \pm 5)$  K. Each opacity component produces a well-defined lobe on the slope plot; the slopes imply  $\sim 17$  and 23 K if  $F = 1$ , which is in satisfactory agreement with our CNM components. This result is typical: in all cases with unblended CNM opacity components the slope method works well, even with blended WNM components.

### 5.1.2. *Blended multicomponent opacity profiles*

Figure 19 exhibits the data for P0531+19. The opacity profile has three CNM components, two narrow ones with  $T_s = (40 \pm 2, 110 \pm 3)$  K for the strong and weak, respectively, connected by a broad one with  $T_s = (171 \pm 5)$  K. The emission profile consists of these plus a single broad WNM component. The two narrow CNM components produce well-defined lobes on the slope plot with slopes of  $\sim (8, 18)$  K for the strong and weak one, respectively. The broad CNM component overlaps both of the narrow components; it contributes less opacity but as much or more emission than the narrow components. It does not produce a well-defined lobe, so that at the velocity of each lobe on the slope plot both a narrow and the wide component contribute. Thus each slope-derived spin temperature is in some sense applicable to both its narrow and wide component.

The slope-derived temperatures are much colder than the Gaussian-derived ones. Thus, the slope method doesn't work at all for blended components. It fails because the emission of a CNM component is not proportional only to its opacity, but rather to the product of opacity with spin temperature. In this example, the spin temperature of the broad opacity component is more than four times higher than that of the stronger narrow component, so the broad component dominates the emission while the narrow one dominates the opacity. The emission of the broad component doesn't change much over the narrow ones width, so the slope is small.

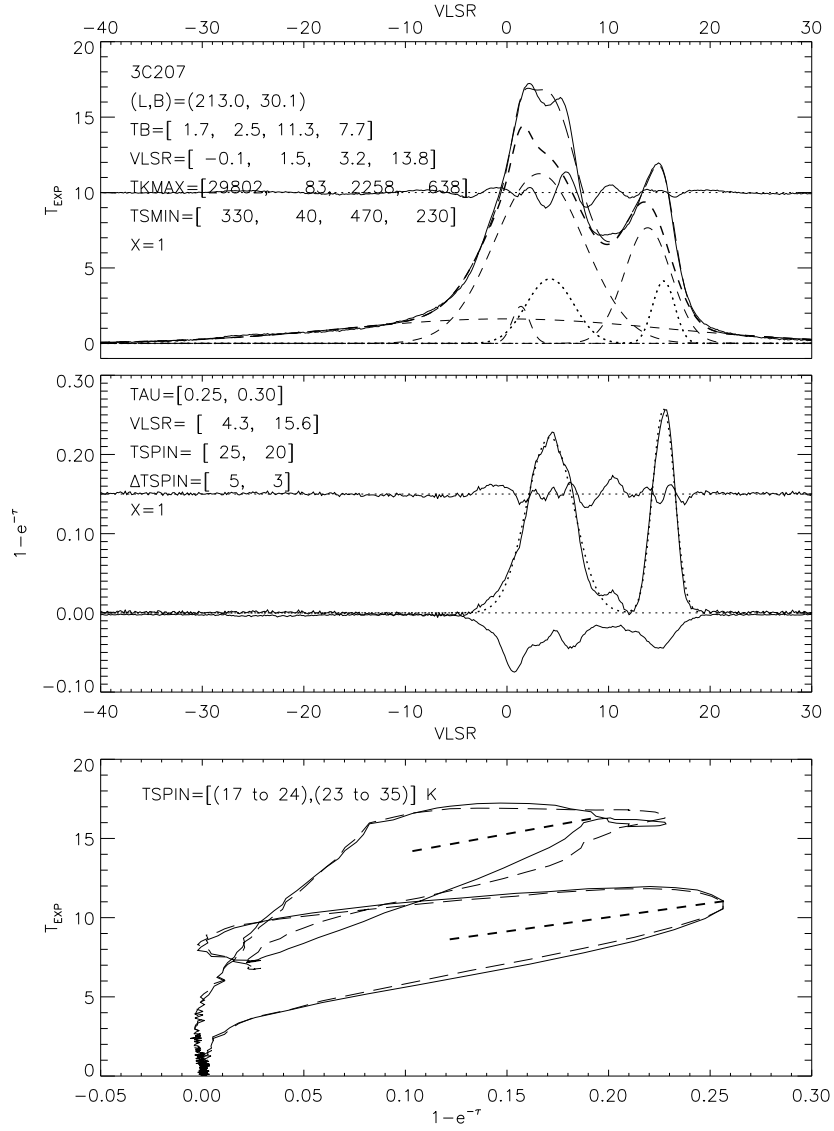


Fig. 18.— For 3C207, comparison of Gaussian-derived and slope-derived spin temperatures for  $\mathcal{F} = (0, 1)$ . The top two panels are the same as the two-panel plots such as Figure 3. The bottom panel is the slope plot  $T_{exp}(\nu)$  versus  $[1 - e^{-\tau(\nu)}]$  discussed in §5.



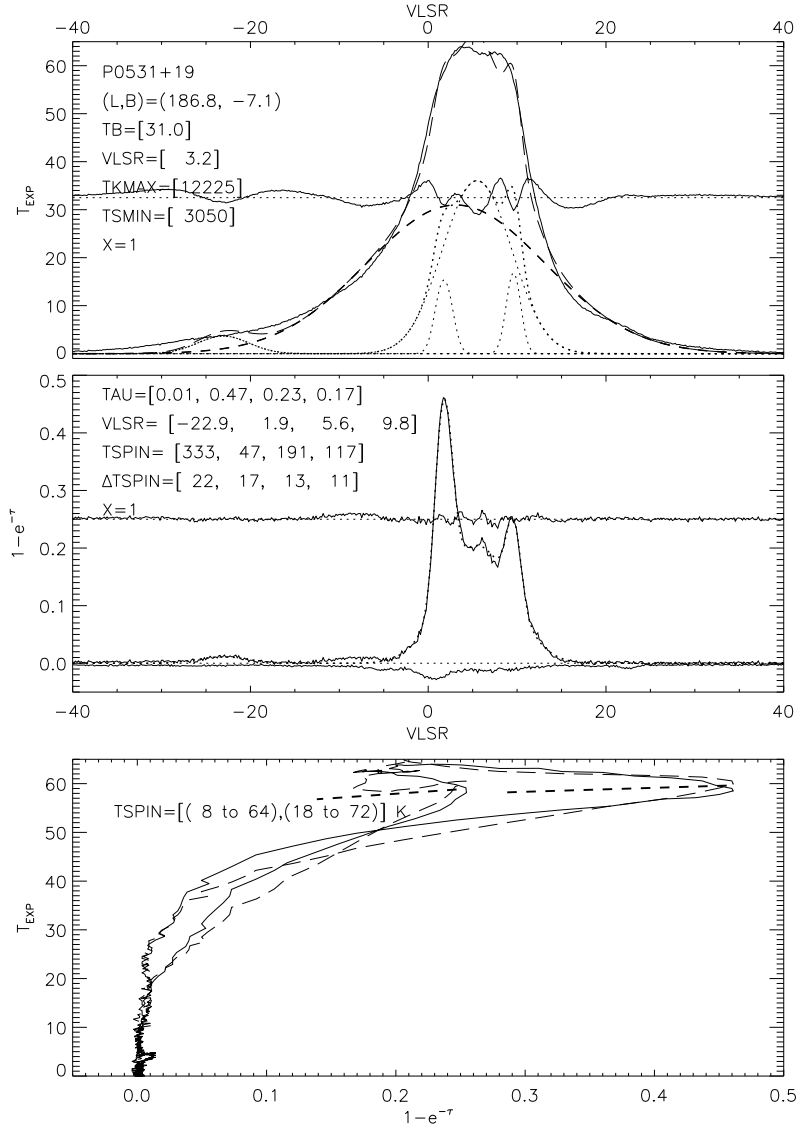


Fig. 19.— For P0531+19, comparison of Gaussian-derived and slope-derived spin temperatures for  $\mathcal{F} = (0, 1)$ . The top two panels are the same as the two-panel plots such as Figure 3. The bottom panel is the slope plot  $T_{exp}(\nu)$  versus  $[1 - e^{-\tau(\nu)}]$  discussed in §5.

## 5.2. Sample of ten sources and conclusion

Table 4 summarizes spin temperatures  $T_{s,S}$  and  $T_{s,G}$  for a set of ten representative sources. The first four sources have no overlapping CNM components. The last six have overlapping components, with one or more Gaussians contributing significantly to the opacity at the velocity of each lobe in the slope plot; the multiple values of  $T_{s,G}$  for these components are listed in square brackets. The table lists temperatures for both  $\mathcal{F} = (0, 1)$ .

Sources like 3C207 with no overlapping components produce good agreement between  $T_{s,G}$  and  $T_{s,S}$ . But the agreement for sources with overlapping components, like P0531+19, is abysmal.

We conclude that the slope method works well when the opacity profile is simple. However, with multiple components it does not work well. We will proceed using our Gaussian fit results.

## 6. SUMMARY

This paper discusses the observation and reduction techniques of our large survey of the 21-cm line in emission and absorption. We use Gaussian components and a simple but physically correct model to treat the radiative transfer issues. The major topics are as follows.

1. §2 presents the theory of extracting the opacity and expected profiles from the on- and off-source spectra. We apply this theory to the Arecibo data, which are characterized by several effects common to most telescopes but amplified at Arecibo because of its large sidelobes. The most serious instrumental effect is the impossibility of getting a true off-source spectrum; we develop an observing and reduction technique that not only solves this problem but also provides reliable estimates of uncertainty for the derived opacity and expected profiles. Our results compare well with older data that are correct, but some older data are incorrect. Surprisingly, stray radiation has little influence on Arecibo’s emission profiles (§4.2).
2. §3 discusses the radiative transfer of the 21-cm line for the real case in which some of the gas is Warm Neutral Medium (WNM) and some the Cold Neutral Medium (CNM). We present a simple, physically correct model for this radiative transfer for which we decompose the observed profiles into Gaussian components; the CNM components are ordered along the line of sight so that some absorb the emission of others, and the ensemble of CNM clouds is placed an arbitrary fractional distance along the line of sight through the WNM.

Because of our inclusion of radiative transfer, we derive spin temperatures that are much lower than those from previous work. Our temperatures are comparable to those derived for the Magellanic clouds using the “slope method”. The slope method is another simple, physically correct model for the radiative transfer and works well for simple profiles, but not multicomponent opacity profiles (§5).

3. Fitting Gaussians to spectra is a subjective and nonunique process. §4 devotes considerable

discussion to our method and process, with many illustrative examples to clarify our subjective biases. For the opacity spectra, we generally fit the minimum number of Gaussians required to reproduce them to within the uncertainties, and for many sources the number of blended Gaussians is small. For the expected emission profiles we fit a “reasonable” number of additional WNM components (§4.2). We discuss the effect of fitting either too few or too many Gaussians to a line profile and conclude that the derived spin temperatures are not very much affected.

Some optical observers fit many Gaussians to reproduce line shapes exactly. We argue that this procedure is not necessarily correct because lines are always nonthermally broadened, in which case lines are not necessarily Gaussians.

4. Paper II provides a detailed discussion of the WNM and CNM properties, together with other astrophysical implications.

We acknowledge helpful discussions with Robert Braun, John Dickey, Ed Jenkins, Dan Welty, and an unknown referee with an eagle eye. This work was supported in part by NSF grants AST-9530590, AST-0097417, and AST-9988341; and by the NAIC.

## REFERENCES

- Crutcher, R.M., Troland, T.H., & Heiles, C. 1981, *ApJ*, 249, 134.
- Dickey, J.M., Salpeter, E.E., & Terzian, Y. 1978, *ApJS*, 36, 77 (DST).
- Dickey, J.M., Mebold, U., Stanimirovic, S., & Staveley-Smith, L. 2000, *ApJ*, 536, 756.
- Hartmann, D., & Burton, W.B. 1997, *Atlas of Galactic Neutral Hydrogen*, Cambridge U. Press.
- Heiles, C. 2001a, *ApJ*, 551, L105.
- Heiles, C. 2001b, *PASP*, 113, 1243.
- Heiles, C. et al 2001a, *PASP*, 113, 1247.
- Heiles, C. et al 2001b, *PASP*, 113, 1274.
- Heiles, C. & Troland, T. 2002, *apj*, 000, 000 (Paper II).
- Greisen, E.W. and Liszt, H.S. 1986, *ApJ*, 303, 702.
- Jenkins, E.B. & Tripp, T.M. 2001, *ApJS*, 137, 297.
- Mebold, U., Düsterberg, C., Dickey, J.M., Staveley-Smith, L., & Kalberla, P. 1997, *ApJ*, 490, L65.
- Payne, H. E., Salpeter, E.E., & Terzian, Y. 1982, *ApJS*, 48, 199 (PST).
- Press, W.H., Flannery, B.P., Teukolsky, S.A., & Vetterling, W.T. 1986, *Numerical Recipes* (second edition), Cambridge University Press.

Welty, D.E. & Hobbs, L.M. 2001, ApJS, 133, 345.

---

This preprint was prepared with the AAS L<sup>A</sup>T<sub>E</sub>X macros v5.0.

Table 1. Derived spectra for all sources

---

---

This table is available only on-line as a machine-readable table

---

FTP to `vermi.berkeley.edu` as anonymous and `cd pub/zobs; get tab1.txt`  
This table should also be available on the electronic edition of Ap.J.

---

Table 2. Table of Gaussian Fit Parameters

$T_B$	$\tau$	$V_{LSR}$	$\Delta V$	$T_s$	$T_{kmax}$	$N(HI)_{20}$	$\mathcal{F}$ or O	(l/b/SOURCE)
0.72 ± 0.04	0.004	-12.6 ± 1.0	53.58 ± 2.70	180	62746	0.75	0.50 ± 0.29	118.6/-52.7/3C18
16.71	0.669 ± 0.011	-8.9 ± 0.0	2.43 ± 0.03	34.25 ± 7.89	129	1.09	1	118.6/-52.7/3C18
19.80	0.077 ± 0.019	-6.7 ± 0.2	8.62 ± 0.70	267.80 ± 5.28	1625	3.46	0	118.6/-52.7/3C18
8.09	0.181 ± 0.018	-5.7 ± 0.1	3.98 ± 0.25	48.75 ± 9.41	346	0.69	2	118.6/-52.7/3C18
1.67 ± 0.12	0.002	-7.1 ± 0.4	26.21 ± 1.37	830	15018	0.86	0.50 ± 0.29	129.4/-49.3/3C33-1
10.41	0.034 ± 0.001	-4.6 ± 0.1	9.44 ± 0.30	309.63 ± 4.79	1949	1.95	0	129.4/-49.3/3C33-1
2.35 ± 0.19	0.011	-7.2 ± 0.5	22.25 ± 1.15	210	10822	1.02	0.50 ± 0.29	129.5/-49.3/3C33-2
10.20	0.059 ± 0.002	-4.2 ± 0.2	9.31 ± 0.42	177.85 ± 4.54	1892	1.90	0	129.5/-49.3/3C33-2
0.38 ± 0.02	0.003	-42.9 ± 0.7	22.23 ± 1.79	150	10804	0.16	0.50 ± 0.29	129.4/-49.3/3C33
2.23 ± 0.06	0.006	-6.7 ± 0.1	22.46 ± 0.43	400	11030	0.98	0.50 ± 0.29	129.4/-49.3/3C33
9.35	0.025 ± 0.000	-4.3 ± 0.0	8.91 ± 0.10	379.10 ± 3.26	1733	1.64	0	129.4/-49.3/3C33
22.55	0.290 ± 0.007	-10.8 ± 0.1	5.10 ± 0.13	89.70 ± 4.14	569	2.58	0	157.8/-48.2/3C64
10.70 ± 0.18	0.012	-5.6 ± 0.2	16.43 ± 0.24	890	5901	3.42	0.53 ± 0.29	157.8/-48.2/3C64
3.71	0.086 ± 0.007	0.2 ± 0.2	4.37 ± 0.38	45.23 ± 5.28	417	0.33	1	157.8/-48.2/3C64
18.08	0.729 ± 0.014	-10.4 ± 0.0	2.06 ± 0.03	34.92 ± 4.70	92	1.02	0	170.2/-44.9/3C75-1
11.48 ± 0.22	0.016	-9.3 ± 0.1	10.15 ± 0.18	720	2253	2.27	0.49 ± 0.29	170.2/-44.9/3C75-1
1.30	0.082 ± 0.007	-6.1 ± 0.1	3.01 ± 0.30	16.45 ± 5.14	198	0.08	1	170.2/-44.9/3C75-1
10.01	0.127 ± 0.006	5.0 ± 0.1	4.58 ± 0.22	84.01 ± 7.64	458	0.95	2	170.2/-44.9/3C75-1
15.94 ± 0.25	0.040	5.8 ± 0.1	11.76 ± 0.15	400	3021	3.65	0.50 ± 0.29	170.2/-44.9/3C75-1
17.24	0.647 ± 0.015	-10.4 ± 0.0	2.33 ± 0.05	36.21 ± 4.54	118	1.06	0	170.3/-44.9/3C75-2
10.74 ± 0.23	0.032	-9.6 ± 0.1	10.46 ± 0.23	340	2393	2.19	0.49 ± 0.29	170.3/-44.9/3C75-2
3.05	0.094 ± 0.009	-6.0 ± 0.1	2.34 ± 0.26	34.06 ± 4.44	119	0.15	1	170.3/-44.9/3C75-2
10.14	0.139 ± 0.007	4.9 ± 0.1	4.41 ± 0.23	78.00 ± 8.04	424	0.93	2	170.3/-44.9/3C75-2
16.98 ± 0.27	0.022	5.8 ± 0.1	11.78 ± 0.16	760	3035	3.90	0.50 ± 0.29	170.3/-44.9/3C75-2
17.93	0.682 ± 0.006	-10.4 ± 0.0	2.32 ± 0.02	36.26 ± 4.06	117	1.12	0	170.3/-44.9/3C75
9.56 ± 0.16	0.009	-10.0 ± 0.1	9.79 ± 0.18	1010	2095	1.82	0.49 ± 0.29	170.3/-44.9/3C75
3.33	0.095 ± 0.004	-5.8 ± 0.1	2.74 ± 0.12	36.89 ± 3.43	163	0.19	1	170.3/-44.9/3C75
11.02	0.113 ± 0.003	5.3 ± 0.1	5.19 ± 0.13	103.57 ± 6.97	589	1.18	2	170.3/-44.9/3C75
14.09 ± 0.21	0.010	5.7 ± 0.0	13.05 ± 0.15	1400	3720	3.58	0.50 ± 0.29	170.3/-44.9/3C75
11.41	0.023 ± 0.002	-8.7 ± 0.2	12.03 ± 0.63	508.07 ± 3.80	3164	2.70	3	174.9/-44.5/3C78
6.81	0.116 ± 0.002	-7.7 ± 0.0	3.07 ± 0.06	62.07 ± 5.14	206	0.43	1	174.9/-44.5/3C78
6.81	0.153 ± 0.002	4.2 ± 0.0	1.92 ± 0.05	47.89 ± 4.61	80	0.27	0	174.9/-44.5/3C78
28.24	1.108 ± 0.004	6.8 ± 0.0	2.24 ± 0.01	42.17 ± 7.17	109	2.04	2	174.9/-44.5/3C78
19.04 ± 0.47	0.011	8.1 ± 0.0	11.47 ± 0.13	1730	2873	4.25	0.44 ± 0.29	174.9/-44.5/3C78
4.29	0.082 ± 0.001	10.7 ± 0.1	4.26 ± 0.14	54.38 ± 6.31	396	0.37	4	174.9/-44.5/3C78
2.50	0.342 ± 0.006	-6.4 ± 0.0	2.06 ± 0.04	8.64 ± 4.69	92	0.12	0	164.1/-34.5/3C79
1.55	0.082 ± 0.007	-3.3 ± 0.0	1.18 ± 0.12	19.55 ± 8.10	30	0.04	4	164.1/-34.5/3C79
8.08 ± 2.21	0.011	-3.0 ± 1.6	15.40 ± 1.07	730	5182	2.46	0.50 ± 0.29	164.1/-34.5/3C79
6.93	0.139 ± 0.005	1.4 ± 0.0	2.85 ± 0.14	53.25 ± 8.33	177	0.41	1	164.1/-34.5/3C79
21.34	0.148 ± 0.004	2.2 ± 0.2	14.09 ± 0.27	155.61 ± 18.25	4339	6.30	2	164.1/-34.5/3C79
1.76	0.048 ± 0.006	9.8 ± 0.1	1.14 ± 0.17	37.78 ± 6.82	28	0.04	3	164.1/-34.5/3C79
1.72 ± 0.17	0.000	-19.5 ± 0.3	6.08 ± 0.76	5170	808	0.20	0.50 ± 0.29	160.0/-15.9/3C93.1
4.26 ± 0.09	0.010	-13.1 ± 0.6	43.14 ± 1.07	410	40687	3.58	0.50 ± 0.29	160.0/-15.9/3C93.1
19.91	0.860 ± 0.080	6.5 ± 0.2	2.99 ± 0.24	34.50 ± 12.95	195	1.73	1	160.0/-15.9/3C93.1
32.88 ± 1.75	0.044	7.2 ± 0.0	7.88 ± 0.26	740	1357	5.04	0.38 ± 0.28	160.0/-15.9/3C93.1
20.40	1.243 ± 0.117	8.8 ± 0.1	2.54 ± 0.13	28.67 ± 11.27	141	1.77	0	160.0/-15.9/3C93.1
1.65	0.081 ± 0.004	-1.2 ± 0.1	3.23 ± 0.18	21.28 ± 6.32	228	0.11	3	179.9/-31.1/3C98-1
16.65 ± 0.31	0.022	6.0 ± 0.1	13.51 ± 0.23	770	3992	4.38	0.57 ± 0.29	179.9/-31.1/3C98-1
7.78	0.209 ± 0.011	9.4 ± 0.0	1.47 ± 0.09	41.24 ± 16.54	47	0.25	0	179.9/-31.1/3C98-1

Table 2—Continued

$T_B$	$\tau$	$V_{LSR}$	$\Delta V$	$T_s$	$T_{kmax}$	$N(HI)_{20}$	$\mathcal{F}$ or O	( $l/b$ /SOURCE)
35.37	$0.368 \pm 0.008$	$9.7 \pm 0.0$	$6.07 \pm 0.08$	$114.85 \pm 5.80$	804	5.00	1	179.9/–31.1/3C98-1
5.94	$0.028 \pm 0.003$	$22.8 \pm 0.3$	$5.40 \pm 0.65$	$215.87 \pm 6.91$	638	0.63	2	179.9/–31.1/3C98-1
5.05	$0.090 \pm 0.004$	$-1.5 \pm 0.1$	$3.16 \pm 0.14$	$58.82 \pm 5.99$	218	0.33	3	179.8/–31.0/3C98-2
20.18 $\pm$ 0.36	0.011	$7.3 \pm 0.1$	$13.21 \pm 0.21$	1860	3813	5.19	$0.53 \pm 0.29$	179.8/–31.0/3C98-2
4.47	$0.203 \pm 0.013$	$9.5 \pm 0.0$	$1.39 \pm 0.10$	$24.40 \pm 15.72$	41	0.13	0	179.8/–31.0/3C98-2
36.44	$0.452 \pm 0.011$	$9.6 \pm 0.0$	$4.62 \pm 0.06$	$100.23 \pm 8.51$	466	4.08	1	179.8/–31.0/3C98-2
5.74	$0.035 \pm 0.003$	$22.5 \pm 0.2$	$4.56 \pm 0.42$	$165.93 \pm 6.56$	453	0.52	2	179.8/–31.0/3C98-2
1.48	$0.092 \pm 0.004$	$-1.0 \pm 0.1$	$4.87 \pm 0.22$	$16.82 \pm 5.14$	519	0.15	3	179.8/–31.0/3C98
17.00 $\pm$ 0.23	0.021	$6.3 \pm 0.1$	$14.86 \pm 0.21$	800	4824	4.92	$0.53 \pm 0.29$	179.8/–31.0/3C98
7.09	$0.297 \pm 0.017$	$9.5 \pm 0.0$	$1.35 \pm 0.09$	$27.59 \pm 20.46$	39	0.21	1	179.8/–31.0/3C98
38.72	$0.508 \pm 0.012$	$9.5 \pm 0.0$	$5.21 \pm 0.07$	$97.27 \pm 6.30$	594	5.02	0	179.8/–31.0/3C98
5.33	$0.041 \pm 0.003$	$23.0 \pm 0.2$	$6.82 \pm 0.58$	$134.11 \pm 3.95$	1016	0.72	2	179.8/–31.0/3C98
4.54	$0.057 \pm 0.004$	$-2.0 \pm 0.2$	$4.37 \pm 0.44$	$81.35 \pm 5.69$	416	0.40	3	187.6/–33.6/3C105
6.85 $\pm$ 0.40	0.019	$6.5 \pm 0.2$	$24.41 \pm 0.69$	370	13021	3.26	$0.49 \pm 0.29$	187.6/–33.6/3C105
25.63	$2.103 \pm 0.054$	$8.3 \pm 0.0$	$1.81 \pm 0.04$	$29.20 \pm 11.94$	71	2.17	2	187.6/–33.6/3C105
24.86	$0.169 \pm 0.012$	$8.4 \pm 0.1$	$9.47 \pm 0.44$	$159.93 \pm 4.41$	1960	4.98	1	187.6/–33.6/3C105
33.06	$2.883 \pm 0.075$	$10.5 \pm 0.0$	$1.97 \pm 0.04$	$35.02 \pm 9.58$	84	3.87	0	187.6/–33.6/3C105
10.31 $\pm$ 1.04	0.041	$0.8 \pm 0.2$	$4.53 \pm 0.53$	250	448	0.91	$0.50 \pm 0.29$	181.8/–27.8/3C109
8.52 $\pm$ 1.05	0.003	$2.4 \pm 0.6$	$26.59 \pm 1.78$	3020	15456	4.40	$0.49 \pm 0.29$	181.8/–27.8/3C109
22.33	$0.381 \pm 0.040$	$5.0 \pm 0.2$	$3.48 \pm 0.26$	$70.49 \pm 4.42$	265	1.82	1	181.8/–27.8/3C109
62.73	$1.979 \pm 0.037$	$9.3 \pm 0.1$	$4.35 \pm 0.18$	$72.79 \pm 2.64$	412	12.19	0	181.8/–27.8/3C109
27.80	$0.344 \pm 0.028$	$13.5 \pm 0.1$	$2.35 \pm 0.16$	$95.41 \pm 3.47$	120	1.50	2	181.8/–27.8/3C109
2.15 $\pm$ 0.28	0.007	$-19.1 \pm 1.1$	$17.07 \pm 2.91$	290	6371	0.73	$0.50 \pm 0.29$	190.4/–27.4/3C120
5.99 $\pm$ 1.35	0.001	$5.2 \pm 2.2$	$20.35 \pm 4.53$	4130	9050	2.27	$0.50 \pm 0.29$	190.4/–27.4/3C120
19.32	$0.736 \pm 0.010$	$6.2 \pm 0.0$	$1.33 \pm 0.02$	$37.08 \pm 6.86$	38	0.71	0	190.4/–27.4/3C120
34.34	$1.666 \pm 0.007$	$7.6 \pm 0.0$	$4.48 \pm 0.01$	$42.34 \pm 9.96$	438	6.15	1	190.4/–27.4/3C120
41.30 $\pm$ 5.57	0.103	$8.1 \pm 0.1$	$6.34 \pm 0.73$	400	877	5.04	$0.18 \pm 0.23$	190.4/–27.4/3C120
20.65	$0.634 \pm 0.008$	$10.2 \pm 0.0$	$1.91 \pm 0.02$	$43.96 \pm 3.95$	79	1.04	2	190.4/–27.4/3C120
0.57	$0.032 \pm 0.002$	$-72.9 \pm 0.1$	$4.28 \pm 0.24$	$17.79 \pm 10.26$	400	0.05	4	170.6/–11.7/3C123
3.82 $\pm$ 0.18	0.003	$-60.7 \pm 0.5$	$25.36 \pm 1.27$	1270	14054	1.89	$0.50 \pm 0.29$	170.6/–11.7/3C123
0.18	$0.008 \pm 0.001$	$-57.8 \pm 0.5$	$5.62 \pm 1.09$	$22.15 \pm 40.62$	691	0.02	3	170.6/–11.7/3C123
2.51	$0.063 \pm 0.002$	$-19.6 \pm 0.0$	$3.14 \pm 0.11$	$40.93 \pm 6.20$	215	0.16	2	170.6/–11.7/3C123
10.11 $\pm$ 0.18	0.002	$-7.2 \pm 0.3$	$37.54 \pm 0.53$	5170	30812	7.40	$0.49 \pm 0.29$	170.6/–11.7/3C123
13.50	$1.606 \pm 0.026$	$4.4 \pm 0.0$	$4.79 \pm 0.02$	$16.88 \pm 7.44$	501	2.53	0	170.6/–11.7/3C123
80.96	$0.596 \pm 0.026$	$4.7 \pm 0.0$	$2.32 \pm 0.08$	$180.36 \pm 115.21$	117	4.86	1	170.6/–11.7/3C123
88.19 $\pm$ 5.96	0.304	$4.9 \pm 0.1$	$6.09 \pm 0.11$	290	811	10.47	$0.00 \pm 0.00$	170.6/–11.7/3C123
0.00	$0.007 \pm 0.002$	$20.0 \pm 0.5$	$3.88 \pm 1.09$	$0.00 \pm 0.00$	328	0.00	5	170.6/–11.7/3C123
10.77 $\pm$ 0.27	0.135	$-40.1 \pm 0.1$	$5.74 \pm 0.19$	80	720	1.20	$0.50 \pm 0.29$	171.4/–7.8/3C131
9.21 $\pm$ 0.25	0.034	$-19.1 \pm 1.1$	$43.93 \pm 1.10$	270	42178	7.89	$0.49 \pm 0.29$	171.4/–7.8/3C131
21.36	$0.321 \pm 0.006$	$-2.3 \pm 0.1$	$6.95 \pm 0.21$	$77.79 \pm 5.43$	1057	3.38	1	171.4/–7.8/3C131
25.06 $\pm$ 1.64	0.040	$1.5 \pm 0.1$	$16.80 \pm 0.92$	620	6168	8.18	$0.44 \pm 0.29$	171.4/–7.8/3C131
39.30	$2.152 \pm 0.034$	$5.3 \pm 0.0$	$4.24 \pm 0.04$	$44.47 \pm 8.06$	392	7.90	0	171.4/–7.8/3C131
5.52 $\pm$ 0.15	0.005	$-16.4 \pm 1.3$	$45.87 \pm 2.18$	1100	45997	4.94	$0.50 \pm 0.29$	178.9/–12.5/3C132
9.04	$0.351 \pm 0.007$	$1.8 \pm 0.1$	$5.43 \pm 0.12$	$30.52 \pm 11.08$	643	1.13	1	178.9/–12.5/3C132
39.75 $\pm$ 0.97	0.020	$5.7 \pm 0.1$	$14.50 \pm 0.43$	2000	4595	11.22	$0.49 \pm 0.29$	178.9/–12.5/3C132
43.75	$1.542 \pm 0.028$	$8.1 \pm 0.0$	$2.42 \pm 0.03$	$55.66 \pm 14.67$	128	4.05	0	178.9/–12.5/3C132
19.68	$0.260 \pm 0.006$	$13.0 \pm 0.1$	$5.68 \pm 0.23$	$85.86 \pm 9.64$	705	2.47	2	178.9/–12.5/3C132
12.83	$0.060 \pm 0.008$	$-29.5 \pm 0.4$	$8.45 \pm 0.63$	$219.27 \pm 5.45$	1559	2.17	4	177.7/–9.9/3C133
1.16	$0.064 \pm 0.009$	$-27.6 \pm 0.2$	$2.84 \pm 0.46$	$18.79 \pm 6.96$	176	0.07	3	177.7/–9.9/3C133

Table 2—Continued

$T_B$	$\tau$	$V_{LSR}$	$\Delta V$	$T_s$	$T_{kmax}$	$N(HI)_{20}$	$\mathcal{F}$ or O	( $l/b$ /SOURCE)
9.06 ± 0.17	0.020	−14.7 ± 0.7	46.06 ± 0.82	460	46378	8.13	0.50 ± 0.29	177.7/−9.9/3C133
15.35	0.262 ± 0.006	−0.2 ± 0.2	6.17 ± 0.31	66.60 ± 11.51	831	2.10	1	177.7/−9.9/3C133
25.98	0.891 ± 0.021	3.7 ± 0.0	2.77 ± 0.06	44.04 ± 17.06	167	2.12	2	177.7/−9.9/3C133
45.62 ± 1.62	0.015	4.3 ± 0.1	12.41 ± 0.39	3000	3368	11.02	0.45 ± 0.29	177.7/−9.9/3C133
30.18	1.532 ± 0.021	8.0 ± 0.0	2.51 ± 0.02	38.50 ± 13.68	138	2.89	0	177.7/−9.9/3C133
3.78	0.038 ± 0.002	−21.5 ± 0.1	3.45 ± 0.21	101.52 ± 5.08	260	0.26	5	187.4/−11.3/3C138
5.20 ± 0.14	0.004	−8.6 ± 0.5	47.38 ± 1.27	1260	49076	4.79	0.50 ± 0.29	187.4/−11.3/3C138
11.82	0.247 ± 0.006	−0.5 ± 0.1	2.86 ± 0.12	54.03 ± 9.60	178	0.74	1	187.4/−11.3/3C138
8.48	0.176 ± 0.014	1.6 ± 0.1	1.84 ± 0.09	52.62 ± 11.03	73	0.33	3	187.4/−11.3/3C138
21.94	0.060 ± 0.004	1.8 ± 0.2	14.64 ± 0.48	379.12 ± 23.44	4683	6.44	2	187.4/−11.3/3C138
25.99	1.046 ± 0.008	6.4 ± 0.0	2.30 ± 0.02	40.07 ± 12.30	115	1.87	0	187.4/−11.3/3C138
20.17 ± 0.75	0.014	6.8 ± 0.4	11.11 ± 0.84	1470	2700	4.36	0.54 ± 0.29	187.4/−11.3/3C138
15.70	0.406 ± 0.005	9.1 ± 0.0	2.81 ± 0.06	47.02 ± 11.54	172	1.05	4	187.4/−11.3/3C138
58.36	0.260 ± 0.010	−15.9 ± 0.3	15.41 ± 0.74	255.00 ± 2.08	5191	19.89	1	174.5/−1.3/3C141.0
3.27 ± 0.41	0.015	−11.4 ± 1.8	68.55 ± 6.32	220	102731	4.37	0.75 ± 0.18	174.5/−1.3/3C141.0
113.44 ± 1.74	0.101	0.6 ± 0.0	11.17 ± 0.09	1120	2726	24.68	0.00 ± 0.00	174.5/−1.3/3C141.0
20.73	0.875 ± 0.024	1.6 ± 0.1	6.19 ± 0.14	35.55 ± 1.76	836	3.75	0	174.5/−1.3/3C141.0
9.10 ± 0.93	0.005	−10.6 ± 0.3	8.78 ± 0.66	2000	1684	1.56	0.50 ± 0.29	197.6/−14.5/3C142.1
0.90	0.101 ± 0.007	−9.2 ± 0.1	3.24 ± 0.26	9.37 ± 13.82	229	0.06	3	197.6/−14.5/3C142.1
44.11	2.362 ± 0.045	7.0 ± 0.0	3.13 ± 0.03	48.69 ± 15.55	214	7.02	0	197.6/−14.5/3C142.1
39.15 ± 1.16	0.028	8.7 ± 0.1	16.13 ± 0.41	1400	5686	12.30	0.44 ± 0.29	197.6/−14.5/3C142.1
4.22	0.203 ± 0.007	13.4 ± 0.1	4.12 ± 0.17	23.03 ± 10.75	370	0.37	1	197.6/−14.5/3C142.1
9.51	0.083 ± 0.007	22.4 ± 0.1	3.39 ± 0.32	119.08 ± 10.47	251	0.65	2	197.6/−14.5/3C142.1
11.61	0.068 ± 0.003	−23.7 ± 0.1	4.35 ± 0.22	176.60 ± 5.51	412	1.02	5	185.6/4.0/3C154
24.81	0.709 ± 0.014	−2.9 ± 0.0	4.45 ± 0.06	48.85 ± 14.40	433	3.01	3	185.6/4.0/3C154
6.05	0.292 ± 0.019	−2.1 ± 0.0	1.32 ± 0.10	23.87 ± 18.23	37	0.18	2	185.6/4.0/3C154
75.24 ± 0.85	0.041	1.4 ± 0.0	18.23 ± 0.11	1830	7267	26.72	0.76 ± 0.18	185.6/4.0/3C154
30.83	0.919 ± 0.014	1.8 ± 0.0	2.63 ± 0.07	51.28 ± 18.44	151	2.42	1	185.6/4.0/3C154
19.70	0.479 ± 0.007	5.0 ± 0.1	3.47 ± 0.10	51.78 ± 15.58	263	1.68	0	185.6/4.0/3C154
10.83	0.413 ± 0.006	10.6 ± 0.0	2.12 ± 0.03	31.98 ± 9.17	98	0.55	4	185.6/4.0/3C154
23.71 ± 0.80	0.049	7.1 ± 0.3	13.83 ± 0.41	480	4181	6.39	0.50 ± 0.29	207.3/1.2/3C167
38.17	0.252 ± 0.008	22.6 ± 0.4	21.71 ± 0.98	171.23 ± 6.90	10302	18.27	2	207.3/1.2/3C167
32.37 ± 1.26	0.202	38.3 ± 0.6	20.60 ± 0.78	160	9280	13.00	0.55 ± 0.28	207.3/1.2/3C167
50.50	0.941 ± 0.024	42.2 ± 0.1	8.01 ± 0.23	82.85 ± 12.73	1403	12.16	0	207.3/1.2/3C167
8.60	0.386 ± 0.032	49.3 ± 0.1	2.09 ± 0.19	26.87 ± 5.61	95	0.42	1	207.3/1.2/3C167
1.90 ± 0.07	0.002	−8.8 ± 0.7	65.50 ± 1.54	980	93799	2.43	0.50 ± 0.29	191.2/13.4/3C172.0
3.35	0.059 ± 0.005	1.5 ± 0.2	4.33 ± 0.46	58.86 ± 6.42	409	0.29	0	191.2/13.4/3C172.0
13.58 ± 0.13	0.014	2.5 ± 0.1	18.46 ± 0.15	1000	7453	4.88	0.50 ± 0.29	191.2/13.4/3C172.0
0.99	0.031 ± 0.004	9.4 ± 0.4	5.62 ± 1.03	32.54 ± 6.75	691	0.11	1	191.2/13.4/3C172.0
6.61 ± 0.04	0.006	2.8 ± 0.1	17.67 ± 0.20	1150	6826	2.28	0.50 ± 0.00	207.6/21.8/3C190.0
1.68 ± 0.04	0.002	23.5 ± 0.4	16.51 ± 0.80	840	5962	0.54	0.50 ± 0.00	207.6/21.8/3C190.0
2.54 ± 0.03	0.003	−3.0 ± 0.2	34.85 ± 0.29	840	26546	1.72	0.50 ± 0.29	197.9/26.4/3C192
7.54 ± 0.06	0.007	7.5 ± 0.0	12.13 ± 0.11	1150	3218	1.78	0.51 ± 0.29	197.9/26.4/3C192
5.39	0.068 ± 0.002	8.0 ± 0.1	4.30 ± 0.12	82.14 ± 3.76	403	0.47	0	197.9/26.4/3C192
1.66 ± 0.07	0.005	−0.1 ± 0.3	36.92 ± 0.80	330	29801	1.19	0.50 ± 0.29	213.0/30.1/3C207
2.51 ± 0.18	0.063	1.4 ± 0.1	1.95 ± 0.13	40	82	0.10	0.50 ± 0.29	213.0/30.1/3C207
11.29 ± 0.24	0.024	3.1 ± 0.1	10.16 ± 0.19	470	2258	2.24	0.49 ± 0.29	213.0/30.1/3C207
5.46	0.250 ± 0.002	4.2 ± 0.0	5.25 ± 0.05	24.65 ± 4.74	602	0.63	1	213.0/30.1/3C207
7.71 ± 0.10	0.034	13.8 ± 0.1	5.40 ± 0.10	230	638	0.81	0.51 ± 0.29	213.0/30.1/3C207



Table 2—Continued

$T_B$	$\tau$	$V_{LSR}$	$\Delta V$	$T_s$	$T_{kmax}$	$N(HI)_{20}$	$\mathcal{F}$ or O	(l/b/SOURCE)
5.03	$0.298 \pm 0.004$	$15.4 \pm 0.0$	$2.43 \pm 0.03$	$19.53 \pm 2.66$	129	0.28	0	213.0/30.1/3C207
$0.76 \pm 0.02$	0.010	$-25.9 \pm 0.1$	$11.30 \pm 0.33$	80	2794	0.17	$0.50 \pm 0.00$	213.7/33.2/3C208.0
$3.39 \pm 0.08$	0.031	$-4.0 \pm 0.1$	$4.34 \pm 0.12$	110	412	0.29	$0.50 \pm 0.00$	213.7/33.2/3C208.0
$2.37 \pm 0.09$	0.024	$0.3 \pm 0.1$	$3.72 \pm 0.14$	100	303	0.17	$0.50 \pm 0.00$	213.7/33.2/3C208.0
$5.13 \pm 0.10$	0.010	$0.4 \pm 0.0$	$19.32 \pm 0.18$	510	8161	1.93	$0.50 \pm 0.00$	213.7/33.2/3C208.0
$6.09 \pm 0.07$	0.068	$5.9 \pm 0.0$	$3.63 \pm 0.04$	90	287	0.43	$0.50 \pm 0.00$	213.7/33.2/3C208.0
$0.63 \pm 0.01$	0.003	$-25.4 \pm 0.3$	$17.18 \pm 0.68$	210	6455	0.21	$0.50 \pm 0.00$	213.6/33.6/3C208.1
$2.72 \pm 0.08$	0.012	$-3.4 \pm 0.0$	$3.45 \pm 0.09$	220	259	0.18	$0.50 \pm 0.00$	213.6/33.6/3C208.1
$4.42 \pm 0.12$	0.010	$1.0 \pm 0.1$	$18.85 \pm 0.25$	440	7766	1.62	$0.50 \pm 0.00$	213.6/33.6/3C208.1
$3.07 \pm 0.12$	0.010	$1.6 \pm 0.0$	$4.03 \pm 0.11$	300	354	0.24	$0.50 \pm 0.00$	213.6/33.6/3C208.1
$6.49 \pm 0.08$	0.019	$6.8 \pm 0.0$	$4.01 \pm 0.05$	350	351	0.51	$0.50 \pm 0.00$	213.6/33.6/3C208.1
$4.35 \pm 0.03$	0.031	$-37.1 \pm 0.0$	$4.22 \pm 0.04$	140	389	0.36	$0.50 \pm 0.29$	219.9/44.0/3C225a
$2.97 \pm 0.03$	0.042	$-27.1 \pm 0.0$	$7.07 \pm 0.08$	70	1091	0.41	$0.50 \pm 0.29$	219.9/44.0/3C225a
$1.14 \pm 0.02$	0.010	$-13.3 \pm 0.4$	$42.44 \pm 0.56$	110	39370	0.94	$0.50 \pm 0.29$	219.9/44.0/3C225a
$1.76 \pm 0.04$	0.010	$-4.5 \pm 0.0$	$5.13 \pm 0.14$	170	575	0.18	$0.50 \pm 0.29$	219.9/44.0/3C225a
5.39	$0.013 \pm 0.001$	$-2.6 \pm 0.3$	$12.68 \pm 0.86$	$409.39 \pm 4.02$	3513	1.34	0	219.9/44.0/3C225a
5.78	$0.313 \pm 0.003$	$4.0 \pm 0.0$	$1.32 \pm 0.01$	$21.53 \pm 1.30$	37	0.17	1	219.9/44.0/3C225a
0.53	$0.033 \pm 0.001$	$-40.6 \pm 0.1$	$2.07 \pm 0.12$	$16.64 \pm 3.05$	93	0.02	4	220.0/44.0/3C225b
2.79	$0.047 \pm 0.001$	$-37.9 \pm 0.1$	$2.52 \pm 0.11$	$61.11 \pm 1.97$	138	0.14	3	220.0/44.0/3C225b
$1.79 \pm 0.05$	0.004	$-29.7 \pm 0.2$	$20.22 \pm 0.64$	420	8938	0.70	$0.50 \pm 0.29$	220.0/44.0/3C225b
1.21	$0.027 \pm 0.001$	$-28.0 \pm 0.1$	$4.78 \pm 0.13$	$45.40 \pm 3.28$	499	0.11	2	220.0/44.0/3C225b
2.01	$0.013 \pm 0.001$	$-5.6 \pm 0.1$	$6.82 \pm 0.33$	$155.08 \pm 9.70$	1015	0.27	1	220.0/44.0/3C225b
$5.73 \pm 0.09$	0.002	$-2.8 \pm 0.1$	$15.40 \pm 0.15$	2370	5182	1.72	$0.50 \pm 0.29$	220.0/44.0/3C225b
9.17	$0.745 \pm 0.002$	$3.6 \pm 0.0$	$1.25 \pm 0.00$	$17.44 \pm 1.80$	34	0.32	0	220.0/44.0/3C225b
$0.99 \pm 0.03$	0.003	$-28.5 \pm 0.4$	$21.38 \pm 1.06$	330	9996	0.41	$0.50 \pm 0.29$	220.8/46.6/3C228.0
5.52	$0.082 \pm 0.002$	$-5.1 \pm 0.0$	$2.86 \pm 0.08$	$70.43 \pm 3.48$	179	0.32	0	220.8/46.6/3C228.0
$6.40 \pm 0.07$	0.009	$-3.9 \pm 0.1$	$14.68 \pm 0.16$	710	4711	1.83	$0.50 \pm 0.29$	220.8/46.6/3C228.0
1.19	$0.027 \pm 0.002$	$-1.4 \pm 0.1$	$2.13 \pm 0.20$	$44.16 \pm 5.34$	98	0.05	1	220.8/46.6/3C228.0
$1.30 \pm 0.03$	0.002	$-17.1 \pm 0.6$	$51.37 \pm 1.01$	650	57719	1.30	$0.50 \pm 0.00$	200.2/52.7/3C234
$1.29 \pm 0.05$	0.002	$0.3 \pm 0.2$	$12.39 \pm 0.60$	640	3356	0.31	$0.50 \pm 0.00$	200.2/52.7/3C234
$0.31 \pm 0.04$	0.004	$-44.1 \pm 1.2$	$17.62 \pm 2.72$	80	6791	0.11	$0.50 \pm 0.00$	190.1/54.0/3C236
$1.53 \pm 0.02$	0.004	$-10.1 \pm 0.4$	$36.79 \pm 0.97$	380	29606	1.10	$0.50 \pm 0.00$	190.1/54.0/3C236
4.08	$0.006 \pm 0.000$	$-5.7 \pm 0.2$	$16.31 \pm 0.32$	$656.14 \pm 5.07$	5816	1.30	2	232.1/46.6/3C237
1.39	$0.005 \pm 0.000$	$-3.0 \pm 0.1$	$2.48 \pm 0.16$	$255.60 \pm 10.79$	134	0.07	1	232.1/46.6/3C237
4.47	$0.398 \pm 0.001$	$1.9 \pm 0.0$	$1.19 \pm 0.00$	$13.61 \pm 0.26$	31	0.13	0	232.1/46.6/3C237
$0.28 \pm 0.01$	0.001	$12.3 \pm 3.9$	$120.09 \pm 12.98$	240	315275	0.65	$0.50 \pm 0.29$	232.1/46.6/3C237
0.45	$0.003 \pm 0.000$	$30.1 \pm 0.2$	$6.04 \pm 0.41$	$168.37 \pm 13.35$	796	0.05	3	232.1/46.6/3C237
$3.71 \pm 0.04$	0.003	$-10.4 \pm 0.1$	$21.46 \pm 0.21$	1240	10065	1.55	$0.50 \pm 0.29$	233.1/56.3/3C245
4.40	$0.009 \pm 0.000$	$-8.6 \pm 0.1$	$5.63 \pm 0.28$	$509.72 \pm 8.36$	693	0.48	0	233.1/56.3/3C245
$0.84 \pm 0.03$	0.014	$-55.2 \pm 0.1$	$9.43 \pm 0.33$	60	1945	0.15	$0.50 \pm 0.00$	228.3/74.4/3C263.1
$1.02 \pm 0.03$	0.007	$-40.1 \pm 0.1$	$11.70 \pm 0.35$	140	2995	0.23	$0.50 \pm 0.00$	228.3/74.4/3C263.1
$0.99 \pm 0.03$	0.005	$-38.2 \pm 0.7$	$52.12 \pm 1.55$	200	59414	1.00	$0.50 \pm 0.00$	228.3/74.4/3C263.1
$0.94 \pm 0.03$	0.008	$-5.9 \pm 0.1$	$16.58 \pm 0.49$	120	6014	0.30	$0.50 \pm 0.00$	228.3/74.4/3C263.1
$0.84 \pm 0.03$	0.004	$-36.2 \pm 0.1$	$10.27 \pm 0.39$	210	2307	0.17	$0.50 \pm 0.00$	237.0/73.6/3C264.0
$1.62 \pm 0.02$	0.004	$-29.6 \pm 0.2$	$49.40 \pm 0.44$	400	53359	1.56	$0.50 \pm 0.00$	237.0/73.6/3C264.0
$2.99 \pm 0.03$	0.003	$-28.8 \pm 0.0$	$9.37 \pm 0.11$	990	1921	0.55	$0.50 \pm 0.00$	256.3/70.1/3C267.0
$1.94 \pm 0.02$	0.003	$-21.3 \pm 0.3$	$37.86 \pm 0.47$	650	31342	1.43	$0.50 \pm 0.00$	256.3/70.1/3C267.0
$1.48 \pm 0.03$	0.005	$-2.5 \pm 0.1$	$12.05 \pm 0.31$	290	3176	0.35	$0.50 \pm 0.00$	256.3/70.1/3C267.0
2.82	$0.029 \pm 0.001$	$-30.6 \pm 0.1$	$3.81 \pm 0.18$	$98.80 \pm 2.65$	316	0.21	2	280.6/74.7/3C272.1

Table 2—Continued

$T_B$	$\tau$	$V_{LSR}$	$\Delta V$	$T_s$	$T_{kmax}$	$N(HI)_{20}$	$\mathcal{F}$ or O	(l/b/SOURCE)
2.72 ± 0.04	0.003	−30.1 ± 0.1	13.84 ± 0.23	900	4184	0.73	0.50 ± 0.29	280.6/74.7/3C272.1
0.98	0.009 ± 0.001	−9.2 ± 0.2	3.12 ± 0.52	112.22 ± 6.42	212	0.06	1	280.6/74.7/3C272.1
3.20 ± 0.03	0.003	−7.4 ± 0.1	20.88 ± 0.23	1060	9526	1.30	0.50 ± 0.29	280.6/74.7/3C272.1
1.26	0.015 ± 0.001	−1.5 ± 0.1	3.61 ± 0.34	87.48 ± 3.80	284	0.09	0	280.6/74.7/3C272.1
1.72 ± 0.01	0.001	−13.9 ± 0.1	35.03 ± 0.28	1600	26820	1.17	0.50 ± 0.29	289.9/64.4/3C273
0.81	0.018 ± 0.000	−6.3 ± 0.0	2.37 ± 0.04	44.43 ± 3.19	122	0.04	0	289.9/64.4/3C273
3.72	0.006 ± 0.000	−5.5 ± 0.1	6.38 ± 0.17	651.31 ± 6.33	889	0.46	1	289.9/64.4/3C273
0.00	0.002 ± 0.000	24.2 ± 0.1	2.00 ± 0.13	0.00 ± 0.00	87	0.00	3	289.9/64.4/3C273
0.64 ± 0.01	0.000	26.1 ± 0.2	20.99 ± 0.56	5700	9626	0.26	0.50 ± 0.29	289.9/64.4/3C273
0.00	0.003 ± 0.000	31.8 ± 0.1	2.85 ± 0.12	0.00 ± 0.00	177	0.00	2	289.9/64.4/3C273
1.52 ± 0.06	0.003	−28.0 ± 0.1	9.33 ± 0.25	500	1902	0.28	0.50 ± 0.29	269.9/83.2/3C274.1
0.88	0.009 ± 0.001	−26.8 ± 0.2	3.91 ± 0.51	96.68 ± 8.54	334	0.07	1	269.9/83.2/3C274.1
0.93 ± 0.02	0.003	−14.9 ± 0.4	53.31 ± 0.74	280	62117	0.97	0.50 ± 0.29	269.9/83.2/3C274.1
3.80	0.102 ± 0.001	−1.6 ± 0.0	2.94 ± 0.04	39.15 ± 2.41	189	0.23	0	269.9/83.2/3C274.1
6.56 ± 0.05	0.009	0.4 ± 0.0	6.36 ± 0.05	730	884	0.81	0.52 ± 0.29	269.9/83.2/3C274.1
1.79 ± 0.06	0.015	−13.1 ± 0.6	54.01 ± 1.78	120	63800	1.88	0.50 ± 0.00	56.5/80.7/3C286
1.16 ± 0.11	0.010	−6.0 ± 0.3	7.27 ± 0.89	115	1157	0.16	0.50 ± 0.00	56.5/80.7/3C286
0.58 ± 0.05	0.003	−30.3 ± 0.4	8.85 ± 1.05	190	1714	0.10	0.50 ± 0.00	54.6/76.1/3C293
1.25 ± 0.04	0.003	−13.7 ± 0.6	41.71 ± 1.01	410	38041	1.01	0.50 ± 0.00	54.6/76.1/3C293
1.07 ± 0.06	0.003	−5.2 ± 0.2	8.32 ± 0.55	360	1512	0.17	0.50 ± 0.00	54.6/76.1/3C293
1.25 ± 0.04	0.002	−12.1 ± 0.6	33.81 ± 0.91	670	24982	0.83	0.50 ± 0.29	38.5/60.2/3C310
17.93	0.620 ± 0.003	−3.7 ± 0.0	1.75 ± 0.01	38.81 ± 3.37	66	0.82	1	38.5/60.2/3C310
9.54 ± 0.21	0.005	−1.4 ± 0.1	9.54 ± 0.11	1900	1990	1.77	0.49 ± 0.29	38.5/60.2/3C310
2.86	0.061 ± 0.001	0.6 ± 0.1	5.11 ± 0.13	48.36 ± 4.76	571	0.29	0	38.5/60.2/3C310
24.03	0.784 ± 0.011	−4.2 ± 0.0	2.15 ± 0.02	44.23 ± 2.20	100	1.45	0	39.3/58.5/3C315
2.04 ± 0.30	0.001	−4.2 ± 0.3	26.13 ± 2.18	1380	14922	1.03	0.50 ± 0.29	39.3/58.5/3C315
12.49 ± 0.36	0.018	−2.8 ± 0.5	6.26 ± 1.10	710	856	1.52	0.16 ± 0.23	39.3/58.5/3C315
8.30	0.146 ± 0.004	1.6 ± 0.1	4.41 ± 0.15	61.00 ± 15.11	425	0.77	1	39.3/58.5/3C315
0.32 ± 0.02	0.005	−56.0 ± 0.7	19.18 ± 1.59	60	8043	0.12	0.50 ± 0.29	30.0/54.8/3C318
0.93 ± 0.03	0.001	−11.2 ± 0.5	42.74 ± 1.16	950	39924	0.77	0.53 ± 0.28	30.0/54.8/3C318
13.05	0.482 ± 0.013	−6.0 ± 0.0	1.77 ± 0.03	34.12 ± 4.47	68	0.57	0	30.0/54.8/3C318
15.55	0.300 ± 0.011	−5.0 ± 0.0	3.36 ± 0.04	60.07 ± 5.81	246	1.18	1	30.0/54.8/3C318
11.64 ± 0.17	0.012	−3.4 ± 0.0	9.32 ± 0.06	1000	1899	2.11	0.43 ± 0.29	30.0/54.8/3C318
0.72 ± 0.02	0.000	−37.8 ± 0.5	27.06 ± 1.80	1790	16007	0.38	0.50 ± 0.29	37.6/42.3/3C333
3.84 ± 0.06	0.002	−0.6 ± 0.1	24.47 ± 0.35	2050	13090	1.83	0.51 ± 0.29	37.6/42.3/3C333
17.01	0.993 ± 0.010	0.9 ± 0.0	2.11 ± 0.02	27.01 ± 7.96	97	1.10	0	37.6/42.3/3C333
16.93 ± 0.55	0.028	0.9 ± 0.0	5.40 ± 0.10	610	636	1.78	0.50 ± 0.29	37.6/42.3/3C333
2.66	0.259 ± 0.003	−2.2 ± 0.0	1.65 ± 0.03	11.65 ± 4.80	59	0.10	1	23.0/29.2/3C348
15.39 ± 0.21	0.017	−0.4 ± 0.0	6.29 ± 0.07	890	863	1.88	0.55 ± 0.28	23.0/29.2/3C348
14.76	0.604 ± 0.004	0.5 ± 0.0	2.12 ± 0.01	32.54 ± 5.82	98	0.81	0	23.0/29.2/3C348
3.31 ± 0.04	0.001	2.8 ± 0.1	35.08 ± 0.29	3300	26904	2.26	0.50 ± 0.29	23.0/29.2/3C348
8.53	0.078 ± 0.002	7.2 ± 0.0	3.73 ± 0.09	113.21 ± 1.57	304	0.64	2	23.0/29.2/3C348
1.72	0.006 ± 0.001	−8.4 ± 0.2	4.19 ± 0.57	292.48 ± 48.11	383	0.14	4	21.1/19.9/3C353
25.87	1.209 ± 0.007	0.0 ± 0.0	2.80 ± 0.01	36.89 ± 10.12	170	2.43	1	21.1/19.9/3C353
28.62	0.195 ± 0.008	1.4 ± 0.0	5.84 ± 0.07	161.35 ± 4.53	746	3.59	0	21.1/19.9/3C353
15.37	0.859 ± 0.006	2.4 ± 0.0	1.69 ± 0.01	26.66 ± 13.08	62	0.76	2	21.1/19.9/3C353
7.33 ± 0.13	0.005	6.0 ± 0.3	26.88 ± 0.38	1560	15797	3.84	0.51 ± 0.29	21.1/19.9/3C353
1.57	0.040 ± 0.001	11.9 ± 0.0	3.01 ± 0.07	39.89 ± 5.32	198	0.09	3	21.1/19.9/3C353
2.85 ± 0.03	0.003	−63.7 ± 0.1	24.05 ± 0.34	980	12640	1.34	0.50 ± 0.29	63.3/−5.9/3C409

Table 2—Continued

$T_B$	$\tau$	$V_{LSR}$	$\Delta V$	$T_s$	$T_{kmax}$	$N(HI)_{20}$	$\mathcal{F}$ or O	( $l/b$ /SOURCE)
11.93	$0.451 \pm 0.002$	$3.9 \pm 0.0$	$3.03 \pm 0.02$	$32.85 \pm 7.01$	201	0.88	0	63.3/–5.9/3C409
11.86	$0.331 \pm 0.003$	$7.7 \pm 0.0$	$2.91 \pm 0.04$	$42.08 \pm 10.70$	184	0.79	3	63.3/–5.9/3C409
45.67 ± 1.51	0.013	$11.2 \pm 0.1$	$12.97 \pm 0.37$	3460	3674	11.52	$0.39 \pm 0.27$	63.3/–5.9/3C409
22.40	$0.861 \pm 0.010$	$13.7 \pm 0.0$	$1.96 \pm 0.02$	$38.80 \pm 18.47$	83	1.28	2	63.3/–5.9/3C409
10.44	$0.413 \pm 0.011$	$14.0 \pm 0.0$	$6.90 \pm 0.13$	$30.85 \pm 11.38$	1040	1.71	4	63.3/–5.9/3C409
11.45 ± 0.39	0.010	$15.3 \pm 0.2$	$30.83 \pm 0.28$	1180	20779	6.88	$0.50 \pm 0.29$	63.3/–5.9/3C409
20.64	$0.753 \pm 0.009$	$15.7 \pm 0.0$	$1.69 \pm 0.02$	$38.99 \pm 13.10$	62	0.97	1	63.3/–5.9/3C409
5.17	$0.035 \pm 0.001$	$23.3 \pm 0.1$	$4.27 \pm 0.20$	$148.28 \pm 13.67$	399	0.44	5	63.3/–5.9/3C409
6.58 ± 0.16	0.015	$–68.3 \pm 0.5$	$37.29 \pm 1.19$	430	30404	4.78	$0.49 \pm 0.29$	69.2/–3.8/3C410
0.30	$0.019 \pm 0.005$	$–46.3 \pm 0.3$	$2.53 \pm 0.68$	$16.11 \pm 29.14$	139	0.02	7	69.2/–3.8/3C410
8.43	$0.042 \pm 0.004$	$–23.2 \pm 0.2$	$3.52 \pm 0.37$	$205.53 \pm 15.95$	270	0.59	6	69.2/–3.8/3C410
8.24 ± 0.37	0.015	$–21.5 \pm 0.3$	$16.36 \pm 0.89$	550	5851	2.63	$0.50 \pm 0.29$	69.2/–3.8/3C410
13.06	$0.369 \pm 0.061$	$–0.7 \pm 0.2$	$3.51 \pm 0.21$	$42.30 \pm 13.68$	269	1.07	3	69.2/–3.8/3C410
26.67	$0.654 \pm 0.025$	$2.6 \pm 0.2$	$4.33 \pm 0.34$	$55.56 \pm 22.19$	409	3.06	2	69.2/–3.8/3C410
52.84	$2.214 \pm 0.030$	$7.8 \pm 0.0$	$2.77 \pm 0.05$	$59.33 \pm 24.84$	167	7.08	1	69.2/–3.8/3C410
59.82 ± 1.00	0.035	$8.0 \pm 0.2$	$21.77 \pm 0.39$	1710	10360	25.37	$0.52 \pm 0.29$	69.2/–3.8/3C410
31.74	$0.688 \pm 0.009$	$11.3 \pm 0.1$	$3.55 \pm 0.11$	$63.79 \pm 22.10$	276	3.04	0	69.2/–3.8/3C410
0.00	$0.118 \pm 0.004$	$17.8 \pm 0.1$	$4.81 \pm 0.25$	$0.00 \pm 0.00$	506	0.00	4	69.2/–3.8/3C410
8.04	$0.103 \pm 0.004$	$25.0 \pm 0.1$	$3.54 \pm 0.17$	$82.37 \pm 8.82$	274	0.58	5	69.2/–3.8/3C410
2.66	$0.162 \pm 0.008$	$2.1 \pm 0.0$	$1.45 \pm 0.06$	$17.85 \pm 10.98$	45	0.08	0	74.5/–17.7/3C433
24.25	$0.258 \pm 0.007$	$3.0 \pm 0.0$	$4.12 \pm 0.09$	$106.60 \pm 4.40$	371	2.21	1	74.5/–17.7/3C433
10.26 ± 0.10	0.007	$3.5 \pm 0.1$	$25.31 \pm 0.22$	1450	14005	5.06	$0.50 \pm 0.29$	74.5/–17.7/3C433
6.71	$0.076 \pm 0.003$	$6.9 \pm 0.0$	$1.97 \pm 0.10$	$92.22 \pm 5.03$	84	0.27	2	74.5/–17.7/3C433
4.39	$0.053 \pm 0.002$	$16.0 \pm 0.0$	$3.11 \pm 0.11$	$85.00 \pm 4.10$	210	0.27	3	74.5/–17.7/3C433
1.69 ± 0.02	0.004	$–50.9 \pm 0.2$	$28.82 \pm 0.59$	420	18158	0.95	$0.50 \pm 0.29$	88.1/–35.9/3C454.0
2.75 ± 0.13	0.002	$–7.7 \pm 0.5$	$26.54 \pm 0.49$	1360	15397	1.42	$0.50 \pm 0.29$	88.1/–35.9/3C454.0
6.81	$0.045 \pm 0.001$	$–1.5 \pm 0.1$	$6.39 \pm 0.20$	$156.34 \pm 5.71$	892	0.87	1	88.1/–35.9/3C454.0
6.98 ± 0.20	0.007	$–0.2 \pm 0.1$	$12.94 \pm 0.28$	1070	3658	1.76	$0.50 \pm 0.29$	88.1/–35.9/3C454.0
5.91	$0.093 \pm 0.001$	$3.9 \pm 0.0$	$3.12 \pm 0.05$	$66.22 \pm 2.48$	213	0.38	0	88.1/–35.9/3C454.0
0.91	$0.016 \pm 0.001$	$–35.4 \pm 0.1$	$3.36 \pm 0.18$	$56.79 \pm 7.80$	246	0.06	5	86.0/–38.1/3C454.3
3.02 ± 0.05	0.005	$–31.2 \pm 0.5$	$36.89 \pm 1.14$	570	29756	2.17	$0.50 \pm 0.29$	86.0/–38.1/3C454.3
0.42	$0.048 \pm 0.001$	$–30.4 \pm 0.0$	$2.00 \pm 0.05$	$8.92 \pm 3.30$	87	0.02	4	86.0/–38.1/3C454.3
2.18	$0.015 \pm 0.001$	$–16.8 \pm 0.1$	$5.51 \pm 0.27$	$151.25 \pm 9.11$	664	0.24	6	86.0/–38.1/3C454.3
10.73	$0.298 \pm 0.001$	$–10.1 \pm 0.0$	$2.65 \pm 0.01$	$41.65 \pm 1.52$	153	0.64	3	86.0/–38.1/3C454.3
7.59	$0.091 \pm 0.001$	$–2.0 \pm 0.0$	$3.69 \pm 0.07$	$86.97 \pm 5.18$	297	0.57	0	86.0/–38.1/3C454.3
9.02 ± 0.24	0.005	$–1.1 \pm 0.1$	$14.96 \pm 0.29$	2000	4891	2.63	$0.52 \pm 0.29$	86.0/–38.1/3C454.3
3.50	$0.079 \pm 0.003$	$0.7 \pm 0.0$	$1.81 \pm 0.06$	$46.32 \pm 4.91$	71	0.13	2	86.0/–38.1/3C454.3
0.88	$0.022 \pm 0.001$	$3.4 \pm 0.2$	$4.20 \pm 0.35$	$40.89 \pm 12.03$	386	0.07	1	86.0/–38.1/3C454.3
2.26 ± 0.03	0.010	$–11.5 \pm 0.2$	$24.96 \pm 0.29$	220	13614	1.10	$0.50 \pm 0.29$	322.2/68.8/4C07.32
4.71 ± 0.07	0.010	$–1.9 \pm 0.0$	$7.48 \pm 0.12$	470	1221	0.69	$0.50 \pm 0.29$	322.2/68.8/4C07.32
6.90	$0.177 \pm 0.005$	$–1.9 \pm 0.0$	$2.19 \pm 0.07$	$42.62 \pm 2.28$	105	0.32	0	322.2/68.8/4C07.32
0.93	$0.022 \pm 0.004$	$–12.8 \pm 0.4$	$5.57 \pm 1.04$	$42.86 \pm 2.32$	678	0.10	2	39.6/17.1/4C13.65
14.24	$0.600 \pm 0.039$	$1.4 \pm 0.1$	$2.04 \pm 0.08$	$31.55 \pm 2.71$	90	0.75	1	39.6/17.1/4C13.65
10.04 ± 0.14	0.022	$1.9 \pm 0.0$	$7.06 \pm 0.08$	460	1088	1.38	$0.50 \pm 0.29$	39.6/17.1/4C13.65
10.20	$0.344 \pm 0.023$	$3.4 \pm 0.2$	$2.57 \pm 0.20$	$35.09 \pm 3.09$	144	0.60	0	39.6/17.1/4C13.65
2.66 ± 0.07	0.023	$9.6 \pm 0.1$	$4.73 \pm 0.17$	115	489	0.24	$0.50 \pm 0.29$	39.6/17.1/4C13.65
8.53 ± 0.07	0.022	$12.8 \pm 0.1$	$35.42 \pm 0.15$	390	27432	5.89	$0.51 \pm 0.29$	39.6/17.1/4C13.65
1.88 ± 0.06	0.008	$20.0 \pm 0.1$	$5.57 \pm 0.21$	230	677	0.20	$0.50 \pm 0.29$	39.6/17.1/4C13.65
2.94 ± 0.04	0.008	$–67.8 \pm 0.2$	$32.25 \pm 0.57$	370	22741	1.85	$0.50 \pm 0.29$	43.5/9.2/4C13.67

Table 2—Continued

$T_B$	$\tau$	$V_{LSR}$	$\Delta V$	$T_s$	$T_{kmax}$	$N(HI)_{20}$	$\mathcal{F}$ or O	( $l/b$ /SOURCE)
17.73	$1.161 \pm 0.015$	$2.0 \pm 0.0$	$2.10 \pm 0.02$	$25.81 \pm 6.76$	96	1.22	1	43.5/9.2/4C13.67
30.01 $\pm$ 2.21	0.061	$4.9 \pm 0.1$	$8.37 \pm 0.42$	490	1532	4.88	$0.31 \pm 0.27$	43.5/9.2/4C13.67
18.90	$1.019 \pm 0.010$	$6.2 \pm 0.0$	$4.01 \pm 0.04$	$29.56 \pm 8.37$	351	2.36	0	43.5/9.2/4C13.67
2.36	$0.030 \pm 0.003$	$20.2 \pm 0.4$	$8.20 \pm 0.89$	$80.73 \pm 7.14$	1469	0.38	2	43.5/9.2/4C13.67
6.63 $\pm$ 0.16	0.018	$20.4 \pm 0.4$	$46.69 \pm 0.45$	360	47663	6.03	$0.51 \pm 0.29$	43.5/9.2/4C13.67
0.92 $\pm$ 0.03	0.031	$-11.4 \pm 0.5$	$37.36 \pm 0.92$	30	30532	0.67	$0.50 \pm 0.00$	9.0/73.0/4C19.44
4.14 $\pm$ 0.14	0.041	$-6.3 \pm 0.0$	$3.13 \pm 0.10$	100	213	0.25	$0.50 \pm 0.00$	9.0/73.0/4C19.44
7.84 $\pm$ 0.15	0.049	$-3.4 \pm 0.0$	$9.70 \pm 0.11$	160	2059	1.48	$0.50 \pm 0.00$	9.0/73.0/4C19.44
5.86 $\pm$ 0.13	0.117	$-2.8 \pm 0.0$	$2.18 \pm 0.05$	50	103	0.25	$0.50 \pm 0.00$	9.0/73.0/4C19.44
0.83 $\pm$ 0.04	0.010	$-13.2 \pm 0.5$	$37.94 \pm 1.07$	80	31466	0.62	$0.50 \pm 0.29$	20.2/66.8/4C20.33
2.92	$0.058 \pm 0.003$	$-9.0 \pm 0.1$	$2.48 \pm 0.12$	$51.56 \pm 2.54$	134	0.15	1	20.2/66.8/4C20.33
6.72 $\pm$ 0.07	0.009	$-5.9 \pm 0.0$	$11.74 \pm 0.09$	780	3015	1.54	$0.49 \pm 0.29$	20.2/66.8/4C20.33
4.01	$0.049 \pm 0.002$	$-2.6 \pm 0.1$	$4.75 \pm 0.21$	$84.57 \pm 2.87$	493	0.38	0	20.2/66.8/4C20.33
35.27	$6.994 \pm 1.782$	$-2.2 \pm 0.0$	$1.26 \pm 0.08$	$35.31 \pm 16.92$	34	6.05	1	188.1/0.0/4C22.12
60.36	$7.911 \pm 8.309$	$4.4 \pm 0.1$	$0.83 \pm 0.19$	$60.38 \pm 27.61$	14	7.68	4	188.1/0.0/4C22.12
68.21	$1.756 \pm 0.045$	$5.1 \pm 0.1$	$11.63 \pm 0.21$	$82.46 \pm 27.02$	2954	32.79	3	188.1/0.0/4C22.12
82.17 $\pm$ 9.17	0.183	$6.2 \pm 0.2$	$19.77 \pm 0.51$	450	8548	31.58	$0.45 \pm 0.27$	188.1/0.0/4C22.12
67.48	$4.067 \pm 2.174$	$7.5 \pm 0.1$	$0.90 \pm 0.15$	$68.66 \pm 26.77$	17	4.90	0	188.1/0.0/4C22.12
19.49	$0.840 \pm 0.034$	$15.8 \pm 0.1$	$3.97 \pm 0.16$	$34.28 \pm 12.06$	345	2.23	2	188.1/0.0/4C22.12
2.24	$0.020 \pm 0.001$	$-16.9 \pm 0.1$	$2.55 \pm 0.22$	$113.15 \pm 4.56$	141	0.11	0	67.2/81.0/4C32.44
1.53 $\pm$ 0.03	0.005	$-10.2 \pm 0.3$	$30.49 \pm 0.70$	280	20325	0.91	$0.50 \pm 0.29$	67.2/81.0/4C32.44
1.10	$0.007 \pm 0.002$	$-4.6 \pm 0.2$	$1.41 \pm 0.42$	$147.74 \pm 15.32$	43	0.03	1	67.2/81.0/4C32.44
23.18	$0.389 \pm 0.006$	$-0.5 \pm 0.0$	$4.18 \pm 0.06$	$71.97 \pm 8.85$	381	2.28	1	166.6/-33.6/CTA21
5.59	$0.193 \pm 0.012$	$1.3 \pm 0.0$	$1.70 \pm 0.09$	$31.82 \pm 11.99$	63	0.20	0	166.6/-33.6/CTA21
22.24 $\pm$ 0.25	0.008	$1.6 \pm 0.1$	$14.85 \pm 0.11$	2850	4817	6.43	$0.46 \pm 0.29$	166.6/-33.6/CTA21
7.55	$0.108 \pm 0.002$	$6.9 \pm 0.0$	$4.17 \pm 0.11$	$73.69 \pm 6.97$	379	0.65	2	166.6/-33.6/CTA21
3.90 $\pm$ 0.06	0.010	$1.3 \pm 0.1$	$9.03 \pm 0.18$	390	1784	0.69	$0.50 \pm 0.00$	209.8/16.6/DW0742+1
2.63 $\pm$ 0.05	0.011	$8.2 \pm 0.2$	$34.01 \pm 0.44$	250	25294	1.74	$0.50 \pm 0.00$	209.8/16.6/DW0742+1
4.06 $\pm$ 3.20	0.007	$-5.4 \pm 9.4$	$36.50 \pm 12.64$	570	29128	2.28	$0.56 \pm 0.28$	159.0/-18.8/NRAO14
134.13 $\pm$ 191.16	0.152	$5.6 \pm 0.7$	$4.16 \pm 1.44$	880	377	7.62	$0.36 \pm 0.30$	159.0/-18.8/NRAO14
38.87 $\pm$ 26.05	0.046	$6.2 \pm 0.3$	$10.01 \pm 3.75$	840	2191	6.17	$0.41 \pm 0.28$	159.0/-18.8/NRAO14
26.83	$7.011 \pm 0.300$	$6.8 \pm 0.0$	$3.66 \pm 0.03$	$26.85 \pm 12.77$	292	13.42	0	159.0/-18.8/NRAO14
21.33	$0.478 \pm 0.014$	$-6.3 \pm 0.1$	$5.10 \pm 0.11$	$56.12 \pm 4.49$	569	2.67	0	177.0/-40.8/P0320+0
7.62	$0.223 \pm 0.024$	$-4.4 \pm 0.1$	$1.37 \pm 0.18$	$38.11 \pm 8.33$	41	0.23	1	177.0/-40.8/P0320+0
12.41 $\pm$ 0.26	0.024	$-1.4 \pm 0.8$	$14.86 \pm 1.08$	520	4828	3.59	$0.51 \pm 0.29$	177.0/-40.8/P0320+0
16.52	$0.372 \pm 0.012$	$5.8 \pm 0.0$	$3.04 \pm 0.09$	$53.23 \pm 3.69$	201	1.17	3	177.0/-40.8/P0320+0
15.60 $\pm$ 0.68	0.018	$10.6 \pm 0.4$	$8.39 \pm 0.70$	870	1539	2.56	$0.50 \pm 0.29$	177.0/-40.8/P0320+0
14.61	$0.408 \pm 0.012$	$11.7 \pm 0.0$	$2.82 \pm 0.08$	$43.62 \pm 8.05$	174	0.98	2	177.0/-40.8/P0320+0
5.30 $\pm$ 0.46	0.053	$-0.6 \pm 0.1$	$2.93 \pm 0.32$	100	187	0.30	$0.50 \pm 0.29$	182.3/-35.7/P0347+0
18.69 $\pm$ 0.36	0.035	$5.7 \pm 0.2$	$16.14 \pm 0.21$	530	5695	5.88	$0.50 \pm 0.29$	182.3/-35.7/P0347+0
40.28	$1.051 \pm 0.027$	$8.0 \pm 0.1$	$3.54 \pm 0.08$	$61.91 \pm 8.28$	273	4.49	1	182.3/-35.7/P0347+0
26.89	$0.171 \pm 0.012$	$12.1 \pm 0.4$	$4.87 \pm 0.64$	$171.55 \pm 6.05$	519	2.78	0	182.3/-35.7/P0347+0
4.27 $\pm$ 0.43	0.009	$-5.4 \pm 1.2$	$40.10 \pm 1.61$	490	35154	3.32	$0.50 \pm 0.29$	176.8/-18.6/P0428+2
19.33	$1.132 \pm 0.016$	$3.2 \pm 0.0$	$3.42 \pm 0.04$	$28.52 \pm 19.69$	255	2.15	2	176.8/-18.6/P0428+2
62.19 $\pm$ 1.66	0.028	$5.3 \pm 0.0$	$11.30 \pm 0.33$	2200	2789	13.67	$0.53 \pm 0.27$	176.8/-18.6/P0428+2
24.22	$1.318 \pm 0.040$	$9.2 \pm 0.0$	$3.70 \pm 0.05$	$33.07 \pm 18.46$	298	3.14	1	176.8/-18.6/P0428+2
21.22	$2.346 \pm 0.128$	$10.6 \pm 0.0$	$1.50 \pm 0.05$	$23.47 \pm 9.38$	49	1.61	0	176.8/-18.6/P0428+2
3.70	$0.011 \pm 0.001$	$-23.1 \pm 0.3$	$6.76 \pm 0.70$	$333.26 \pm 21.57$	1000	0.49	3	186.8/-7.1/P0531+1
17.77	$0.474 \pm 0.003$	$1.8 \pm 0.0$	$2.09 \pm 0.02$	$47.10 \pm 16.58$	95	0.91	2	186.8/-7.1/P0531+1

Table 2—Continued

$T_B$	$\tau$	$V_{LSR}$	$\Delta V$	$T_s$	$T_{kmax}$	$N(HI)_{20}$	$\mathcal{F}$ or $\mathcal{O}$	( $l/b$ /SOURCE)
$31.04 \pm 0.39$	0.010	$3.1 \pm 0.1$	$23.65 \pm 0.20$	3050	12225	14.30	$0.49 \pm 0.29$	186.8/−7.1/P0531+
39.01	$0.229 \pm 0.001$	$5.5 \pm 0.0$	$8.74 \pm 0.06$	$190.74 \pm 13.06$	1670	7.43	0	186.8/−7.1/P0531+
17.87	$0.166 \pm 0.003$	$9.6 \pm 0.0$	$1.87 \pm 0.04$	$117.02 \pm 10.60$	76	0.71	1	186.8/−7.1/P0531+
$1.09 \pm 0.16$	0.014	$-37.2 \pm 0.7$	$21.58 \pm 2.34$	80	10184	0.46	$0.50 \pm 0.00$	201.4/29.7/P0820+
$3.18 \pm 0.19$	0.020	$-7.9 \pm 0.1$	$15.38 \pm 0.58$	160	5171	0.95	$0.50 \pm 0.00$	201.4/29.7/P0820+
$1.11 \pm 0.12$	0.016	$7.2 \pm 4.6$	$63.39 \pm 4.79$	70	87880	1.37	$0.50 \pm 0.00$	201.4/29.7/P0820+
$6.75 \pm 0.10$	0.015	$9.8 \pm 0.1$	$11.03 \pm 0.15$	440	2662	1.45	$0.50 \pm 0.00$	201.4/29.7/P0820+
$1.05 \pm 0.01$	0.002	$-32.2 \pm 0.3$	$29.62 \pm 0.62$	520	19177	0.61	$0.50 \pm 0.29$	222.5/63.1/P1055+
$1.67 \pm 0.04$	0.002	$-4.9 \pm 0.1$	$18.36 \pm 0.38$	810	7371	0.60	$0.50 \pm 0.29$	222.5/63.1/P1055+
1.47	$0.010 \pm 0.001$	$-4.6 \pm 0.1$	$7.94 \pm 0.30$	$149.01 \pm 6.39$	1379	0.23	1	222.5/63.1/P1055+
2.81	$0.073 \pm 0.001$	$-3.6 \pm 0.0$	$2.23 \pm 0.02$	$40.00 \pm 1.10$	108	0.13	0	222.5/63.1/P1055+
$1.36 \pm 0.01$	0.008	$-29.3 \pm 0.3$	$43.23 \pm 0.49$	170	40868	1.14	$0.50 \pm 0.00$	240.4/65.8/P1117+
$1.48 \pm 0.02$	0.005	$-5.3 \pm 0.1$	$14.85 \pm 0.23$	310	4820	0.43	$0.50 \pm 0.00$	240.4/65.8/P1117+
$2.50 \pm 0.94$	0.125	$-27.4 \pm 0.3$	$1.83 \pm 0.84$	20	72	0.09	$0.50 \pm 0.29$	181.4/−5.2/T0526+
$14.45 \pm 1.05$	0.206	$-21.2 \pm 1.6$	$18.94 \pm 2.28$	70	7840	5.35	$0.46 \pm 0.29$	181.4/−5.2/T0526+
30.63	$1.080 \pm 0.037$	$-7.6 \pm 0.1$	$6.22 \pm 0.16$	$46.39 \pm 8.75$	847	6.07	3	181.4/−5.2/T0526+
$55.00 \pm 1.73$	0.196	$0.2 \pm 0.7$	$19.50 \pm 0.92$	280	8315	20.89	$0.22 \pm 0.18$	181.4/−5.2/T0526+
31.38	$2.809 \pm 0.684$	$2.5 \pm 0.0$	$1.08 \pm 0.11$	$33.39 \pm 16.99$	25	1.97	2	181.4/−5.2/T0526+
43.24	$1.413 \pm 0.076$	$5.9 \pm 0.1$	$7.86 \pm 0.20$	$57.14 \pm 10.05$	1352	12.37	1	181.4/−5.2/T0526+
54.72	$39.128 \pm 49.972$	$7.1 \pm 0.1$	$1.20 \pm 0.23$	$54.72 \pm 9.54$	31	50.11	0	181.4/−5.2/T0526+
0.00	$2.105 \pm 0.089$	$6.9 \pm 0.2$	$15.13 \pm 0.28$	$0.00 \pm 0.00$	5006	0.00	1	190.1/−2.2/T0556+
$142.23 \pm 81.04$	0.508	$8.6 \pm 0.1$	$20.06 \pm 1.75$	280	8796	53.63	$0.88 \pm 0.16$	190.1/−2.2/T0556+
0.00	$106.719 \pm 114.205$	$13.1 \pm 0.2$	$3.19 \pm 0.40$	$0.00 \pm 0.00$	222	0.00	0	190.1/−2.2/T0556+
3.96	$0.152 \pm 0.017$	$-11.9 \pm 0.1$	$1.29 \pm 0.16$	$28.13 \pm 7.36$	36	0.11	5	201.5/0.5/T0629+
$61.72 \pm 2.93$	0.206	$4.5 \pm 0.1$	$8.46 \pm 0.32$	300	1563	10.16	$0.24 \pm 0.18$	201.5/0.5/T0629+
28.44	$1.605 \pm 0.035$	$4.9 \pm 0.0$	$4.37 \pm 0.06$	$35.60 \pm 14.16$	416	4.86	1	201.5/0.5/T0629+
46.16	$0.297 \pm 0.005$	$16.9 \pm 0.3$	$28.11 \pm 0.46$	$179.87 \pm 8.78$	17273	29.21	3	201.5/0.5/T0629+
13.91	$0.354 \pm 0.017$	$23.3 \pm 0.1$	$3.03 \pm 0.16$	$46.68 \pm 19.93$	201	0.98	2	201.5/0.5/T0629+
$32.94 \pm 2.66$	0.150	$28.1 \pm 0.5$	$18.82 \pm 0.73$	220	7739	12.07	$0.50 \pm 0.29$	201.5/0.5/T0629+
14.46	$0.271 \pm 0.016$	$30.9 \pm 0.1$	$2.81 \pm 0.26$	$60.90 \pm 13.83$	172	0.90	0	201.5/0.5/T0629+
16.34	$1.285 \pm 0.042$	$33.9 \pm 0.0$	$1.70 \pm 0.05$	$22.59 \pm 10.30$	63	0.96	4	201.5/0.5/T0629+

Note. — For a complete description of table entries, see §4.1. The ordering is by source name as follows: 3C, 4C, CTA, DW, NRAO, P, T. C components have no error for  $T_B$ ; WNM components have no error for  $\tau_0$ . Temperatures are in K, velocities in  $\text{km s}^{-1}$ , column densities in  $10^{20} \text{ cm}^{-2}$ .

Table 3. Comparison of derived parameters

SOURCE: VLSR	$T_{s,worst}$	$T_{0,worst}$		$T_{s,best}$	$T_{0,best}$		$T_{s,adopted}$	$T_{0,adopted}$
3C120 WNM: -19.1	...	$1.1 \pm 0.1$		...	$2.2 \pm 0.1$		...	$2.2 \pm 0.3$
3C120 WNM: 5.2	...	$2.6 \pm 0.1$		...	$6.4 \pm 0.2$		...	$6.0 \pm 1.4$
3C120 CNM: 6.2	$23.6 \pm 1.3$	...		$39.9 \pm 0.3$	...		$37.1 \pm 6.9$	...
3C120 CNM: 7.6	$29.1 \pm 1.9$	...		$45.8 \pm 0.5$	...		$42.3 \pm 10.0$	...
3C120 CNM: 8.1	$34.9 \pm 1.4$	...		$43.0 \pm 0.7$	...		$44.0 \pm 4.0$	...
3C120 WNM: 10.2	...	$27.4 \pm 1.5$		...	$39.4 \pm 0.7$		...	$41.3 \pm 5.6$
3C137 CNM: -4.2	$38.0 \pm 0.2$	...		$46.2 \pm 0.1$	...		$44.2 \pm 2.2$	...
3C137 WNM: -4.2	...	$1.4 \pm 0.1$		...	$2.4 \pm 0.1$		...	$2.0 \pm 0.3$
3C137 WNM: -2.8	...	$11.8 \pm 0.1$		...	$12.7 \pm 0.1$		...	$12.5 \pm 0.4$
3C137 CNM: 1.6	$30.3 \pm 1.5$	...		$69.3 \pm 0.4$	...		$61.0 \pm 15.1$	...

Note. —  $T_s$  are CNM component spin temperatures and  $T_0$  WNM component brightness temperatures. The first column is the VLSR of the WNM or CNM component. After that, the first column pair is the worst case combination of  $\mathcal{F}$  and CNM ordering; the second pair the best case; the third case the adopted values from Table 2.

Table 4. Temperatures by two methods

Source	$T_{s,S,\mathcal{F}=0}$	$T_{s,G,\mathcal{F}=0}$	$(T_{s,S} - T_{s,G})_{\mathcal{F}=0}$		$T_{s,S,\mathcal{F}=1}$	$T_{s,G,\mathcal{F}=1}$	$(T_{s,S} - T_{s,G})_{\mathcal{F}=1}$
3C333( $\mathcal{F} = 0.50$ )	29	25	+4		...	...	...
3C225b	16	19	-3		11	16	-5
3C274.1	53	42	+11		48	36	+12
3C207	24	24	0		17	18	-1
3C207	35	30	+5		23	19	4
P0531+19	64	$\begin{bmatrix} 72 \\ 206 \end{bmatrix}$	$\begin{bmatrix} -8 \\ -142 \end{bmatrix}$		8	$\begin{bmatrix} 40 \\ 171 \end{bmatrix}$	$\begin{bmatrix} -32 \\ -163 \end{bmatrix}$
P0531+19	72	$\begin{bmatrix} 132 \\ 206 \end{bmatrix}$	$\begin{bmatrix} -60 \\ -134 \end{bmatrix}$		18	$\begin{bmatrix} 110 \\ 171 \end{bmatrix}$	$\begin{bmatrix} -92 \\ -153 \end{bmatrix}$
3C79	15	$\begin{bmatrix} 15 \\ 147 \end{bmatrix}$	$\begin{bmatrix} 0 \\ -132 \end{bmatrix}$		0	$\begin{bmatrix} 10 \\ 173 \end{bmatrix}$	$\begin{bmatrix} -10 \\ -173 \end{bmatrix}$
3C79	72	$\begin{bmatrix} 63 \\ 147 \end{bmatrix}$	$\begin{bmatrix} -9 \\ -75 \end{bmatrix}$		18	$\begin{bmatrix} 59 \\ 173 \end{bmatrix}$	$\begin{bmatrix} -41 \\ -155 \end{bmatrix}$
3C318	43	$\begin{bmatrix} 39 \\ 66 \end{bmatrix}$	$\begin{bmatrix} 4 \\ -17 \end{bmatrix}$		29	$\begin{bmatrix} 31 \\ 53 \end{bmatrix}$	$\begin{bmatrix} -2 \\ -24 \end{bmatrix}$
3C138	57	$\begin{bmatrix} 60 \\ 68 \\ 350 \end{bmatrix}$	$\begin{bmatrix} -3 \\ -11 \\ -293 \end{bmatrix}$		16	$\begin{bmatrix} 36 \\ 44 \\ 379 \end{bmatrix}$	$\begin{bmatrix} -20 \\ -28 \\ -363 \end{bmatrix}$
3C138	63	$\begin{bmatrix} 68 \\ 65 \\ 350 \end{bmatrix}$	$\begin{bmatrix} -5 \\ -2 \\ -287 \end{bmatrix}$		30	$\begin{bmatrix} 53 \\ 57 \\ 379 \end{bmatrix}$	$\begin{bmatrix} -23 \\ -27 \\ -349 \end{bmatrix}$
3C133	54	$\begin{bmatrix} 56 \\ 67 \end{bmatrix}$	$\begin{bmatrix} -2 \\ -13 \end{bmatrix}$		9	$\begin{bmatrix} 18 \\ 20 \end{bmatrix}$	$\begin{bmatrix} -9 \\ -11 \end{bmatrix}$
3C133	70	$\begin{bmatrix} 67 \\ 78 \end{bmatrix}$	$\begin{bmatrix} 3 \\ -8 \end{bmatrix}$		20	$\begin{bmatrix} 20 \\ 48 \end{bmatrix}$	$\begin{bmatrix} 0 \\ -28 \end{bmatrix}$
3C120( $\mathcal{F} = 0$ )	29	$\begin{bmatrix} 46 \\ 40 \\ 43 \end{bmatrix}$	$\begin{bmatrix} -17 \\ -11 \\ -14 \end{bmatrix}$		...	...	...
P0420+20( $\mathcal{F} = 0.55$ )	2	$\begin{bmatrix} 27 \\ 34 \end{bmatrix}$	$\begin{bmatrix} -25 \\ -32 \end{bmatrix}$		...	...	...
P0420+20( $\mathcal{F} = 0.55$ )	41	29	12		...	...	...

Note. —  $T_{s,S}$  and  $T_{s,G}$  are spin temperatures determined from the slope and Gaussian methods, respectively. We provide comparisons for  $\mathcal{F} = 0$  in columns 2-4 and for  $\mathcal{F} = 1$  in columns 5-7. Multiple values of  $T_{s,G}$  enclosed in square brackets mean that more than one Gaussian is associated with the single value of  $T_{s,S}$ ; see section 5.